COMPUTATIONAL STUDIES OF CHEMICAL SYSTEMS:
I. A THEORETICAL INVESTIGATION OF CLATHRATE HYDRATES
II. CONFORMATIONAL POTENTIAL ENERGY SURFACE OF TRYPTAMINE

by

Valerie N. McCarthy

BA, Albion College, 2002

Submitted to the Graduate Faculty of

the Department of Chemistry in partial fulfillment

of the requirements for the degree of

Doctor of Philosophy

University of Pittsburgh

2008

UNIVERSITY OF PITTSBURGH

CHEMISTRY DEPARTMENT

This dissertation was presented

by

Valerie N. McCarthy

It was defended on

January 15, 2008

and approved by

Kenneth D. Jordan, Chemistry Department

David Pratt, Chemistry Department

Peter Siska, Chemistry Department

Jeffry Madura, Chemistry Department

Dissertation Director: Kenneth D. Jordan, Chemistry Department

COMPUTATIONAL STUDIES OF CHEMICAL SYSTEMS:
I. A THEORETICAL INVESTIGATION OF CLATHRATE HYDRATES
II. CONFORMATIONAL POTENTIAL ENERGY SURFACE OF TRYPTAMINE

Valerie N. McCarthy, PhD

University of Pittsburgh, 2008

Hydrogen clathrates have recently been discovered and considered as storage medium for H_2. Hydrogen forms a Type II clathrate structure, with a small and large cage. Multiple guest hydrogen molecules can occupy both cages (up to two in the small cage and four in the large cage), although the number of hydrogen molecules occupying the small cage has been a source of debate in the literature. The goal of this work has been to develop a polarizable force field for use in molecular dynamics simulations of hydrogen clathrates. The resulting force field has been coded in the DLPOLY package and simulations of the system as a function of the number of guest hydrogen molecules have been performed. The development of the force field, and the results of the simulations are discussed.

In order for a clathrate structure to form, a 'guest' molecule must be present under ideal conditions. That is, water does not form a so-called 'self' hydrate. In order to elucidate the factors responsible for clathrate formation, *ab initio* calculations were performed on $(H_2O)_{21}$ and $(H_2O)_{20}{\cdot}H_2S$ clusters. The results of these calculations have provided insight into why water does not form a self hydrate.

Stimulated emission pumping experiments done by the Zwier group have established bounds on the low energy isomerization barriers between specific minima of tryptamine. In

order to identify the low energy isomerization pathways, the Becke3LYP and RI-MP2 methods were used to characterize the low-energy minima and the transition states of tryptamine. In general there is good agreement between theory and experiment, but for a subset of the isomerization processes, the calculations give significantly higher barriers than deduced from experiment. Possible causes of this discrepancy are discussed.

TABLE OF CONTENTS

LIST OF TABLES

LIST OF FIGURES

PREFACE

This is the culmination of a scholastic journey that began a long, long time ago, and there are some very important people who have helped me stay the course during the many times when I was ready to abandon ship.

I owe my parents my complete gratitude for their hand in who I am today. They have stood by my side through everything and have loved me just the same for my successes and my failures, and probably deserve medals for putting up with me during the more trying experiences of graduate school. My dad (Ed) was the voice in my ear telling me to never ever give up, and my mom (Cathy) knows me better than anyone and is always able to magically say the right things. My brother (Mike) and my sister (Stephanie) are my best friends and their support means the world to me.

I have been lucky to have met such wonderful, funny, and intelligent people throughout my time in the chemistry department. My graduate school sister and my faithful running buddy (Inland Trail Marathon champs!), Demetra Czegan, was always up for a run, a work-out at the gym, a trip to the Monroeville mall, or just hanging out. I will always have a special place in my heart for the Saturday morning long runs, up before the sun, and solving all the world's problems. We also saw some pretty spectacular sunrises. My many, many thanks to you, DeeDee! I will miss you dearly, but know that we will always remain close, no matter where life takes us. I also want to thank my good friend and former roommate, Katherine Stone, for always being able to make me laugh, and for reminding to stop finding things to worry about. Also, Katherine was always game for a good "Law and Order" marathon on TV. Mark Ams and I met during our freshman year at Albion College, and

became good friends and even neighbors during graduate school. Mark is one of the nicest, most down-to-earth people I know, and I thank him for helping me stay grounded. I will likely never meet anyone like Kadir Diri, my Jordan group colleague, who is now a cherished friend. Kadir was a constant source of support, a sounding board, someone who could talk about quantum mechanics in one minute, and the latest "South Park" episode the next. We had so many good times over the years, but what will stand out the most to me is all of our long discussions about everything under the sun. Somehow, a two-second question would turn into a two-hour talk. Kadir, you are truly one of a kind. I also want to thank Jun Cui (another Jordan group colleague) for her friendship and support, and for always being my 'hole in the ground'. I'd also like to thank Mandy Matson and Kris Takach for their friendship, and for all the fun times we had. Lunch will never be the same! I want to especially thank them for being my career counselors and reviewing countless resumes and cover letters for me. I will continue to be amazed at their seemingly endless patience with me as we analyzed every single job interview I ever had at least ten times. And finally, I'd like to acknowledge Bill Valenta, former Assistant Chair. Bill's door was always open (even after he left the chemistry department), and I will be forever grateful for his words of wisdom, kindness, and career advice as I navigated my final year of graduate school, and finally learned to follow my heart.

Of course, none of this would have been possible without the guidance of my advisor Ken Jordan, whose passion for science and learning will always be an inspiration to me. Ken was always available and willing to discuss just about any topic from science, to hockey, to running. I truly admire and respect Ken for his devotion to the field and to his students.

I would especially like to thank Daniel Schofield and Hao Jiang for their help with the clathrate projects, as well as all my fellow Jordan group members (past and present) for all the scientific discussions and moral support throughout the years.

1.0 INTRODUCTION

The research presented in this dissertation focuses on utilizing electronic structure and molecular dynamics simulation methods to address important chemical problems. Specifically, I have used quantum mechanical *ab initio* techniques to study the conformational properties of biomolecules and have developed a force field for use in dynamics simulations to characterize gas hydrates. These projects have been in collaboration with experimental groups.

1.0.1 Gas hydrates

Clathrate hydrates are naturally occurring solid cages of water that form around small gas molecules such as methane, hydrogen, or carbon dioxide when the appropriate conditions are met. The field of clathrate hydrate chemistry is one ripe with possibilities for research. Recent experimental work on hydrates has raised the possibility of using clathrates as a storage and transportation medium for H_2, thereby making the possibility of hydrogen as an alternative fuel source a more realistic goal.[1] However, a more comprehensive understanding of hydrogen clathrates is crucial to the energy industry. The development of a force field for use in molecular dynamics simulations on hydrogen clathrates is discussed. Additionally, a main focus of this work is dedicated to understanding the formation mechanisms of clathrates with regards to $(H_2O)_{21}$ and $(H_2O)_{20}{\cdot}H_2S$ clusters.

1.0.1.1 Stability of H_2 clathrates *vs.* cavity occupancy Hydrogen clathrates are a fairly recent and surprising discovery as it was thought that hydrogen was too small to form

a clathrate structure.[2] Additionally, hydrogen is one of the only molecules (N_2 is another[3]) in which multiply occupied cages have been seen. Hydrogen clathrates form a Type II structure with 136 water molecules forming 24 cages in the unit cell. Sixteen of the cages are pentagonal dodecahedra (5^{12}) and the other eight cages are 16-hedra ($5^{12}6^4$). In the case of hydrogen clathrates, hydrogen molecules occupy both cages. The stability of the system is related to the number of H_2 molecules inside the various cavities.

My research has involved developing a polarizable H_2-water potential for use in Molecular Dynamics (MD) and Monte Carlo simulations of the hydrogen hydrates. The resulting potential uses point charges for the electrostatics and a mobile point charge to represent induced polarizability, a Buckingham[4] term is used for the repulsions and dispersive interactions between the water and hydrogen molecules. This potential was constructed in the spirit of the charge on a spring (COS) water model.[5] The multipoles and polarizabilities used in the potential as well as the parameters for the H_2O-H_2 and H_2-H_2 interactions in the Buckingham term were determined from MP2/aug-cc-pV5Z calculations.

This potential has been has been shown to closely reproduce *ab initio* results and has been coded into the DLPOLY[6] package. Simulations on the hydrogen clathrate system as function of hydrogen guest occupancy numbers have been performed, and the results are in agreement with experimental data.

1.0.1.2 $(H_2O)_{21}$ *vs* $(H_2O)_{20}\cdot H_2S$

To gain insight into the factors responsible for the different behavior of H_2O and H_2S with respect to hydrate formation, we have employed the density functional[7,8] and RIMP[9,10] electronic structure methods to examine the stability of the $(H_2O)_{21}$ and $(H_2O)_{20}\cdot H_2S$ cluster systems. The starting point for the various calculations was the undistorted dodecahedral $(H_2O)_{20}$ cage. The additional H_2O or H_2S molecule was then added to the interior of the cluster, either retaining the ten free OH groups of the cage, giving the so called $(20,1)_{10}$ species or with two of the free OH groups reoriented inward to give the $(20,1)_8$ species.

1.0.2 Conformational potential energy surface of tryptamine

The biomolecule, tryptamine, is a neurotransmitter with a flexible ethylamine side chain and has served as a testing ground for conformation specific infrared spectroscopy. Recent *ab initio* calculations have identified 11 low-energy minima of tryptamine, differing in the orientation and position of the ethylamine side chain.[11,12,13] Stimulated emission pumping (SEP)-hole filling spectroscopy and SEP-induced population transfer spectroscopy have been used to measure the energy thresholds to conformational isomerization in tryptamine by the Zwier group at Purdue University.[14] This technique has uncovered low-energy isomerization pathways, but is incapable of providing specific information about the properties of the transition state molecules.

To aid in the analysis of the experiments and to identify low-energy pathways, we have carried out a theoretical investigation of the minima and transition states of tryptamine. We used the density functional, RIMP2, and CCSD(T) electronic structure methods to characterize the 11 low lying minima on the potential energy surface, and we located the transition states using the QST3[15] algorithm.

The theoretical results for most of the pathways are in good agreement with the experimental barriers. However, the calculated pathways involving certain isomerizations have barriers considerably larger than those seen experimentally.

2.0 CLATHRATE INTRODUCTION

2.1 CLATHRATE REVIEW AND HISTORY

Clathrate hydrates are naturally occurring solid cages of water that form around small gas molecules such as methane, hydrogen, or carbon dioxide when the appropriate conditions are met.[16,17] On a molecular scale, single small guest molecules are encaged in cavities of hydrogen bonded networks of water molecules in a non-stoichiometric ratio. The guest molecule dictates the type of cage structure that will form with the three most common and well defined types known as Type I, Type II and Type H, shown in Figure 2.1.[18,19,20,21] Type I is the most common naturally occurring clathrate and contains small (0.4-0.55 nm) guests; Type II occurs mostly in man-made environments and can hold larger guests (0.6-0.7nm); and Type H occurs in both natural and man-made environments and can hold large (0.8-0.9 nm) guests.[22] Additionally, there are several unique structures formed by bromine,[23] dimethyl ether[24] and tert-butylamine.[25]

In Type I and Type II, water molecules form hydrogen bonds in a basic building block called 5^12 (pentagonal dodecahedra) because there are 12 faces of pentagonally bonded water molecules. Both types incorporate additional cages containing hexagonal (two in the $5^{12}6^2$ cavity of Type I and four in the $5^{12}6^4$ cavity of Type II) faces into the framework of the structure.[17,2] These hexagonal cages can contain larger guest molecules. Although both cage types are present in each structure, it is not necessary that each be filled for a clathrate to be stable. In certain cases, the guest molecule may be too large to fit inside the smaller cage, so these will go empty while the larger cage will be occupied. However, small guests can fill both cages.

Clathrate hydrates have a long literature history, going back approximately 200 years when the first observance was reported to the Royal Society and published in 1811.[26] Davy reported that a compound of chlorine (muriatic oxide) and water had a higher melting point than that of ice and in 1823 Faraday[27] measured its composition to be $Cl_2{*}(H_2O)_{10}$. At the time, clathrates were a bit of a mystery as they did not obey the general rules for chemical compounds that were just being discovered. It wasn't until the early 1950s that the Type

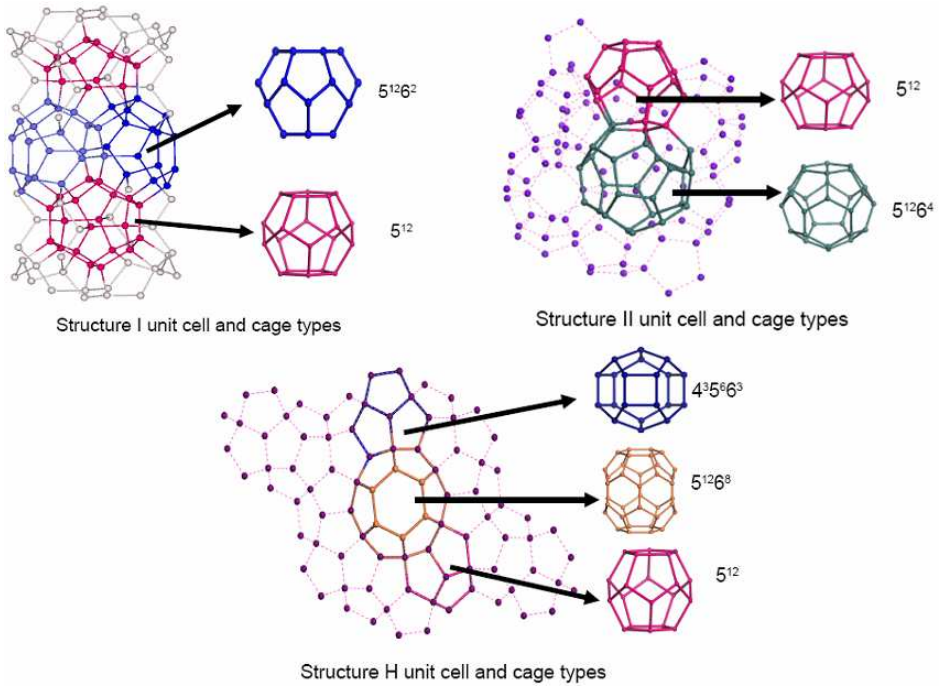

Figure 2.1: The common types of clathrate structures: Type I, Type II and Type H, and their cage types are displayed. Nomenclature: $5^{12}6^4$ indicates a water cage composed of 12 pentagonal and 4 hexagonal faces.

I and Type II structures were identified and characterized,[28,29,30,31,32] helping to provide answers to many of the questions that kept clathrates a mystery during the previous 150 years.

Interest in hydrates began to expand beyond academics in the 1930s when it was discovered that hydrocarbon hydrates form quite easily in gas pipelines, and there was a huge push for research programs dedicated to understanding hydrate formation in the hope of preventing blockages.[33] Unfortunately, the low temperatures and high pressures typical of pipelines place them well within hydrate-forming region, and the issue has given rise to the new field engineering – flow assurance engineering. This field of engineering involves research programs dedicated to designing methods of avoiding blockages, and to prevent the annual loss of property and lives that hydrate blockages cause.

During the last few decades, large amounts of methane hydrate have been discovered in the permafrost regions of the Earth, and off-shore on continental margins.[34] There are differing opinions as to how much natural gas is trapped in clathrates, but even the most conservative estimates suggest that the amount of energy stored in hydrates is equal to twice that of all other fossil fuels combined.[35] Efforts to cost-effectively harvest gas from such deep-lying hydrates are underway, and the rates of depletion of the current energy supply have placed a particular urgency on research in this area. Although it is easy to be excited about the huge amounts of methane deposits, an unfortunate side effect of this much methane is indirectly related to global warming, as it is a far worse greenhouse gas than CO_2, and may an important contributor to the greenhouse phenomena.[36] Increased global temperatures cause methane clathrates to decompose releasing methane gas into the atmosphere and thus contributing to global warming. Given the amount of methane stored in clathrates, this can produce catastrophic consequences, rendering efforts to understand hydrate formation more necessary than ever.

In conclusion, there are a multitude of directions and untapped fields of research for one to consider regarding hydrates, and a comprehensive overview of each possibility is beyond the scope of this work. Interested readers should consider the references listed at the end of

this dissertation. The work presented in this thesis is part of a new NSF initiative designed to foster collaborations among individuals who have not previously worked together, and tackle problems that reach beyond academics and have a wider community impact. The work done under this grant consists of two separate projects and the overall goal is to advance the state knowledge of clathrate hydrates. Each project is discussed in turn, in the following pages.

2.2 COLLABORATIVE RESEARCH IN CHEMISTRY

The NSF CRC Project is a team of chemists, geologists and engineers working together to advance the state knowledge of gas hydrates. We are currently working with principal investigators at UC-Irvine to push toward overall goals of developing new experiments to explore hydrate structures, elucidating the smallest collection of water molecules that form hydrates, gaining a comprehensive understanding of the diffusion of guest molecules between the cages, and a better understanding of hydrate formation. This project also includes a community outreach component of which the purpose is to broaden scientific impact. To establish this, we have developed a week-long workshop for Irvine area high school teachers in which they were able to develop clathrate experiments and simulations for use in the classroom, and we have also developed and maintained a website (http://sag1.chem.pitt.edu/clathrate) in order to foster communication among the collaborators and to communicate our results to a broader audience.

3.0 DEVELOPMENT OF A MODEL POTENTIAL FOR HYDROGEN CLATHRATE SIMULATIONS

3.1 ABSTRACT

The use of hydrogen as an alternative fuel resource has gained much attention recently, although there are practical problems with regards to transportation and storage of hydrogen. Clathrate hydrates have been proposed as means to help overcome some of these obstacles, although hydrogen clathrates are a relatively new discovery. It is known that multiple hydrogen molecules can occupy the different cage types in the Type II clathrate structure, but there is disagreement in the literature about the exact number of hydrogen guest molecules that can occupy the smaller of the two cage types. Previous simulations on such clusters have raised the issue of the importance of including polarization in the force field for molecular dynamics simulations on these structures, although no such force field exists for the interaction between water and hydrogen. To this end, the work in this section is dedicated to the development of such a force field, which is modeled after the charge on a spring water model. The resulting force field was coded into the DLPOLY package for use in hydrogen hydrate simulations.

3.2 INTRODUCTION

As mankind continues to rapidly deplete the readily accessible reserves of natural gas, it is becoming more urgent that we seek out alternative fuel sources, and there has been a push in developing the technology for hydrogen usage as an efficient and environmentally clean fuel. However, effective storage and delivery of hydrogen have proven to be the main (scientific) obstacle holding back the establishment of a hydrogen-based economy.

The most commonly used form of hydrogen in prototype automobiles is liquid hydrogen (density of 70 g/L), but up to 40% of the energy content is spent in liquefying the hydrogen at its low condensation temperature (20 K).[37,38] The second most used form is compressed hydrogen gas, but it has a very low density (15 g/L) at 35 Mpa. Higher pressures could hold a higher hydrogen content, but safety and logistical concerns render this ineffective. Alternative approaches of hydrogen storage include compounds consisting of simple molecules, and research in this area is ongoing and active.[39,1,40]

In considering alternative hydrogen storage mediums, a number of requirements must be addressed: (1) the storage medium must have a high energy content per unit mass; (2) high hydrogen content per unit volume; (3) moderate synthesis pressure (ideally < 400 MPa, which is the pressure that can be reached by a single compressor); (4) near ambient pressure and moderate temperature for storage; (5) easy hydrogen release and (6) environmentally friendly byproducts, if any. Alternative storage methods that meet these requirements have been suggested and include molecular hydrogen adsorption on solids, bonded atomic hydrogen in hydrocarbons or in metal hydrides, and more recently, hydrogen clathrates.[?] Hydrogen clathrates are especially interesting since preliminary research on H_2-H_2O systems has suggested that these compounds can retain up to 15.6 mass % molecular hydrogen, which is significantly above DOE targets.[1,40,41] Additionally, the only byproduct upon release of hydrogen would be water, rendering clathrates an attractive and inexpensive hydrogen storage material.[40,42,26,27,18,33,43,44,45,41,46,47,48,49]

It was previously believed that hydrogen was too small to form a clathrate,[50] but re-

cently, under high pressure conditions, a hydrogen clathrate with the Type II structure was synthesized and characterized by Mao *et al.*,[40] from a liquid at a pressure of 200 MPa and a temperature of 249 K. This structure contains 50 g/L (5.3 mass %) and recovered to ambient pressure (0.1 MPa) at 77 K, successfully demonstrating the potential for hydrogen storage. Furthermore, it was surprising when energy-dispersive x-ray diffraction, Raman and infrared spectroscopy indicated an unusually high H_2/H_2O ratio.[51] The chemical composition could only be accounted for if multiple occupancies of the clathrate cages are assumed. This multiple occupancy is a rare phenomenon for clathrates and the only other system to exhibit this quality is nitrogen clathrates.[3]

One of the most the most pressing issues hindering hydrogen clathrates as a storage medium is that an accurate determination of the number of hydrogen molecules that can occupy the small cage in different pressure-temperature conditions is currently lacking. There have been enormous experimental and theoretical efforts to address this question, but most reports are still conflicting.[1,52,53,54,55] Mao *et al.* suggested that four hydrogen molecules are stored in the large cage, and two are stored in the small cage from optical microscopy and Raman spectroscopy studies. However, neutron scattering studies by Loshkin *et al.*[48] of deuterated water and deuterium at 220 MPa and 200-270 K showed that the small cages hold just one deuterium molecule. Further compounding the confusion are the theoretical studies carried with different methods. Patchkovskii and Tse[52] used Møeller-Plesset perturbation (MP2) theory to model the small (20-molecule water cluster) and large cage (28-molecule cluster) with varying numbers of guest hydrogen molecules. They concluded that the small cages are preferentially occupied by two guest molecules. This disagrees with molecular dynamics simulations by Alavi *et al.*[54] and Inerbaev *et al.*,[55] in which the small cage is preferentially occupied with one guest hydrogen molecule, agreeing with the neutron scattering studies. However, Patchkovskii and Yurchenko showed that if quantum effects are included, the optimal occupancy of the small cage is reduced.[56]

Clearly, this is a topic with unlimited avenues in which to pursue research. The molecular dynamics studies performed thus far on the hydrogen clathrate system have used water

potentials that have either neglected polarization or have included it in an effective manner. It has been shown that in order to accurately model hydrogen-bonded systems (such as clathrate structures), it is necessary to include polarization in the model potential.[57,58,59,60] Therefore, the specific goal of the work here is to develop a force field for in use molecular dynamics simulations that accounts for polarization, which will ultimately be used to study the stability of the structure II hydrogen clathrate as a function of hydrogen occupancy.

The development of this force field (which will be referred to as COS_{hyd} for the remainder of this document), its implementation into the DLPOLY package, and initial molecular dynamics simulations on the system for testing the COS_{hyd} are discussed in the following pages. It is hoped that research carried out here will be beneficial to a comprehensive understanding of the chemical, structural and dynamical properties of hydrogen hydrates with the ultimate goal of contributing to the advancement of alternative energy technology.

3.3 THEORETICAL BACKGROUND

3.3.1 Molecular dynamics simulations

The time dependent behavior of molecular systems can be calculated with molecular dynamics (MD), through the integration of Newton's equations of motion:

$$m_i \frac{d^2\mathbf{r_i}}{dt^2} = \mathbf{F_i}. \tag{3.1}$$

The force can also be expressed as the gradient of the potential energy,

$$F_i = -\nabla_i V. \tag{3.2}$$

Combining these two equations yields

$$-\frac{dV}{dr_i} = m_i \frac{d^2 r_i}{dt^2} \tag{3.3}$$

Newton's equations relate the derivative of the potential energy to the changes in position as a function of time. The result is a trajectory of positions and velocities as a function of time, where m_i is the mass of particle i, $\boldsymbol{r}_i$ is its position and $\boldsymbol{F}_i$ is the force acting on it. From the trajectory, it is possible to obtain the average values of properties of interest. In practice, the equations of motion are many-body in nature and cannot be solved analytically. For these systems, numerical integration techniques such as the Verlet algorithm[61] are employed. This algorithm assumes that the positions and velocities can be approximated as Taylor series expansions of the coordinate of a particle around time, t.

$$\begin{aligned}
\mathbf{r}(t+\delta t) &= \mathbf{r}(t) + \delta t \mathbf{v}(t) + \frac{1}{2}\delta t^2 \mathbf{a}(t) + \cdots \\
\mathbf{v}(t+\delta t) &= \mathbf{v}(t) + \delta t \mathbf{a}(t) + \frac{1}{2}\delta t^2 \mathbf{b}(t) + \cdots \\
\mathbf{a}(t+\delta t) &= \mathbf{a}(t) + \delta t \mathbf{b}(t) + \frac{1}{2}\delta t^2 \mathbf{c}(t) + \cdots,
\end{aligned} \tag{3.4}$$

where $\mathbf{v}$ is the velocity, $\mathbf{a}$ is the acceleration, $\mathbf{b}$ is the third derivative and so on.

The Verlet algorithm uses positions and accelerations at time t and the positions from t-δt to calculate new positions at time t+δt. The relationship between these quantities and the velocities can be expressed as follows:

$$\begin{aligned}
\mathbf{r}(t+\delta t) &= \mathbf{r}(t) + \delta t \mathbf{v}(t) + \frac{1}{2}\delta t^2 \mathbf{a}(t) + \cdots \\
\mathbf{r}(t-\delta t) &= \mathbf{r}(t) - \delta t \mathbf{v}(t) + \frac{1}{2}\delta t^2 \mathbf{a}(t) - \cdots.
\end{aligned}$$

Summing these equations gives:

$$\mathbf{r}(t+\delta t) = 2\mathbf{r}(t) - \mathbf{r}(t-\delta t) + \delta t^2 \mathbf{a}(t) \cdots . \tag{3.5}$$

The acceleration is calculated from the force on the atom at time t. While the velocities do not explicitly appear in the Verlet algorithm, they can be calculated in a variety of ways. One of the simplest ways is to divide the difference in positions at t+δt and t-δt by $2\delta t$. The resulting equation is then:

$$\mathbf{v}(t) = \frac{\mathbf{r}(t+\delta t) - \mathbf{r}(t-\delta t)}{2\delta t}. \tag{3.6}$$

The advantages of this algorithm are that it is straightforward and its storage requirements are small, although the precision is sometimes compromised. Variations on the Verlet algorithm have subsequently been developed. One such variation is the velocity Verlet algorithm, which gives positions, accelerations and a velocity computed at equal times, and does not compromise precision:

$$\mathbf{r}(t+\delta t) = \mathbf{r}(t) + \delta t \mathbf{v}(t) + \frac{1}{2}\delta t^2 \mathbf{a}(t) + \cdots \tag{3.7}$$

The velocities are:

$$\mathbf{v}(t+\delta t) = \mathbf{v}t + \frac{1}{2}\delta t[\mathbf{a}(t) + a(t+\delta t)]. \tag{3.8}$$

The velocities are computed after the new positions, and the new forces come from the new positions.

3.3.2 Force fields in molecular dynamics simulations

At the basis of molecular dynamics methods is an interaction potential, which refers to a functional form for the potential energy of a system, and a set of parameters that are chosen so that the resulting energies agree with experimental data or with *ab initio* quantum mechanical results. The interaction potential is a sum of terms describing the energy required for distorting a molecule from its equilibrium position.

$$V_{total} = V_{str} + V_{bend} + V_{tors} + V_{dispersion} + V_{repulsion} + V_{electrostatics} + E_{cross} \tag{3.9}$$

E_{str} is the energy for stretching for stretching a bond between two atoms, E_{bend} is the energy required for bending an angle, the torsional energy for rotation around a bond is represented by E_{tors}, $E_{electrostatics}$, $E_{dispersion}$, $E_{repulsion}$ describe the non-bonded atom-atom interactions and E_{cross} describes the coupling between the stretching, bending and torsional terms.

A major concern in molecular dynamics simulations is obtaining a quality force field while maintaining reasonable computational costs. In this light, most force fields limit intramolecular interactions, and are designed for rigid molecules. The resulting intermolecular potential

is then a sum of pairwise electrostatic and Van der waals terms between the molecules of interest, which can be written as

$$V_{total} = V_{electrostatic} + V_{polarization} + V_{repulsion} + V_{dispersion} \tag{3.10}$$

The various components to the total interaction energy are discussed in the following sections.

3.3.2.1 Electrostatics and polarization Electrons are more attracted to electronegative elements than to less electronegative elements, giving rise to an uneven charge distribution. This charge distribution can be represented by point charges at various locations on the molecule. The electrostatic interaction energy arising from attractions and repulsions between charges on different sites can then be expressed with Coulomb's law:

$$V_{ele} = \sum_{i=1}^{N_A} \sum_{j=1}^{N_B} \frac{q_i q_j}{4\pi\epsilon_0 R_{ij}}. \tag{3.11}$$

Where N_A and N_B are the numbers of point charges in the two molecules. In general, the number of point charges and the values of the charges are chosen so as to reproduce the experimental or *ab initio* values of the dipole and quadrupole moment of the molecule of interest as determined either by experiment, or high level *ab initio* quantum calculations. The quadrupole moment of a system of charges is defined as

$$\Theta_{\alpha\beta} = \frac{1}{2} \sum_i q_i \left(3 r_{i\alpha} r_{i\beta} - r_i^2 \delta_{\alpha\beta}\right) \tag{3.12}$$

Electrostatic interactions also arise from changes in the charge distribution of a molecule or atom that are caused by an external electric field (usually caused by neighboring molecules), which is polarization. The primary effect of an external electric field is to induce a dipole moment in the molecule, which is proportional to the electric field with a constant of proportionality, the polarizability, α:

$$\mu_{\mathbf{ind}} = \alpha \mathbf{E} \tag{3.13}$$

It is often difficult to model polarization effects as they tend to be many-body in nature. For example, the induced dipole on molecule A will affect the charge distribution on

another molecule, B. The electric field at A will in turn be affected due to the dipole on B. The presence of other molecules will also influence the interaction. For example, a third molecule may reduce the size of the electric field on the second molecule and thereby lower the induction energy contribution to the force field energy. It is these many-body effects that renders polarization effects computationally demanding. In many cases, such three-body effects are included implicitly in the pair potential by using water dipole moments that are larger than the experimental gas phase value. In other models, the charges are constant and cannot change in response to a change in environment which arises from movements of atoms during a simulation.

3.3.2.2 van der Waals interaction The remaining component to the total molecular interaction energy is the van der Waals interaction energy which is a sum of the repulsive and dispersive interactions. Dispersion forces are the weak attractive forces between molecules arising from small instantaneous dipoles that occur as the electrons move about the nucleus. Although electrons are in constant motion, the motions of electrons on atom (or molecule) affects the motions of the electrons on another atom (or molecule). An instantaneous dipole in a molecule can induce a dipole in neighboring atoms, giving rise to an attractive interaction. The forces were first explained by Fritz London in 1930[59] and are often referred to as London forces.

While dispersion forces act at long distances, repulsive forces arise at short distances and can be explained in terms of the Pauli principle, which states that no two electrons in an atom can have the same set of quantum numbers. As the distance between two atoms decreases, the repulsion energy increases as it is unfavorable for two electrons to occupy the same orbital space.

The dispersive and repulsive interactions can be modeled in with a force field that includes a simple empirical expression. In a simulation, it is desirable that this expression be calculated rapidly, and the best known function is the *Lennard-Jones 12-6* function:

$$V_{vdw} = 4\varepsilon \left[\left(\frac{\sigma}{r} \right)^{12} - \left(\frac{\sigma}{r} \right)^{6} \right] \tag{3.14}$$

3.3.2.3 Force fields for clathrate structures Although this research focuses exclusively on hydrogen clathrate systems, it is important to point out that work done on other clathrate systems, particularly on methane systems, can provide insight and direction for studies on hydrogen systems. As previously discussed, the significance of methane hydrates is quite obvious, and this system has been the focus of numerous computational studies. With exception of recent calculations[62,63] using the TIP4P-FQ[64] model, which allows for in-plane polarization, most of the molecular dynamics simulations on these systems have employed models that account for polarization in an effective two-body manner. However, in their work on methane hydrates, Jiang *et al.*[65] have shown the deficiencies of such non-polarizable (or in-plane polarizable) models in producing correct descriptions of clathrate structures. More specifically, the authors demonstrate that the AMOEBA and COS/G2 polarizable models more accurately predict the experimental values for properties such as the temperature dependence of the lattice constants, radial distribution functions, and vibrational spectra.[66,5]

The AMOEBA water model provides a realistic description of both bulk water and water clusters;[67,68] however, its computational demands and its inability to run in parallel made it an inappropriate choice for Type II hydrogen clathrate simulations. Instead, the COS/G2 polarizable model[5] was used for H_2O-H_2O interactions. Previous simulations by Ripmeester *et al.*[54] on this system have made use of a rigid, non-polarizable model of hydrogen, using point charges for the electrostatics and adopting a *Lennard-Jones* function for describing the van der Waals interactions (from here, this method will be referred to as the Ripmeester potential). However, this method poorly reproduces *ab initio* results for selected one dimensional cuts through the H_2O-H_2 and H_2-H_2 potential energy surface. Therefore, the purpose of this research was to develop and implement a polarizable model for hydrogen for use in hydrogen hydrate simulations, using the COS/G2 water model as a guide. Such a force field does not currently exist in the literature, and the importance of hydrogen hydrates places an urgency on understanding the properties of this system. An accurate model potential will ultimately help in clarifying the pressing questions regarding

hydrogen clathrates, especially regarding the occupancy numbers in the small cage. The details of developing the model, of coding it into DLPOLY,[69] and the results of preliminary simulations are discussed in the following sections.

3.4 THEORETICAL METHODS: DEVELOPING THE HYDROGEN CLATHRATE FORCE FIELD

3.4.1 Force field for H_2O-H_2O interactions

Due to its biological importance, water has been extensively studied by computational methods. There has been an exhaustive effort put forth by the scientific community in developing a model potential to accurately describe water. A historical overview of the development of such a potential can be found in the literature.[70,71,72,73,74,75,76,77,78,79] For the most part, these models make use of pairwise potentials and include many body effects implicitly. Other force fields use fixed partial charges and include many-body effects in an average, mean field manner. Some of these interaction models for water include the widely used simple point charge (SPC) potential developed by Bernal and Fowler,[80] which was improved by Stillinger and Rachman.[81] Berendsen *et al.*[82] and Jorgensen *et al.*[83] expanded on this approach to develop a transferable interaction potential (TIP) that uses fractional charges located on atomic or symmetry sites of the H_2O molecule to describe the electrostatic interactions, and a Lennard-Jones potential between the oxygen atoms to describe dispersion and repulsion contributions. However, it has been widely recognized that these types of non-polarizable water models do not accurately describe the properties of water molecules in different environments. There has therefore been a push in developing polarizable models, and the three main approaches of doing so have been discussed extensively in the literature: polarizable point dipole,[5] fluctuating charge,[84,64] and Drude oscillator methods.[85]

For the hydrogen hydrate simulations discussed here, it was necessary to employ a model for water than could be extended to water-hydrogen and hydrogen-hydrogen interactions.

Additionally, the model needed to be able to run in parallel, and it was necessary that the model be included in a software package for which the code could be modified and recompiled. For these reasons, and because it proven successful in reproducing experimental data of methane hydrates, the COS/G2[5] water model was used.

In the COS/G2 model, water has one polarizable center, which is a virtual atomic center, the M-site, that is located 0.22 Å from the oxygen atom along the bisector of the HOH angle, as shown in Figure 3.1. An induced dipole moment on each M-site located at $\mathbf{r}_i$ is determined by Equation 3.15

$$\mu_i^{ind} = \alpha_i(\mathbf{E}_i^0 + \mathbf{E}_i^p) \tag{3.15}$$

where $\mathbf{E}_i^0$ is the electric field due to the permanent atomic charges and $\mathbf{E}_i^p$ is the field due to other induced dipoles.

The induced dipole is represented by two charges: one charge is located on the M-site, and the other charge belongs to a mobile polarization particle that is harmonically attached to the M-site by a spring. The force constant for the spring is related to the polarizability and is given by $\frac{q_{pol}^2}{\alpha_i}$. This method of representing dipoles requires that an addition term be included in the intermolecular potential energy expression, which corresponds to the energy cost of distorting the molecule to its polarized state.

$$V_{pol} = \frac{1}{2}\sum_{i=1}^{N}\frac{\mu_{\mathbf{i}}^{\mathbf{ind}}}{\alpha_i} \tag{3.16}$$

The van der Waals terms for the H_2O-H_2O interaction are accounted for in the COS/G2 model and are expressed with a *Lennard-Jones 12-6* function, the parameters for which can be found in the paper by Yu *et al.*[5]

3.4.2 Force field for H_2O-H_2 and H_2-H_2 interactions

A polarizable force field describing the H_2O-H_2 and H_2-H_2 interactions does not currently exist in the literature, and the development of such a force field is not a trivial undertaking.

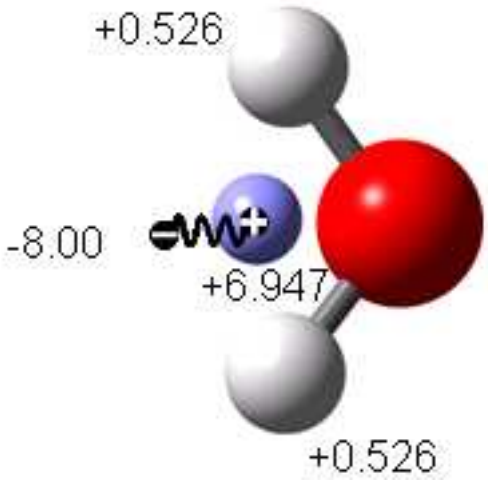

Figure 3.1: Schematic diagram of the COS/G2 model for water. The electrostatic properties are represented by four interaction sites; the two hydrogen atoms, the M-site, and a polarization charge, which is connected to the M-site by a spring. There is one van der Waals interaction site at the oxygen atom.

As a starting point,*ab initio* quantum mechanics calculations at the MP2/aug-cc-pV5Z[86] level were carried out for several one-dimensional cuts through the multidimensional potential energy surface of both the H_2O-H_2 and H_2-H_2 systems. The selected orientations of both systems are shown in Figure 3.2 and Figure 3.3, and the one dimensional potential energy cuts are shown in Figure 3.4 and 3.5. The global minimum for the H_2O-H_2 system is Structure A, and the global minimum for the H_2-H_2 system is the perpendicular configuration. The potential energy surfaces provided a guide for building the molecular dynamics force field. In particular, the total interaction of each complex as a function of distance should accurately and precisely match the surfaces generated by the *ab initio* calculations. In order to do this, it is necessary to consider each component to the total interaction energy separately.

The electrostatic energy is determined by Coulomb's law for each system, and the values and locations of the three point charges for water are those of the COS/G2 model. The point charges for hydrogen were chosen so as to reproduce the experimental quadrupole value[87] of $2.172 \times 10^{-40} Cm^2$, and were placed on each hydrogen atom, and on an M-site in the middle of the H_2 bond. The polarization for H_2, 0.771 $Å^3$, was determined by *ab initio* calculations at the MP2/aug-cc-pV5Z level, which closely matches the experimental value[87] of 0.787 $Å^3$, and provides a force constant, k of 7208.1 $\frac{kJ}{mol Å^2}$. These parameters define the electrostatic and polarization contributions to the total interaction energy. The remaining component to the total interaction energy is the van der Waals interaction energy.

The interaction between water and hydrogen was modeled with a Buckingham[88] function (Equation 3.17 for H_2O-H_2 and Equation 3.18 for H_2-H_2), as it became apparent during this work that an exponential term was far superior to the *Lennard-Jones* function for modeling the repulsive interactions. A repulsive center was placed on the M-site of the H_2 molecule, on each water hydrogen and on the oxygen atom; a dispersion site was placed on the oxygen atom and on the M-site of H_2 for the H_2O-H_2 and H_2-H_2 complexes. As discussed by Tang and Toennies,[89] the dispersive functions should be damped at short distances. In this work,

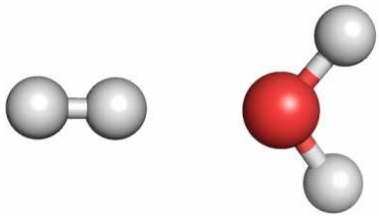

(a) Structure **A**

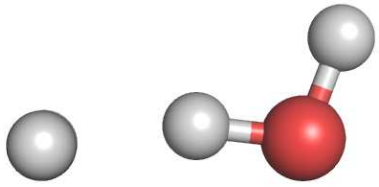

(b) Structure **B**

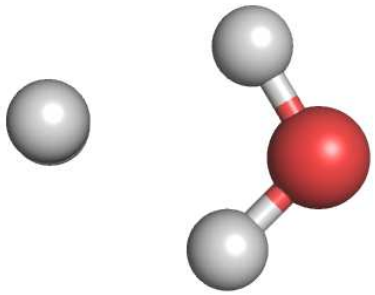

(c) Structure **C**

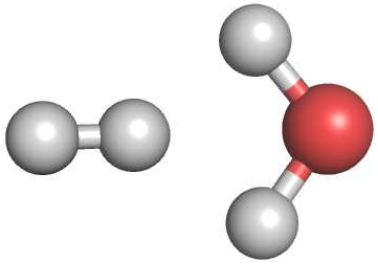

(d) Structure **D**

Figure 3.2: Selected geometries of the H_2O-H_2 complex for which cuts through the one-dimensional potential energy surface were determined by varying the distance between the monomers.

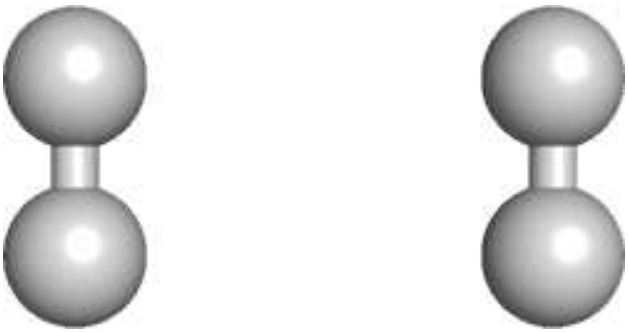

(a) **Parallel**

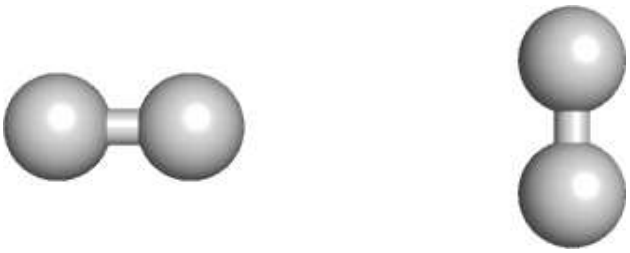

(b) **Perpendicular**

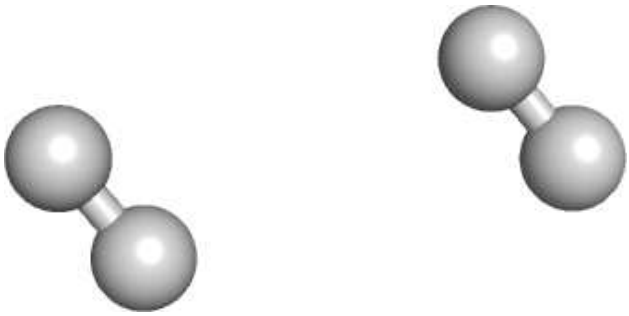

(c) **Slipped**

Figure 3.3: Selected geometries of the H_2-H_2 complex for which cuts through the one-dimensional potential energy surface were determined by varying the distance between the monomers.

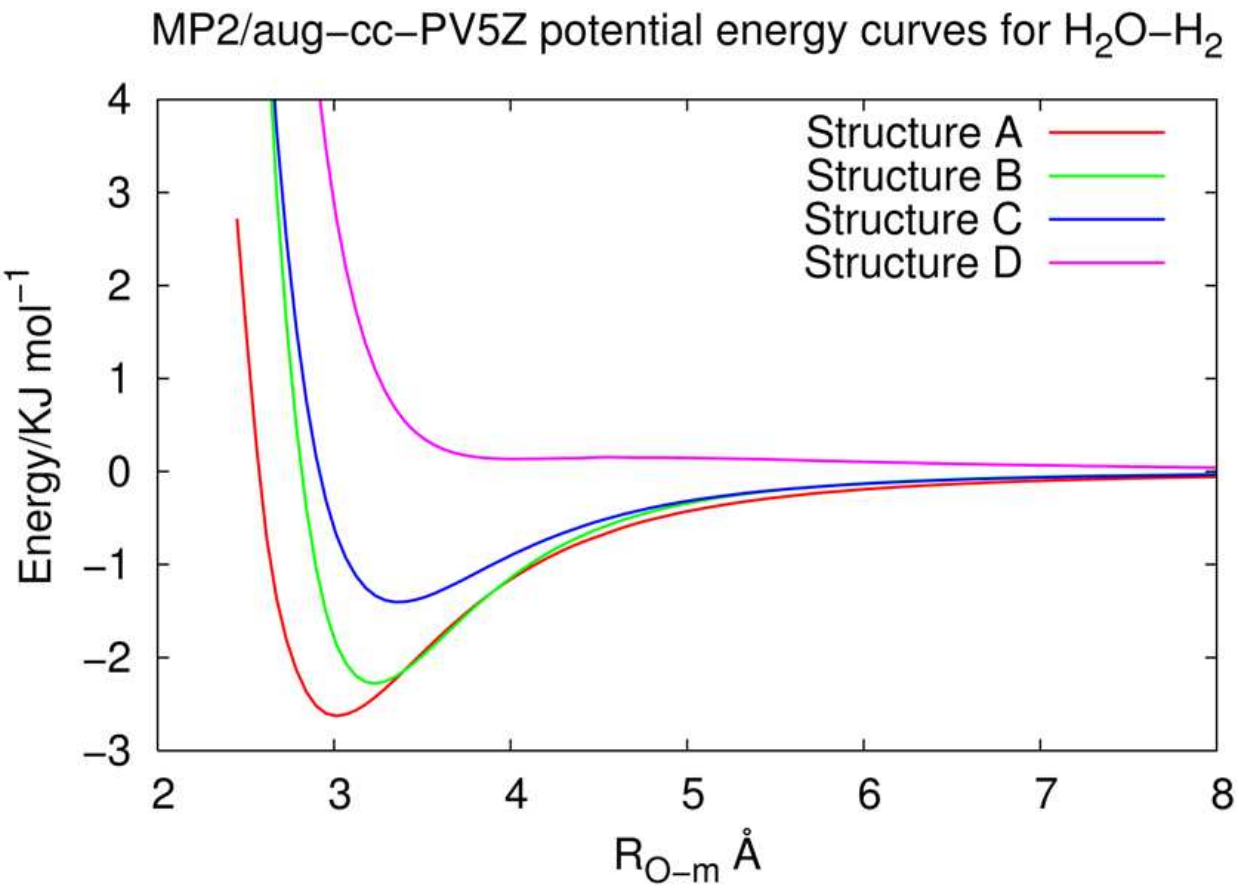

Figure 3.4: Potential energy curves for the selected geometries of the H_2O-H_2 system at the MP2/aug-cc-pV5Z level. The monomers in this and subsequent figures are rigid.

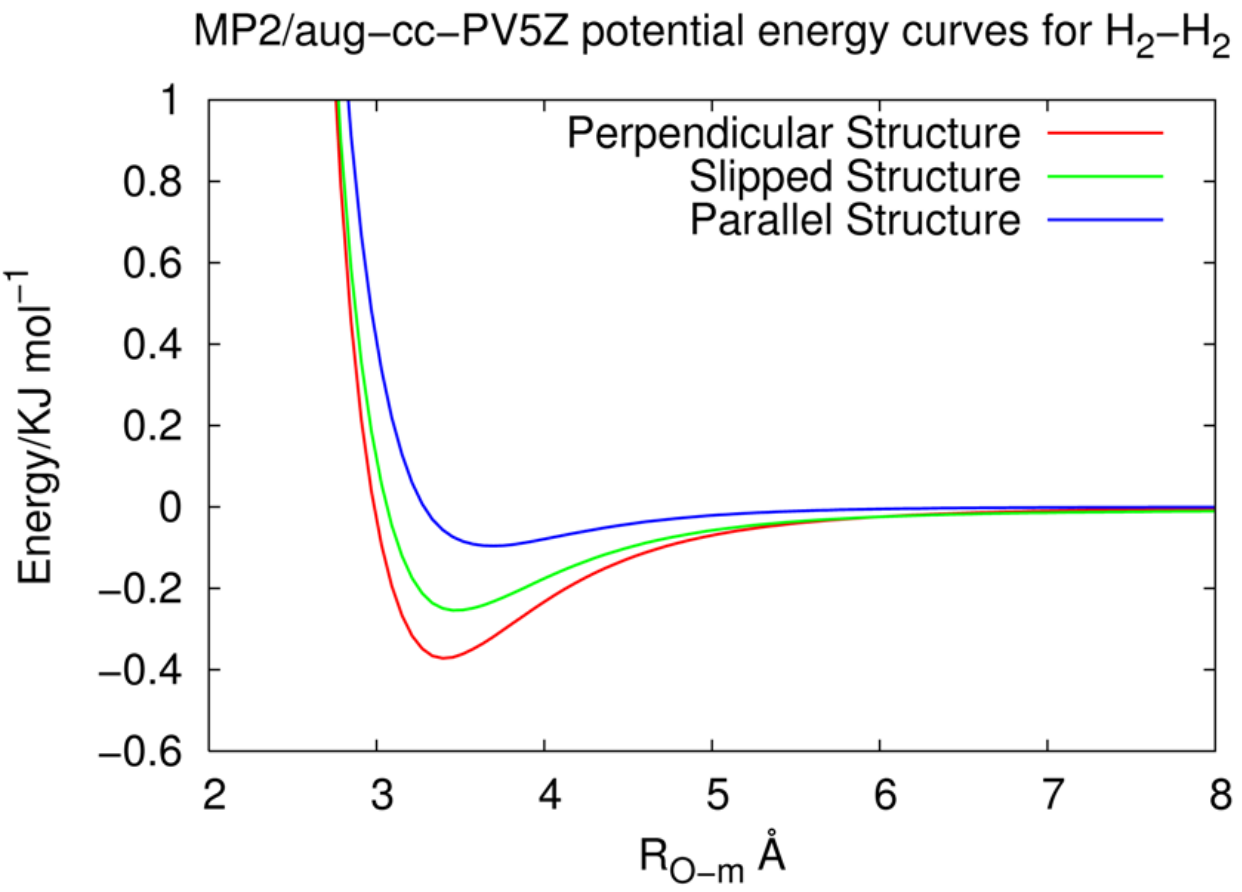

Figure 3.5: Potential energy curves for the selected geometries of the H_2-H_2 system at the MP2/aug-cc-pV5Z level.

the damping function of Tang and Toennies[89] was used ($f_6(\delta, r_{OM})$ and $f_6(\delta, r_{MM})$).

$$V_{vdw} = A_{OM} e^{-B_{OM} r_{OM}} + \sum A_{HM} e^{-B_{HM} r_{HM}} - f_6(\delta, r_{OM}) \frac{C_6^{OM}}{r_{OM}^6} \tag{3.17}$$

$$V_{vdw} = A_{MM} e^{-B_{MM} r_{MM}} - f_6(\delta, r_{MM}) \frac{C_6^{MM}}{r_{MM}^6} \tag{3.18}$$

$$f_6(\delta, r_{OM}) = 1 - e^{-\delta r_{OM}} \sum_{n=0}^{6} \frac{(\delta r_{OM})^n}{n!} \tag{3.19}$$

$$f_6(\delta, r_{MM}) = 1 - e^{-\delta r_{MM}} \sum_{n=0}^{6} \frac{(\delta r_{MM})^n}{n!} \tag{3.20}$$

The parameters for H_2O-H_2 and H_2-H_2 were found by fitting the $E_{total} - E_{electrostatic} - E_{polarization}$ residual, where E_{total} is the *ab initio* MP2/aug-cc-pV5Z energy of the dimer of interest as a function of intermolecular distance. The repulsive parameters A and B, the dispersion coefficient C_6, and the damping parameter, δ, were found by using a least squares fitting method included in the Mathematica software package.

3.4.3 The resulting force field

The resulting force field for H_2 is shown in Figure 3.6, and the energy curves generated from this model are shown in Figures 3.7, 3.8, 3.9, and 3.10 for each of the H_2O-H_2 and H_2-H_2 geometries considered. As can be seen, the potential agrees quite well with the *ab initio* curves. The electrostatic and polarization contributions are also shown.

For comparison, the potential energy surfaces generated by the method employed by Ripmeester *et al.* are displayed in Figure 3.14. In these potentials, the extended simple point charge model (SPC/E)[90] was used as the intermolecular potential for H_2O-H_2O interactions. The isotropic van der Waals potential was used to describe H_2-H_2 and H_2O-H_2 interactions, and a *Lennard-Jones* potential was used to describe H_2-H_2 interactions. The intermolecular potential parameters between unlike atoms were determined from Lorenz-Bertholet combination rules. It is clear that this potential does not reproduce the *ab initio* curves very

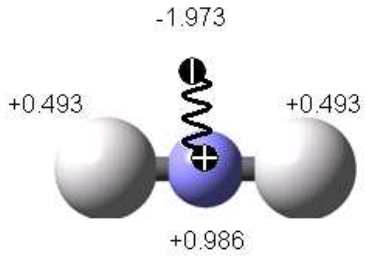

Figure 3.6: Schematic diagram of the COS_{hyd} model for hydrogen. The electrostatic properties are represented by three interaction sites at the two hydrogen atoms and the M-site, and the polarization charge, which is connected to the M-site by a spring. There is one van der Waals interaction site at the center of mass M-site.

well. Therefore, including polarization and using a better function for the repulsive interactions leads to a more accurate description of the force field, without significantly increasing computational expense.

The COS_{hyd} model has been coded into the DLPOLY molecular dynamics simulation package for use in hydrogen hydrate simulations. Molecular dynamics simulations on the Type II hydrogen clathrates with different guest H_2 occupancies were carried out to study the stability of the system. The results of these simulations are discussed in the following sections.

3.5 THEORETICAL METHODS: SIMULATIONS WITH THE HYDROGEN CLATHRATE FORCE FIELD

As discussed in the introduction, there has been debate in the literature about the stability of the structure II hydrogen clathrate with regards to the number of hydrogen molecules that can exist inside the small dodecahedral cage. Because of this, and to be able draw com-

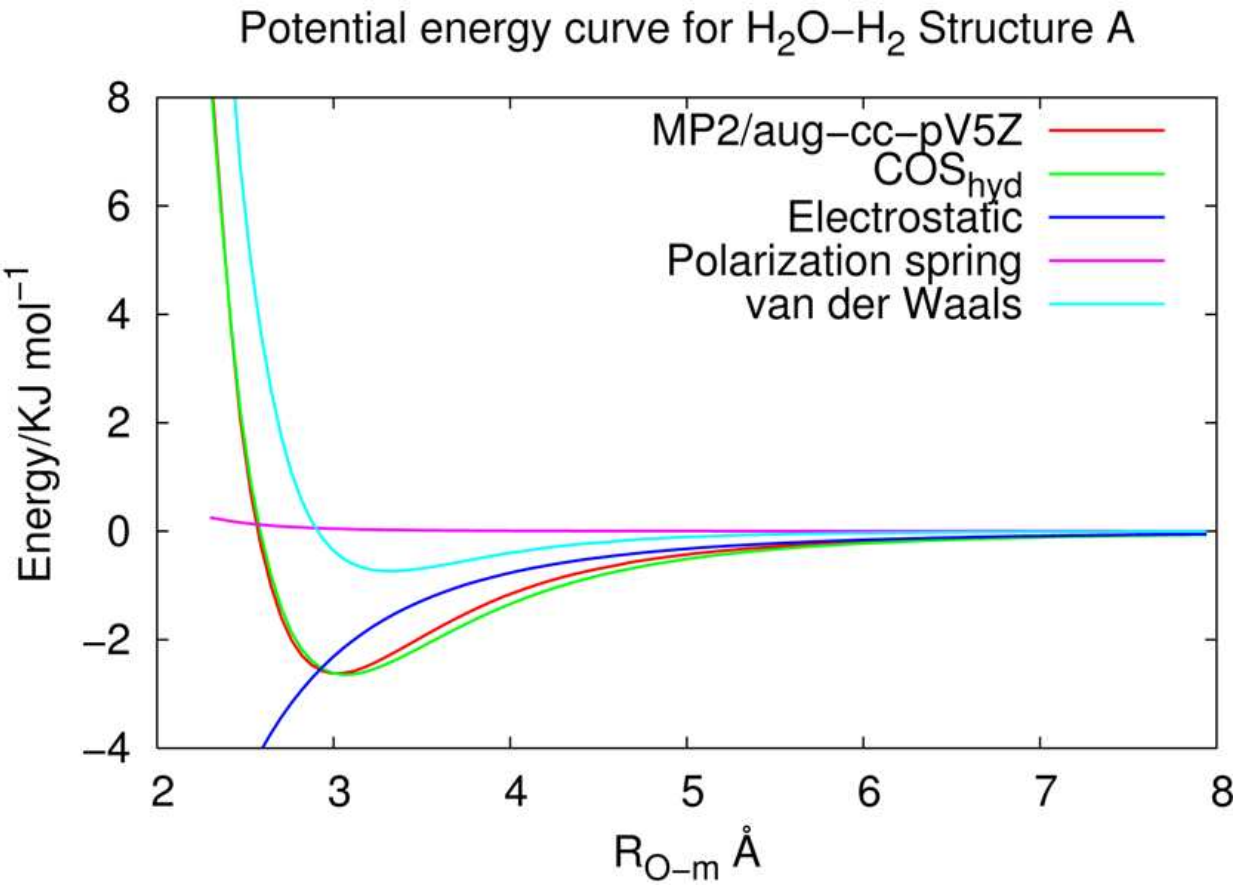

Figure 3.7: The binding energy of the Structure **A** dimer as a function of intermolecular distance. The COS_{hyd} interaction energy agrees quite well with the PES generated by MP2/aug-cc-pv5Z calculations. The electrostatic, polarization and van der Waals contribution to the interaction are also shown. (The polarization curve corresponds to the energy cost of separating the two charges representing the induced dipole.)

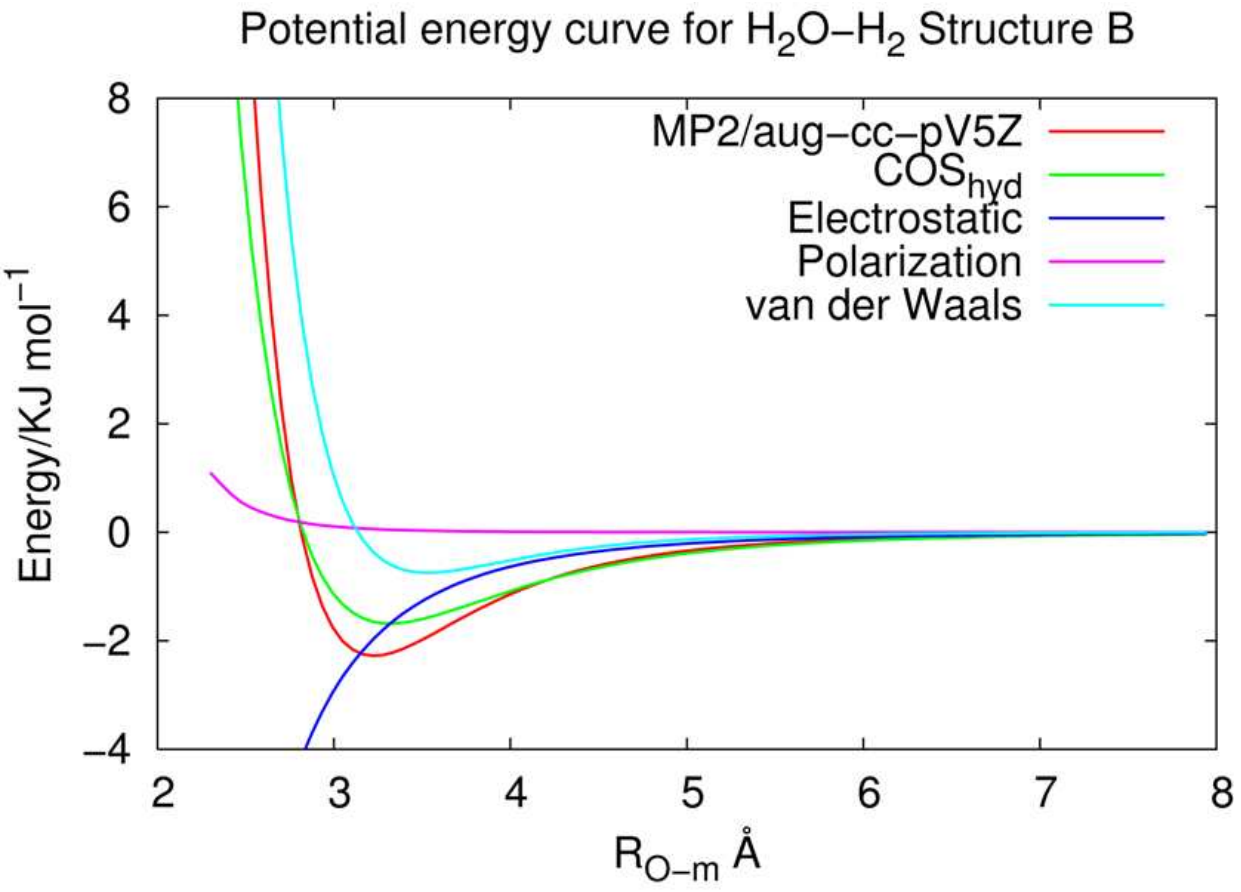

Figure 3.8: The binding energy of the Structure **B** dimer as a function of intermolecular distance. The COS_{hyd} interaction energy agrees quite well with the PES generated by MP2/aug-cc-pv5Z calculations. The electrostatic, polarization and van der Waals contribution to the interaction are also shown. (The polarization curve corresponds to the energy cost of separating the two charges representing the induced dipole.)

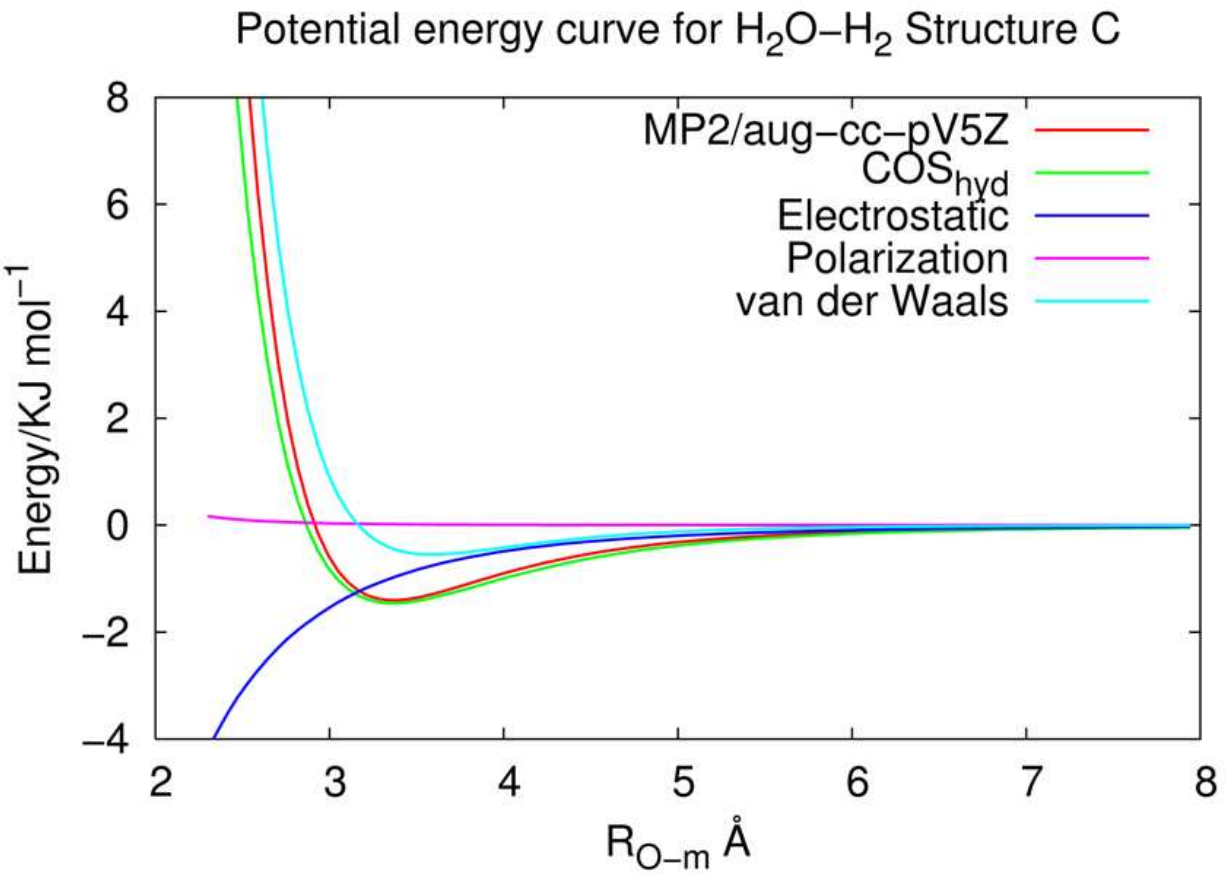

Figure 3.9: The binding energy of the Structure **C** dimer as a function of intermolecular distance. The COS_{hyd} interaction energy agrees quite well with the PES generated by MP2/aug-cc-pv5Z calculations. The electrostatic, polarization and van der Waals contribution to the interaction are also shown. (The polarization curve corresponds to the energy cost of separating the two charges representing the induced dipole.)

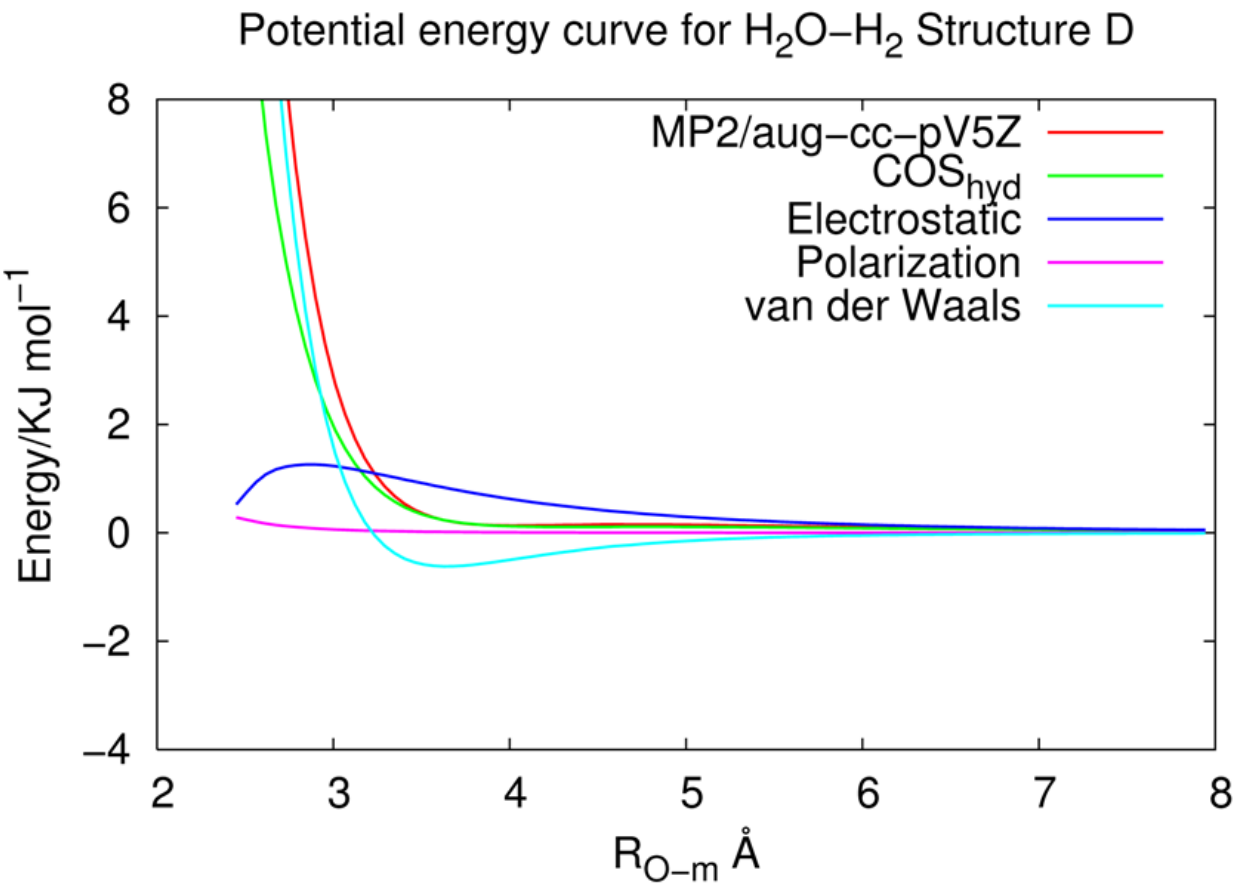

Figure 3.10: The binding energy of the Structure **D** dimer as a function of intermolecular distance. The COS_{hyd} interaction energy agrees quite well with the PES generated by MP2/aug-cc-pv5Z calculations. The electrostatic, polarization and van der Waals contribution to the interaction are also shown. (The polarization curve corresponds to the energy cost of separating the two charges representing the induced dipole.)

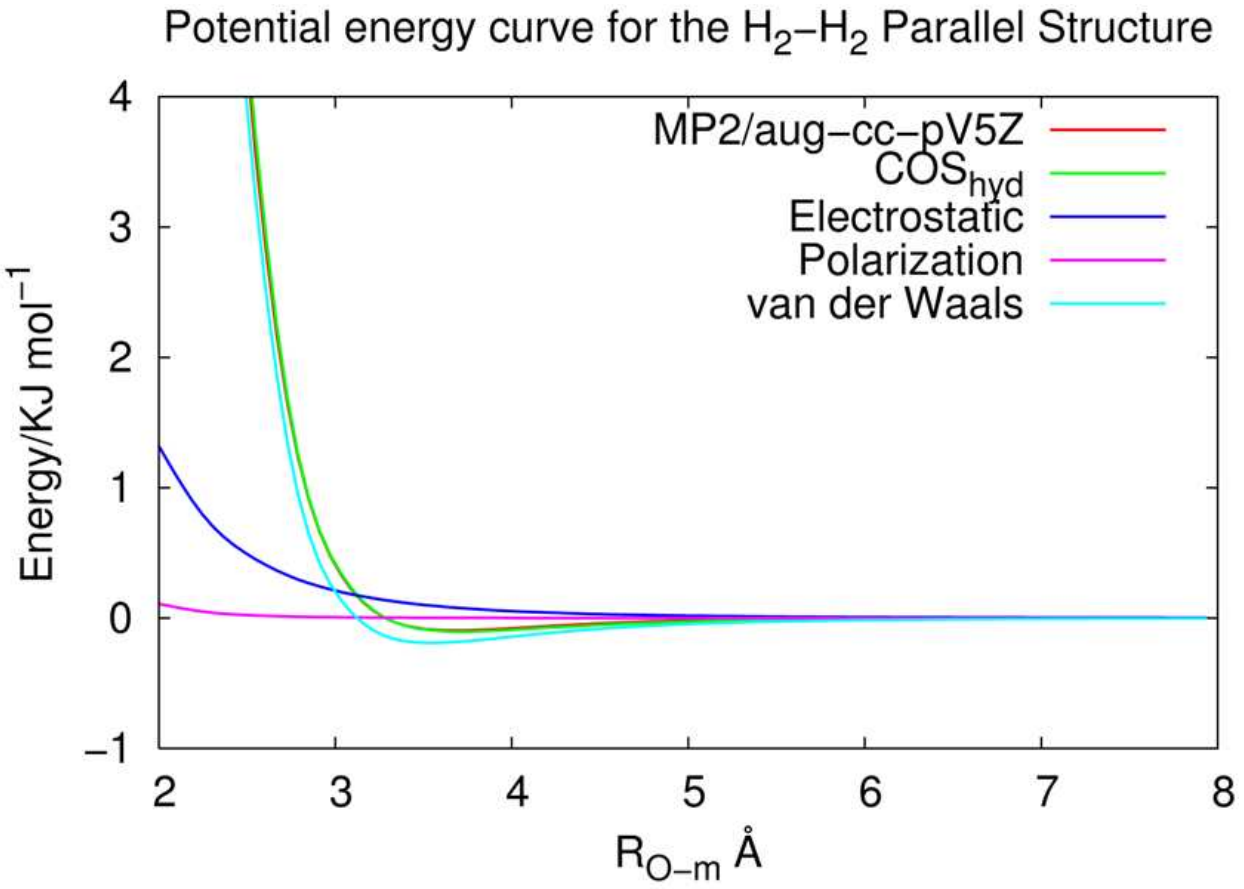

Figure 3.11: The binding energy of the **Parallel** H_2-H_2 dimer as a function of intermolecular distance. The COS_{hyd} interaction energy agrees quite well with the PES generated by MP2/aug-cc-pv5Z calculations. The electrostatic, polarization and van der Waals contribution to the interaction are also shown. (The polarization curve corresponds to the energy cost of separating the two charges representing the induced dipole.)

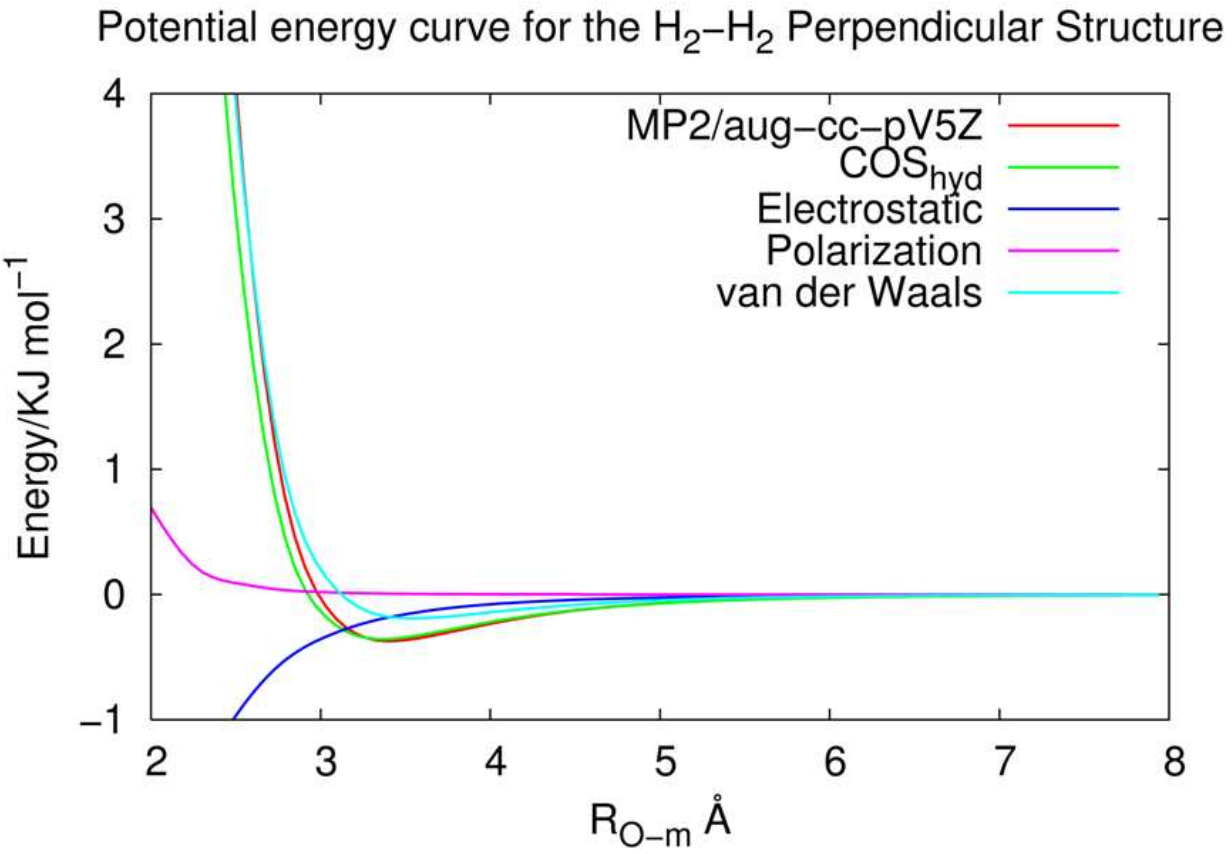

Figure 3.12: The binding energy of the **Perpendicular** H_2-H_2 dimer as a function of intermolecular distance. The COS_{hyd} interaction energy agrees quite well with the PES generated by MP2/aug-cc-pv5Z calculations. The electrostatic, polarization and van der Waals contribution to the interaction are also shown. (The polarization curve corresponds to the energy cost of separating the two charges representing the induced dipole.)

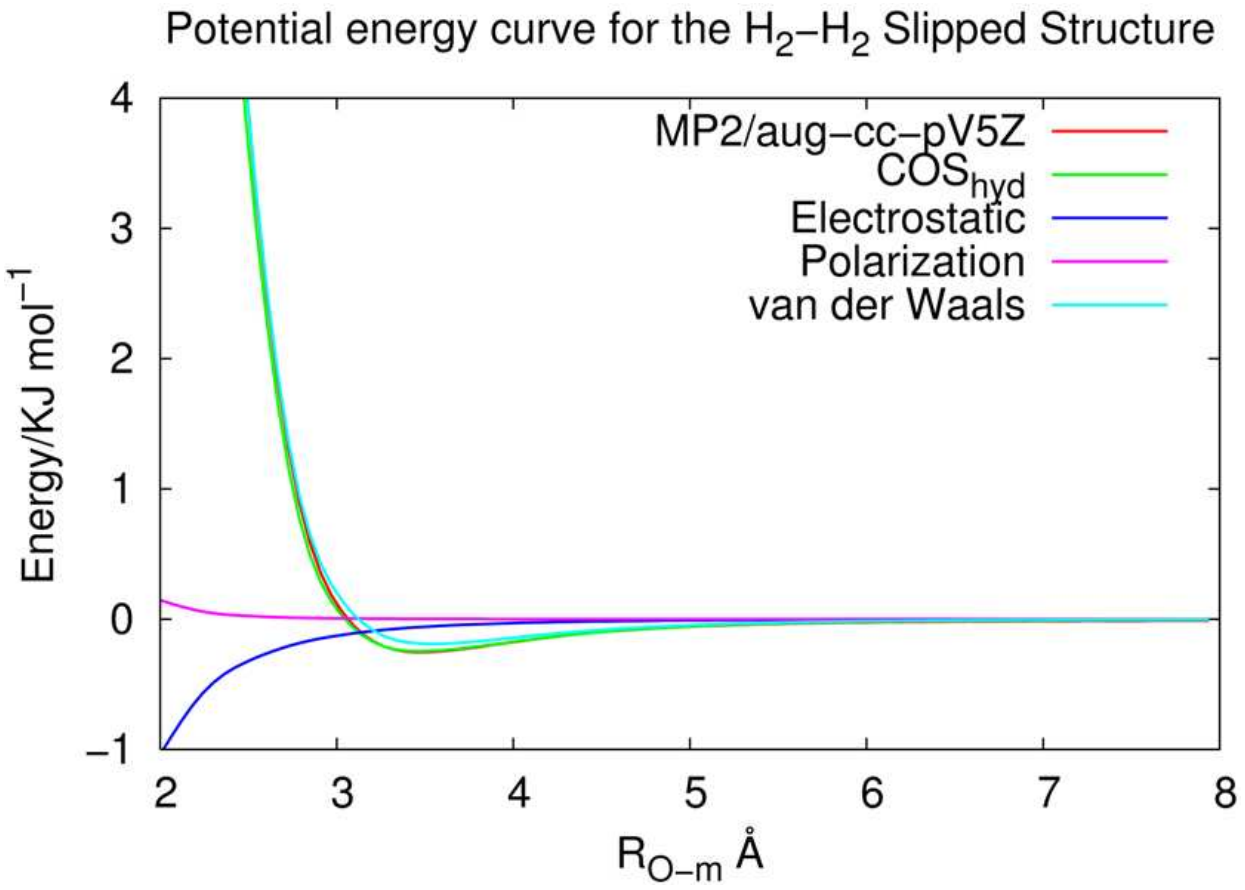

Figure 3.13: The binding energy of the **Slipped** H_2-H_2 dimer as a function of intermolecular distance. The COS_{hyd} interaction energy agrees quite well with the PES generated by MP2/aug-cc-pv5Z calculations. The electrostatic, polarization and van der Waals contribution to the interaction are also shown. (The polarization curve corresponds to the energy cost of separating the two charges representing the induced dipole.)

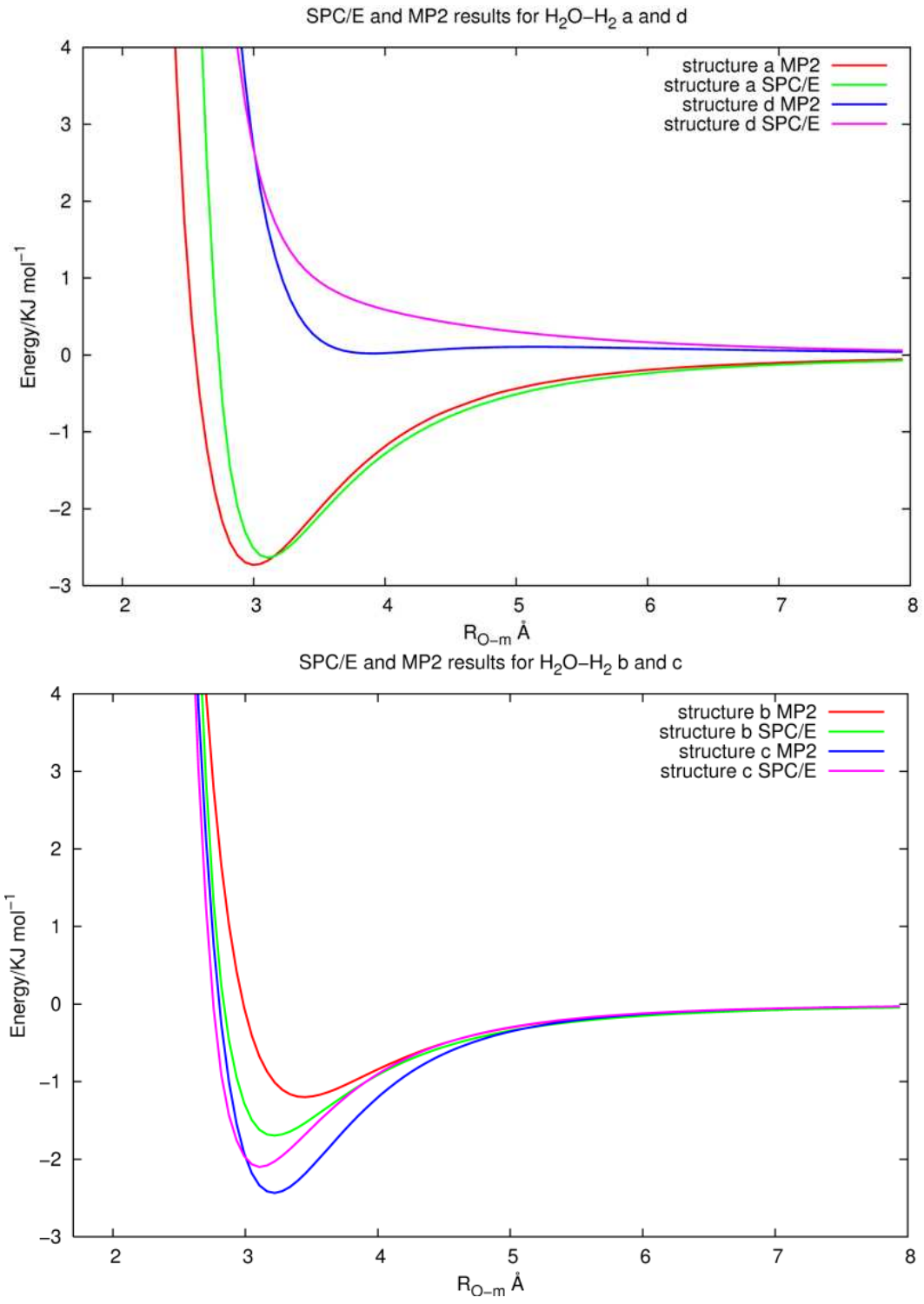

Figure 3.14: *ab initio* and SPC/E potential energy curves for H_2O-H_2 and H_2-H_2 structures

parisons between Ripmeester's model and the newly developed COS_{hyd} model, simulations of the Type II hydrogen clathrate with varying hydrogen occupancies were performed.

3.5.1 Cage occupancy vs. stability

The charge on a spring (COS/G2) model is used as the intermolecular potential for water, and the newly developed model, COS_{hyd}, was used for the H_2O-H_2 and H_2-H_2 interactions.

Constant-pressure-constant-temperature molecular dynamics simulations were performed with the Nose-hoover barostat algorithm[91,92] on $2X2X2$ Type II hydrogen clathrate supercells with the DL-POLY program (version 2.16) after it had been recoded and recompiled for the new potential. The relaxation times for the thermostat and barostat were 0.5 and 2.0 ps, respectively. The equations of motion were integrated with a time step of 1 fs with the velocity Verlet scheme. Coulombic long-range interactions were calculated using Ewald summation[93,94] and a potential cutoff was set at $R = 8.5\mathring{A}$. The simulations were carried out for 50 ps with the first 10 ps used for equilibration.

The initial input structures for the simulation were provided by Ripmeester and correspond to the experimental Type II clathrate hydrates.[95] Diffraction experiments were used to determine the position of the oxygen atoms, and the positions of the water hydrogen atoms were chosen so as to minimize the dipole moment of the Type II unit cell, in keeping consistent with the Bernal-Fowler ice rules, and were obtained from simulations done by van Klaveren *et al.*[96,97,98]

The unit cell volume and energy were determined with N-P-T simulations at 1.013 bars and 100 K for different guest hydrogen occupancies. In keeping consistent with Ripmeester's notation, the occupancy of the small and large cages in the unit cell is given with the notation *is+jl*, where i and j are the numbers of guest molecules in the small and large cages, respectively. Here, i=0,1,2 and j=0,1,2,3,4 are considered where all small (and large) cages in the super cell carry the same number of hydrogens. The empty cell is not stable experimentally, but on the order of the simulation time scale, it is metastable.

3.5.2 Results and discussion

The unit cell volume and energy content for various H_2 occupancies are shown in Figure 3.15 and Figure 3.16. The unit cell volume remains fairly constant up to $1s{+}2l$ and then repulsions among guest molecules and host-guest cause the large cell to expand, which is most clearly exhibited in the large jump in volume for the $2s{+}2l$ structure. The $1s{+}4l$ and $2s{+}2l$ cages are especially informative since they have the same number of guest hydrogens, but they are distributed differently. The unit cell volume greatly expands in going from the singly occupied small cage to the doubly occupied cage, and continues to increase as more hydrogen guests are added to the large cage. Although simulations detailing the variation of the lattice vector lengths for the Type II clathrate with the occupation number for hydrogen guest molecules have not completed at the time of this writing, Ripmeester's simulations demonstrate that as the occupancy increases to $2s{+}2l$, the structure undergoes a tetragonal distortion. This distortion has not been experimentally observed, and as suggest by Ripmeester *et al.*, this conclusion is based on the specific model potential chosen for the simulation. The COS_{hyd} potential model is more in agreement with high level *ab initio* quantum calculations, making simulations with this potential especially appealing.

The energy for loading the Type II hydrogen structure is given by Equation 3.21, where the isolated rigid-rotor H_2 is assigned an energy of 5RT/2 per mole (for an ideal diatomic gas).[99]

$E(nH_2)$ and $E(0H_2)$ are the potential energies of the unit cell with n H_2 guests (nH_2) and zero guests ($0H_2$). The results are detailed in Table 3.1. The $1s{+}4l$ structure is the most energetically favorable structure as it has the lowest energy. In considering the $2s{+}2l$ and $1s{+}4l$ structures, it is clear that double occupancy of the small cage increases the energy by $\sim$150 kJ/mol. Generally, placing a second hydrogen molecule in the small cage gives rise to a strong repulsion, which is reflected in the rise in potential energy. Additionally, an increase in the unit cell potential energy is seen in going from $2s{+}3l$ to $2s{+}4l$ with Ripmeester's force field, although no such increase is seen with the COS_{hyd} force field. The results of these simulations for potential energy and for unit cell volume follow can be seen in Figures 3.15

and 3.16 for both force fields.

$$\Delta E = E(nH_2) - E(0H_2) - \frac{5nRT}{2} \tag{3.21}$$

The radial distribution functions (O(water)-$H_{2\ M-site}$) in Figure 3.17 demonstrate that the distance between the guest hydrogen and water in the small cage is approximately 3.7 Å and the distance between the guest hydrogen and water in the large cage is about 4.0 Å, in agreement with experimental data.[100,48]

The O(water)-$H_{2\ M-site}$ radial distrubution functions for multiply occupied cages are shown in Figure 3.18, for simulations done with both the Ripmeester and COS_{hyd} potential. With both potentials, the $1s{+}nl$ system ($n = 0 - 4$), the peaks broaden and shifts from 3.7 Å for $1s{+}0l$ to 3.2 Å for $1s{+}4l$ as more hydrogen molecules are added. When the small cage is doubly occupied, the peak remains around 3.0 Å as hydrogen molecules are added to the large cage providing evidence that the RDF is dominated by the guest molecules in the small cage.

The $H_{2\ M-site}$-$H_{2\ M-site}$ RDFs are shown in Figure 3.19 for simulations using both the Ripmeester and COS_{hyd} potential. In both cases, the $1s{+}nl$ ($n = 2 - 4$), the peak is at a distance of 3.0 Å, and for the $2s{+}nl$ ($n = 2 - 4$), the average separation is at about 2.7 Å. Additionally, the peak generated from the COS_{hyd} potential begins to split as a third hydrogen molecule is added to the large cage, corresponding to the separation between the H_2 guest molecules in the small and large cages. This split becomes more pronounced when a fourth hydrogen molecule is added, although it is not seen in the RDFs generated by simulations with the Ripmeester potential. It is likely that the COS_{hyd} force field is able to predict a geometrical arrangement of the H_2 molecules that causes this split, and lowers the potential energy of the unit cell, as discussed above.

To recap, simulations with COS/G2 model for H_2O and COS_{hyd} for H_2 suggest that single occupancy in the small cages is preferable since double occupancy raises the energy and likely causes tetragonal distortion of the unit cell. In terms of storage potential, $2s{+}4l$ hydrogen storage capacity is 5.0 wt %, and decreases to about 3.8 wt % for the singly occupied small

Table 3.1: The energy, ΔE_n, (kcal/mol) required to load the clathrate with n guest hydrogen molecules at 100 K and 1.013 bars.

n[a]	ΔE_n	$\Delta E_n/n$
8 (0s+1l)	-78.6	52.5
16 (1s+0l)	-183.5	19.3
24 (1s+1l)	-261.5	9.7
32 (1s+2l)	-309.6	6.0
40 (1s+3l)	-365.6	3.7
48 (1s+4l)	-390.3	2.5
48 (2s+2l)	-237.6	6.1
56 (2s+3l)	-292.6	4.5
64 (2s+4l)	-330.1	4.2

[a]The notation is+jl corresponds to the numbers of guest molecules (i and j) in the small (s) and large (l) cage

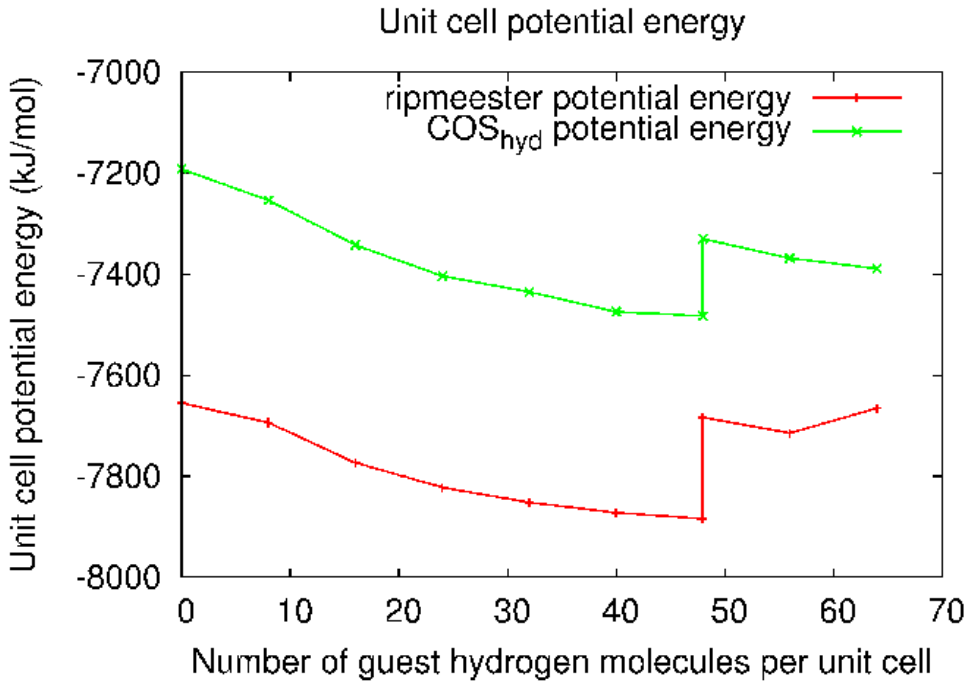

Figure 3.15: The energy per unit cell for different hydrogen cell occupancy numbers in the Type II clathrate at 1.013 kbars and 100 K with the Ripmeester and COS$_{hyd}$ potential.

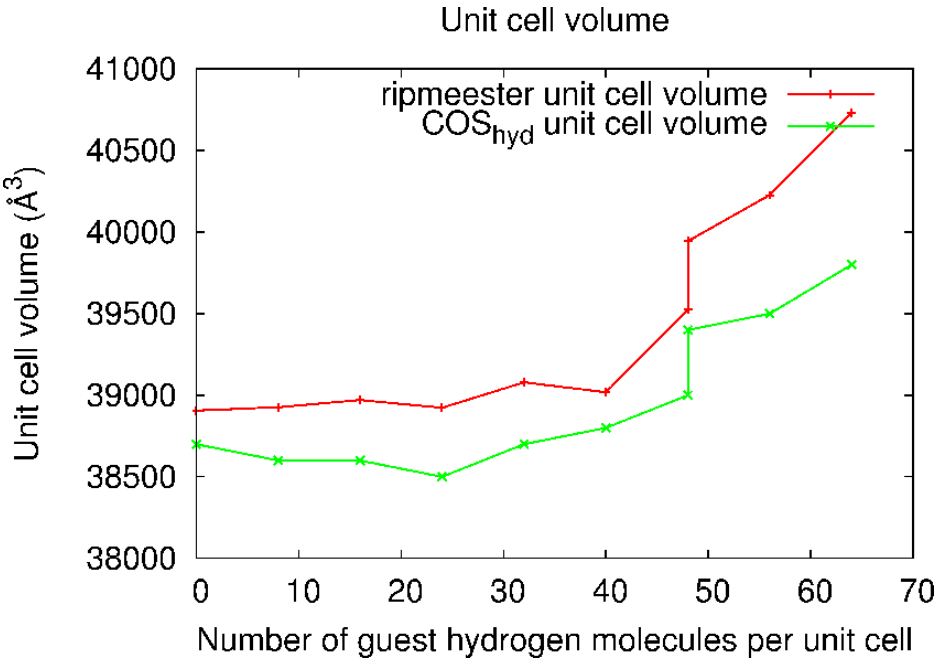

Figure 3.16: The unit cell volume ($\mathring{A}$ ^{3}) for different hydrogen cell occupancy numbers in the Type II clathrate at 1.013 kbars and 100 K with the Ripmeester and COS$_{hyd}$ potential.

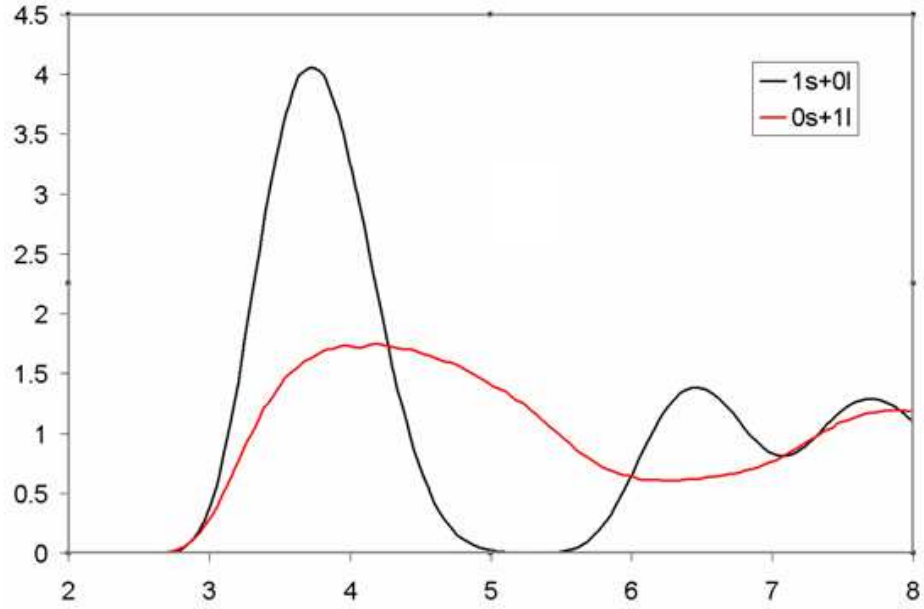

Figure 3.17: The O(water)-H_2 $_{M-site}$ radial distribution function for the $1s$+$0l$ and $0s$+$1l$ structures at 100 K and 1.013 bar. The peak in the $1s$+$0l$ cage is at approximately 3.7 $\mathring{A}$, and is located approximately at 4.1 $\mathring{A}$ for the $0s$+$1l$ cage.

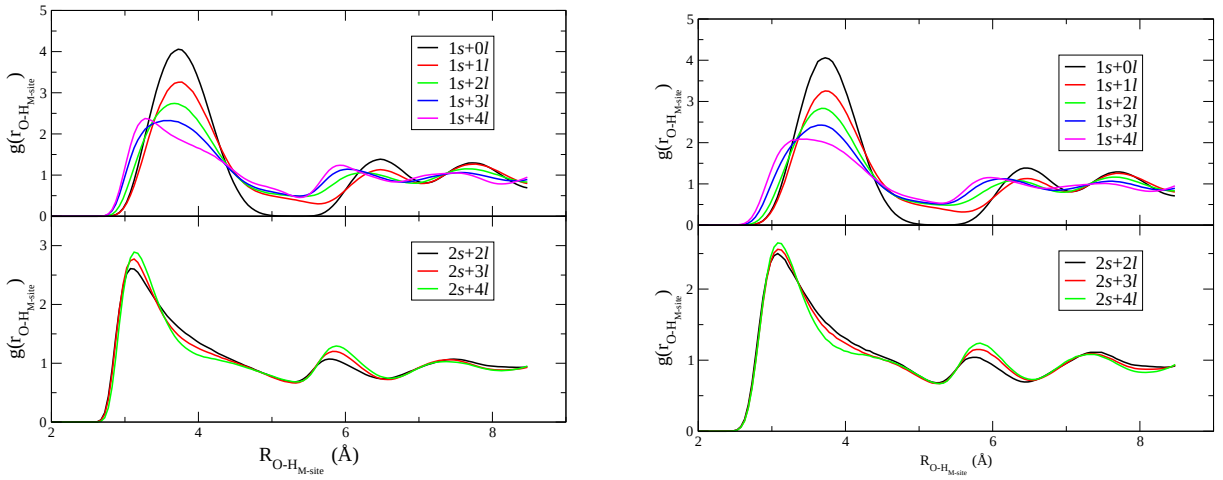

(a) (b)

Figure 3.18: The O(water)-H_2 $_{M-site}$ radial distribution function for the different hydrogen guest occupancy numbers at 100 K and 1.013 bar for simulations done with ripmeester's potential (a) and COS_{hyd} potential (b). The RDF curves broaden as more hydrogens are added to the large cage, while the small cage remains singly occupied. The RDF curves are not greatly affected by multiple occupancies in the large cage when the small cage is doubly occupied.

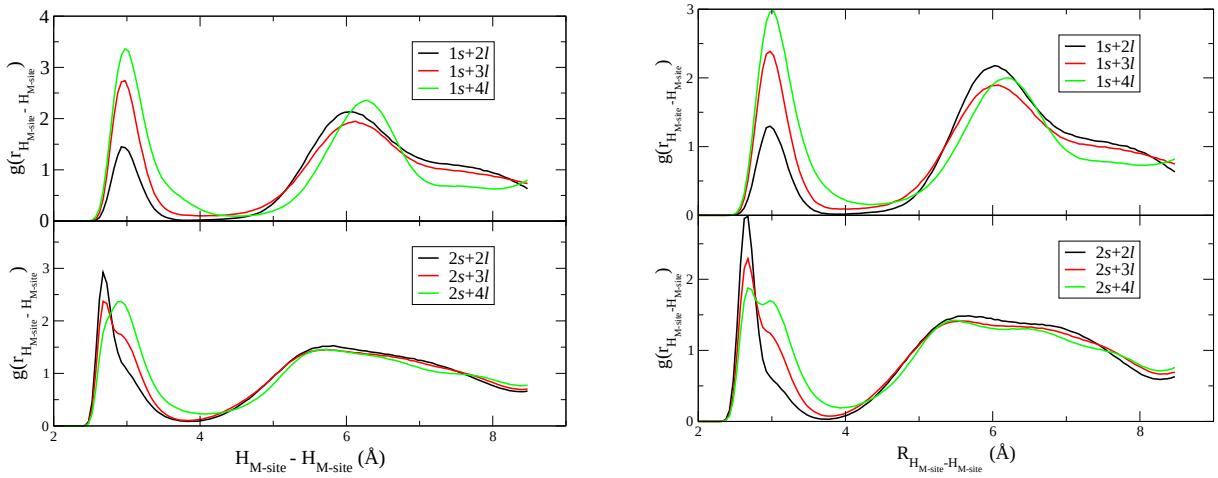

(a) (b)

Figure 3.19: The H_2 $_{M-site}$-H_2 $_{M-site}$ radial distribution function for the different hydrogen guest occupancy numbers at 100 K and 1.013 bar for simulations done with ripmeester's potential (a) and COS_{hyd} potential (b). The RDF curves remain fairly unchanged for the singly occupied small cage as more hydrogen molecules are added to the large cage for simulations with both potentials. For the doubly occupied cage, a split in the peak for the $2s+3l$ and $2s+4l$ structures is seen with the COS_{hyd} potential, but this split is only seen in the $2s+3l$ structure with the Ripmeester potential.

cage structure. These factors, and the high pressure required for synthesis may limit the use of clathrates as an effective storage medium for hydrogen, but research dedicated to overriding these challenges is ongoing, and clathrates remain a promising option.

3.6 SUMMARY AND FUTURE DIRECTION

It has been previously demonstrated that in order to accurately describe properties of hydrogen bonded systems, such as clathrates, it is necessary to use a model for H_2O that explicitly includes polarization. In particular, this was shown to be crucial in predicting properties such as the temperature dependence of lattice constants and vibrational spectra, as well as reproducing experimental data. These reasons provided motivation for developing a polarizable force field for hydrogen clathrate simulations, and the majority of the work presented here was dedicated to this endeavor. The resulting COS_{hyd} model closely predicts the potential energy surfaces generated by high-level *ab intio* calculations. The force field was tested in simulations of the clathrate system with varying occupancies of hydrogen guests in the small and large cages, and the results are in agreement with experimental data.

It is expected that this working COS_{hyd} model can be used in future simulations to address issues related to hydrogen storage potential. In particular, simulations of the H_2 occupancy under different pressure and temperature regimes may provide experimental guidance in determining methods of economic synthesis. Further, there has been evidence that presence of a promoter molecule such as tetrahydrofuran reduces the formation pressure by a factor of 30.[101,102] In these systems, the large cage is filled by the THF, and the small cage is filled by H_2. The THF concentration and pressure range required for formation needs further investigation. Also, the occupancy number of the small cage in this system is not entirely clear, illustrating the need for more work.

3.7 ACKNOWLEDGEMENT

We acknowledge support from the National Science Foundation (Grant CHE-040474).

4.0 STRUCTURE AND STABILITY OF THE $(H_2O)_{21}$ AND $(H_2O)_{20}\cdot H_2S$ CLUSTERS: RELEVANCE OF CLUSTER SYSTEMS TO GAS HYDRATE FORMATION

This work was published as: Valerie N. McCarthy, Kenneth D. Jordan. *Chemical Physics Letters* 429 (2006) 166-168

4.1 ABSTRACT

In order to gain insight into the factors responsible for the different behavior of H_2O and H_2S with respect to hydrate formation, we have studied theoretically the $(H_2O)_{21}$ and $(H_2O)_{20}\cdot H_2S$ cluster systems. For each cluster, two isomers resulting from insertion of an H_2O or H_2S molecule into a dodecahedral $(H_2O)_{20}$ cage were examined. The calculations were performed using the density functional and RIMP2 methods.

4.2 INTRODUCTION

H_2S is known to form a type I gas hydrate,[50] in which the H_2S molecules are encapsulated in dodecahedral and tetrakaidecahedron water cages.[103] In contrast, water does not form a crystalline "self" hydrate, with water molecules trapped inside polyhedral cages. To gain insight into the factors responsible for the different behavior of H_2O and H_2S with respect to hydrate formation, we have employed the density functional[8,104] and RIMP2[10,9] electronic structure methods to examine the stability of the $(H_2O)_{21}$ and $(H_2O)_{20}{\cdot}H_2S$ cluster systems.

In each case two isomers with the guest H_2S (or H_2O) molecule inserted inside the most stable dodecahedral cage were considered. In one isomer, the guest molecule donates two H-bonds to the O atoms of the cage, with the cage retaining ten free OH groups, and in the other isomer, two of the free OH groups of the cage are reoriented inward so that the guest molecule is engaged in a total of four H-bonds (two donor and two acceptor).

4.3 METHODOLOGY

The starting point for the various calculations was the undistorted dodecahedral $(H_2O)_{20}$ cage, hereafter designated as UD. There are multiple such structures differing in the arrangement of the H-bonds.[105] In this work we start from the lowest energy isomer of $(H_2O)_{20}$ reported by Xantheas *et al.*[105] The additional H_2O or H_2S molecule was then added to the interior of the cluster, either retaining the ten free OH groups of the cage, giving the so called $(20,1)_{10}$ species or with two of the free OH groups reoriented inward to give the $(20,1)_8$ isomer (the structures of the isomers are depicted in Figure 4.1). The specific $(20,1)_8$ isomer considered for $(H_2O)_{21}$ is that located by our group.[106] This isomer lies 0.6 kcal/mol above another $(20,1)_8$ isomer reported by Hartke *et al.*[107] and which was located using the basin hopping algorithm together with the polarizable TTMF-2 model potential.[108] For the $(H_2O)_{20}{\cdot}H_2S$ species the internal water molecule of the two $(H_2O)_{21}$ isomers was replaced by

H_2S to obtain the initial structures for the geometry optimizations.

All structures were optimized using the Becke3LYP[8,104] density functional method together with the augmented correlation-consistent polarized valence double-zeta (aug-cc-pVDZ) basis set.[109,110,111] Single-point energy calculations were performed using the resolution-of-the-identity second-order Moller-Plesset perturbation theory (RIMP2)[10,9] with both the aug-cc-pVDZ and aug-cc-pVTZ basis sets and using the Becke3LYP/aug-cc-pVDZ optimized geometries. The counterpoise correction for basis set superposition error[7] was applied to the RIMP2 results. The harmonic vibrational frequencies were calculated at the B3LYP/6-31+G(d) level of theory and used to estimate vibrational zero-point energy corrections to the relative stabilities.

4.4 RESULTS AND DISCUSSION

Figure 4.1 depicts the structures of the undistorted water dodecahedron as well as of the $(20,1)_{10}$ and $(20,1)_8$ isomers of $(H_2O)_{21}$ and $(H_2O)_{20}{\cdot}H_2S$. It is clear from this figure that the cages of the $(20,1)_8$ isomers are highly distorted compared to that of the UD and $(20,1)_{10}$ species. The $(20,1)_8$ isomer of $(H_2O)_{21}$ is one of a family of closely related structures, which in turn are similar to the low-lying minima of the $H^+(H_2O)_{21}$ cluster which associate the excess proton with a water monomer on the cluster surface.[112]

Tables 4.1 and 4.2 report the energies of the $(20,1)_{10}$ and $(20,1)_8$ isomers of $(H_2O)_{21}$ and $(H_2O)_{20}{\cdot}H_2S$ relative to those of the undistorted dodecahedron plus a free H_2S or H_2O molecule, with and without corrections for the vibrational zero-point energies. From the data in these tables, it is evident that the clusters with the internal H_2O or H_2S molecule are significantly ($\sim$5 to 10 kcal/mol) more stable with the RIMP2 method than with the Becke3LYP method. This could reflect, in part, the importance of dispersion interactions in the binding of the interior monomer. In the subsequent discussion we focus on the RIMP2/aug-cc-pVTZ results with the counterpoise (CP) correction as these should be the most reliable results for

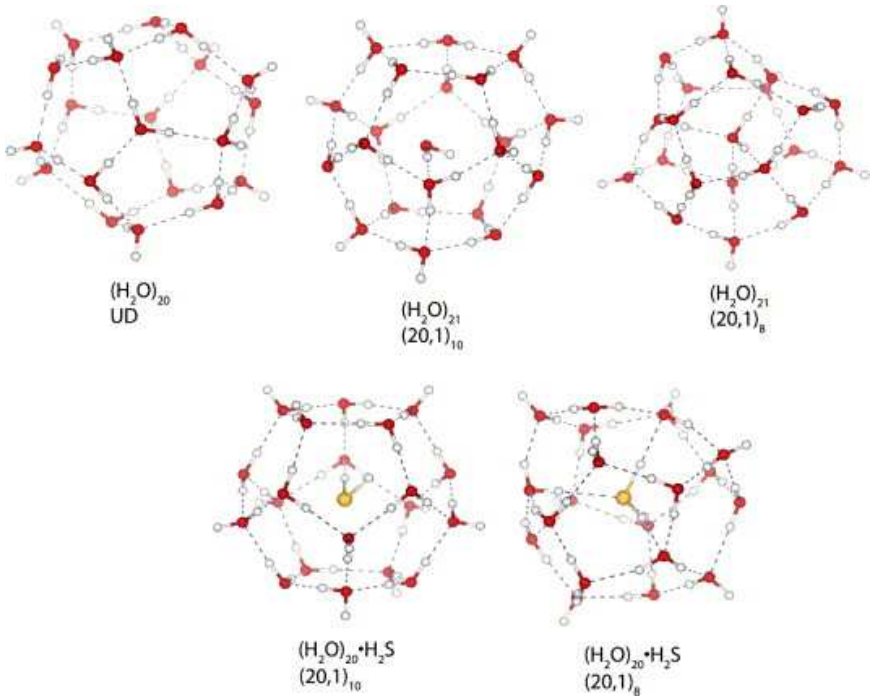

Figure 4.1: Structures of the UD $(20,1)_{10}$ and $(20,1)_8$ isomers of $(H_2O)_{20}$, $(H_2O)_{21}$ and $(H_2O)_{20}{\cdot}H_2S$

Table 4.1: Relative energies (kcal/mol) for isomers of $(H_2O)_{21}$

Method[a]	UD+H_2O	$(20,1)_8$	$(20,1)_{10}$
B3LYP/aug-cc-pVDZ	0.0	-16.6	-3.5
B3LYP/aug-cc-pVTZ	0.0	-14	-1.7
RIMP2/aug-cc-pVDZ	0.0 (0.0)	-26.0 (-19.3)	-10.0 (-5.7)
RIMP2/aug-cc-pVTZ	0.0 (0.0)	-23.0 (-19.3)	-8.0 (-6.1)
HF/aug-cc-pVTZ	0.0 (0.0)	-9.4 (-8.9)	-2.1 (-1.7)
Relative ZPE	0	4.9	0.8

[a]The numbers in paranthesis denote relative energies including counterpoise corrections.

predicting relative stabilities.

4.4.1 $(H_2O)_{21}$

At the RIMP2-CP/aug-cc-pVTZ level, the $(20,1)_{10}$ and $(20,1)_8$ isomers of $(H_2O)_{21}$ are calculated to be, respectively, 6.1 and 19.3 kcal/mol more stable than the undistorted water dodecahedron [$(UD(20)_{10}$] plus a free water molecule. In the $(20,1)_{10}$ isomer of $(H_2O)_{21}$, the internal water molecule forms only a single H-bond with one of the water molecules of the cage, and the cage is only slightly distorted by the presence of the internal water molecule. In contrast, the cage of the $(20,1)_8$ isomer of $(H_2O)_{21}$ is highly distorted from that of the undistorted $(H_2O)_{20}$ dodecahedron, primarily due to the reorientation of the two OH-bonds with the internal water molecule. The large distortion energy (22.1 kcal/mol) is more than compensated by the 31.0 kcal/mol attractive interaction between the guest water molecule and the distorted cage. Inclusion of the vibrational zero-point corrections destabilizes the $(20,1)_8$ and $(20,1)_{10}$ isomers relative to UD+H_2O by 4.9 and 0.8 kcal/mol, respectively. Even with the vibrational ZPE corrections, the $(20,1)_8$ isomer of $(H_2O)_{21}$ is calculated to be 9.1

Table 4.2: Relative energies (kcal/mol) for isomers of $(H_2S)_{21}$

Method[a]	UD+H_2S	$(20,1)_8$	$(20,1)_{10}$
B3LYP/aug-cc-pVDZ	0.0	1.1	0.8
B3LYP/aug-cc-pVTZ	0.0	3.6	2.4
RIMP2/aug-cc-pVDZ	0.0 (0.0)	-12.9 (-5.0)	-12.5 (-6.3)
RIMP2/aug-cc-pVTZ	0.0 (0.0)	-9.8 (-6.2)	-10.1 (-7.4)
HF/aug-cc-pVTZ	0.0 (0.0)	4.8 (5.3)	1.2 (1.6)
Relative ZPE	0	2.5	1.2

[a]The numbers in paranthesis denote relative energies including counterpoise corrections.

kcal/mol more stable than the $(20,1)_{10}$ isomer.

4.4.2 $(H_2O)_{20}\cdot H_2S$

The $(20,1)_{10}$ and $(20,1)_8$ isomers of the $(H_2O)_{20}\cdot H_2S$ cluster are calculated to be, respectively, 7.4 and 6.2 kcal/mol more stable than the perfect dodecahedron plus a free H_2S molecule at the RIMP2-CP/aug-cc-pVTZ level of theory. As in $(H_2O)_{21}$, the dodecahedral cage of the $(20,1)_{10}$ isomer of $(H_2O)_{20}\cdot H_2S$ is only slightly distorted due to the presence of the guest molecule, whereas the $(20,1)_8$ isomer of $(H_2O)_{20}\cdot H_2S$ is highly distorted by the guest molecule. In the $(20,1)_8$ isomer of $(H_2O)_{20}\cdot H_2S$, the H2S monomer makes two very weak (as judged by the bond lengths) H-bonds to the water molecules of the cage.

In contrast to $(H_2O)_{21}$ for which there is a strong preference for the isomer forming four H-bonds to the internal monomer, for $(H_2O)_{20}\cdot H_2S$ there is a slight ($\sim$1.2 kcal/mol) preference for the $(20,1)_8$ isomer. This is a consequence of the much weaker donor and acceptor H-bonds between H_2S and H_2O molecules than between two H_2O molecules. Vibrational ZPE destabilizes the $(20,1)_8$ and $(20,1)_{10}$ isomers of $(H_2O)_{20}\cdot H_2S$ by 2.5 and 1.2 kcal/mol,

respectively, with respect to the undistorted dodecahedron plus a free H_2S molecule. With inclusion of vibrational ZPE corrections the $(20,1)_{10}$ isomer is predicted to be 2.5 kcal/mol more stable than the $DD(20,1)_8$ isomer.

4.5 CONCLUSION

The greater stability of the $(20,1)_{10}$ isomer of $(H_2O)_{20}{\cdot}H_2S$ over the $(20,1)_8$ isomer is consistent with the ability of H_2S to form a clathrate with H_2O. Moreover, the strong preference of $(H_2O)_{21}$ for the $(20,1)_8$ isomer over the $(20,1)_{10}$ isomer is consistent with the failure of H_2O to form a "self" clathrate. Here it should be noted that the $(20,1)_8$ isomer arrangement cannot be accommodated into a periodic crystalline structure.

Although the focus here has been on H_2O clusters with H_2O or H_2S molecules inside $(H_2O)_{20}$ cages, it is instructive to compare these results with those for a methane molecule inside a dodecahedral cage. To this end, we have also carried out RIMP2 calculations of a methane molecule inside the $(H_2O)_{20}$ dodecahedral cage. In this case the counterpoise corrected RIMP2/aug-cc-pVDZ calculations indicate that the system is bound by 3.4 kcal/mol, with respect to the undistorted dodecahedron plus a free methane molecule. This interaction of the CH_4 molecule with the dodecahedral cage is appreciably weaker than that found for H_2O and H_2S with the cage.

4.6 ACKNOWLEDGEMENTS

We acknowledge support from the National Science Foundation (Grant CHE-040474).

5.0 DIRECT MEASUREMENT OF THE ENERGY THRESHOLDS TO CONFORMATIONAL ISOMERIZATION IN TRYPTAMINE: EXPERIMENT AND THEORY

This work was published as: J. R. Clarkson, B. C. Dian, L. Morigg, A. DeFusco, V. McCarthy, K. D. Jordan, and T. S. Zwier. *J. Chem Phys.* (122) (2005) 214311.

The author wishes to acknowledge that the work in the experimental sections of the paper was performed by JRC, BCD, and LM. Theoretical calculations were carried out by VNM with assistance from AD.

5.1 ABSTRACT

The methods of stimulated emission pumping-hole filling spectroscopy (SEP-HFS) and stimulated emission pumping population transfer spectroscopy (SEP-PTS) were applied to the conformation-specific study of conformational isomerization in tryptamine [TRA, 3 - (2-aminoethyl)indole]. These experimental methods employ stimulated emission pumping to selectively excite a fraction of the population of a single conformation of TRA to well-defined ground-state vibrational levels. This produces single conformations with well-defined internal energy, tunable over a range of energies from near the zero-point level to well above the lowest barriers to conformational isomerization. When the SEP step overcomes a barrier to isomerization, a fraction of the excited population isomerizes to form that product. By

carrying out SEP excitation early in a supersonic expansion, these product molecules are subsequently cooled to their zero-point vibrational levels, where they can be detected downstream with a third tunable laser that probes the ground-state population of a particular product conformer via a unique ultraviolet transition using laser-induced fluorescence. The population transfer spectra (recorded by tuning the SEP dump laser while holding the pump and probe lasers fixed) exhibit sharp onsets that directly determine the energy thresholds for conformational isomerization in a given reactant-product conformer pair. In the absence of tunneling effects, the first observed transition in a given X-Y PTS constitutes an upper bound to the energy barrier to conformational isomerization, while the last transition not observed constitutes a lower bound. The bounds for isomerizing conformer A of tryptamine to B(688-748 cm^{-1}), C(1)(860-1000 cm^{-1}), C(2)(1219-1316 cm^{-1}), D(1219-1282 cm^{-1}), E(1219-1316 cm^{-1}), and F(688-748 cm^{-1}) are determined. In addition, thresholds for isomerizing from B to A(< 1562 cm^{-1}), B to F(562-688 cm^{-1}), and out of C(2) to B(< 747 cm^{-1}) are also determined. The $A \rightarrow B$ and $B \rightarrow A$ transitions are used to place bounds on the relative energies of minima B relative to A, with B lying at least 126 cm^{-1} above A. The corresponding barriers have been computed using both density functional and second-order many-body perturbation theory methods in order to establish the level of theory needed to reproduce experimental results. While most of the computed barriers match experiment well, the barriers for the A-F and B-F transitions are too high by almost a factor of 2. Possible reasons for this discrepancy are discussed.

5.2 INTRODUCTION

Molecules with several torsional degrees of freedom undergo conformational isomerization on highly corrugated, multidimensional potential-energy surfaces containing many minima and an even greater number of transition states separating them. When there are local minima close in energy to the global minimum, they can acquire significant population, even when the molecule is cooled in a supersonic expansion. Building off a foundation of conformation-specific infrared and ultraviolet spectroscopies,[113,114,115,116,117,118,119,120,121,122] we have recently been studying the conformational isomerization dynamics of such molecules using a new experimental protocol developed expressly for this purpose.[123,124,125,14] As shown schematically in Figure 5.1, this protocol involves (i) initial cooling of the molecules of interest to their zero-point levels, (ii) selective laser excitation of a single "reactant" conformation in the mixture while the molecules are still in a high-density region of the expansion where collisions are prevalent, (iii) isomerization and recooling of the molecules, followed by (iv) selective detection of a single "product" conformation downstream in the collision-free region of the expansion with a probe laser.

The initial studies that used this cool-excite-cool-probe scheme employed infrared excitation of a single conformation via the amide NH stretch fundamentals to initiate conformational excitation.[123,124,125,14] Conformation-selective excitation and detection steps provide a means of dissecting the complex set of isomerization processes into individual $X \rightarrow Y$ reactant-product pairs. When the infrared laser is fixed and the probe laser tuned, one can determine which products are formed. This scheme is called IR-UV hole-filling spectroscopy because the "hole" created in the ground-state population of the excited conformer is used to fill in population in product conformers. On the other hand, when the IR laser is tuned while the UV probe laser is fixed to monitor a given product conformer population, the resulting spectrum [called an IR-induced population transfer spectrum (IR-PTS)] records the fractional population change induced by the infrared laser. By piecing together the results of a series of IR-population transfer spectra, it is possible to determine the isomerization

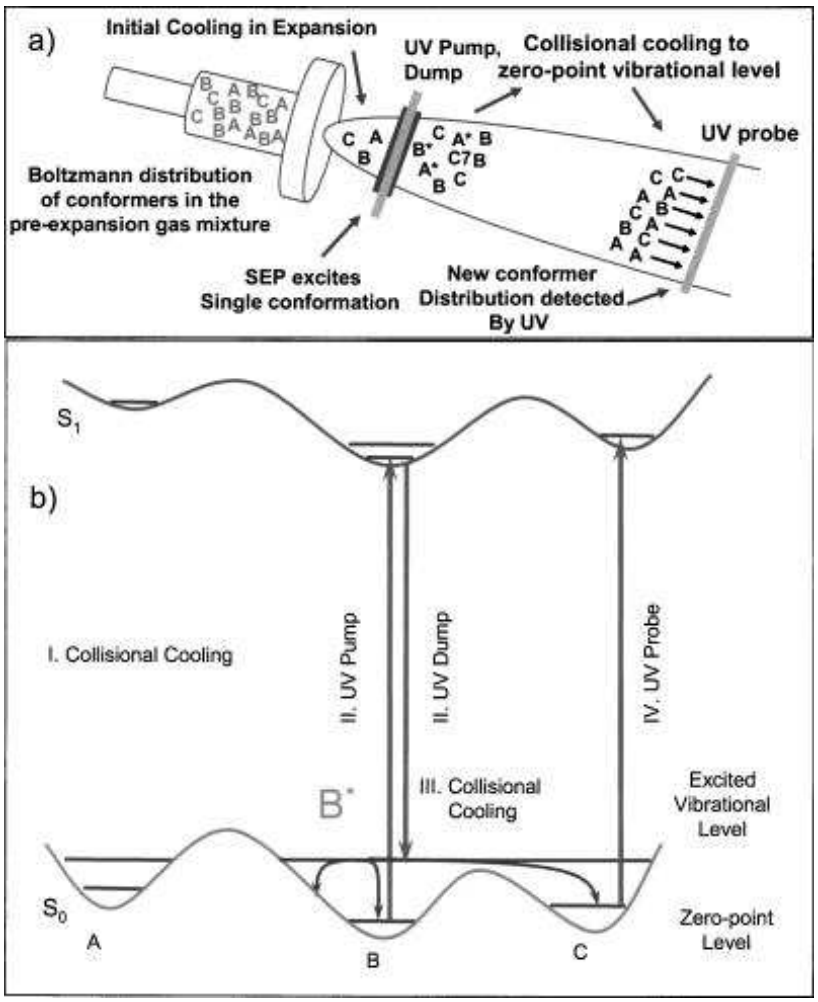

Figure 5.1: (a) Schematic diagram of the spatial temporal arrangement of the experiment. Selective stimulated emission pumping (SEP) excitation of a single conformation is carried out early in the supersonic expansion, followed by collisional recooling either back into the original minimum or into other minima following isomerization. The changes in conformational population are detected downstream using laser-induced fluorescence (LIF). In SEP hole-filling (SEP-HF) spectroscopy, the first (pump 20 Hz) laser and second (dump 10 Hz) UV lasers are held fixed while the third UV laser (probe 20 Hz) is scanned. In the SEP-population transfer (SEP-PT), the dump laser is tuned while the probe laser is fixed at a unique vibronic transition. In either case, the difference in fluoresence signal with and without the dump laser is detected downstream.

product quantum yields following conformation-selective infrared excitation.

One of the nonideal aspects of the infrared excitation scheme is that absorption of one infrared photon in the hydride stretch fundamental region (˜3500 cm^{-1}) puts 10 kcal/mol of energy into the excited conformation, well above many of the lowest-energy barriers to conformational isomerization (3-5 kcal/mol typical).[124] Recently, we reported first results of a variation of the hole-filling method that employs simulated emission pumping (SEP) rather than infrared excitation.[14] SEP is a powerful spectroscopic technique which has been utilized in a number of ways.[126,127,128] With SEP, it is possible to tune widely over ground-state vibrational energies ranging from the vibrational zero-point level to well above the lowest-energy barriers to isomerization. In doing so, it is possible to directly measure the energy thresholds to isomerization for individual $X \rightarrow Y$ reactant-product pairs. Thus, the SEP-PT spectra provide a spectroscopic means of placing bounds on the barrier heights to conformational isomerization. This is an exciting prospect because spectroscopy almost always characterizes the minima on the potential-energy surface rather than the barriers.

The SEP hole-filling scheme was carried out first on tryptamine [TRA, 3- (2 - aminoethyl) indole]. In the initial report, we demonstrated the ability of the method to measure the barriers to conformational isomerization, even in a case where there are several isomers present.[14] In this respect, TRA is quite a challenge because it possesses seven conformational isomers with significant population, even under conditions of supersonic expansion cooling.[129,11,130,13,131] As a result, there are 42 individual $X \rightarrow Y$ reactant-product pairs. Of course, the $X \rightarrow Y$ and $Y \rightarrow X$ pairs measure the same barrier from either direction. The difference in these energy thresholds then constitutes a measure of the energy differences between the minima; that is,

$$E_{thresh}(X \rightarrow Y) - E_{thresh}(Y \rightarrow X) = E_{min}(Y) - E_{min}X \tag{5.1}$$

Thus, the combined results from all 42 $X \rightarrow Y$ pairs could in principle constitute a complete characterization of the energies of the relevant stationary points on the potential-energy surface for isomerization.

In the present paper, we provide a complete account of the SEP hole-filling studies of tryptamine. In addition to a more detailed exposition of the full experimental data set, we have now carried out an extensive set of *ab initio* and density-functional theoretical (DFT) calculations of the transition states for conformational isomerization in TRA, for comparison with the experimental data. As we shall see, the experimental data match well with calculations for most of the reactant-product pairs measured. However, the thresholds into conformer well F are computed to be about a factor of 2 higher than the experiment. The effect of tunneling on the measured isomerization thresholds has been explored by using tryptamine deuterated at the amino site.

The study of TRA presented here is followed up in an adjoining paper by an analogous study of conformational isomerization in 3-indole propionic acid (IPA) and its water-containing complexes.[132]

5.3 METHODS

5.3.1 Experiment

The laser-induced fluorescence (LIF) chamber used in these experiments has been described in detail elsewhere.[123] Those aspects of the experiment that are unique to the SEP hole-filling method are described here. The three UV laser beams enter the chamber through CaF_2 windows mounted at the Brewster's angle before passing through a set of baffles containing 2×10 mm slits to allow easy spatial movement of the laser beams intersecting the supersonic expansion. The laser beams intersect the supersonic expansion at right angles while the fluorescence is collected by a filtered photomultiplier tube (PMT) (ETI 9318QB with WG320 and WG305 cut-off filters) perpendicular to both the jet and the excitation beam. TRA (Aldrich) was resistively heated to 400 K in a stainless-steel sample holder. The sample was entrained in helium (commercial grade, 99.995 %) at a total pressure of 7 bars and expanded through a 20-Hz pulsed valve (Parker General, Series 9, 2-mm orifice)

into a vacuum chamber pumped with a roots blower (Leybold, WS-1001) backed by two rotary vane mechanical pumps (Sargent-Welch) to supersonically cool the molecules into their conformational-specific zero-point levels. Total flow rates of 2×10^{-3} bar L/s in a 1.0-1.5-ms gas pulse were used, leading to a vacuum chamber pressure of ˜5×10^{-5} bar.

Three independent Nd:YAG-(yttrium aluminum garnet) pumped (Continuum 7000 series and NY-61) doubled dye lasers (Lumonics HD-500, Lambda Physik Scanmate 2E and FL3002) were employed. Foundational to all methods was laser-induced fluorescence excitation spectroscopy, in which a single ultraviolet laser (˜0.1 mJ/pulse) was tuned through the $S_1 \leftarrow S_0$ origin region of jet-cooled tryptamine. LIF spectroscopy was carried out at a distance (x) 12 mm downstream from the 2-mm-diameter expansion orifice (D) (corresponding to $x/D = 6$). SEP spectra were recorded at this same spatial position, with the pump laser λ_1 fixed on the $S_1 \leftarrow S_0$ origin band of a specific conformer. In the dump step, the excited-state population was transferred to a particular vibrational level in the ground state [$S_0(v)$] via stimulated emission induced by a second tunable laser (the "dump" laser). Under optimal conditions, as much as 30%-40% of the population in the S_1 state of a particular conformation of TRA can be driven back to $S_0(v)$. The magnitude of this population transfer depends on (i) the laser powers in both pump and dump steps, (ii) the lifetime of the S_1 state, (iii) the delay between pump and dump lasers, (iv) the oscillator strength and Franck-Condon factors for the dump transitions, and (v) the rate of collisional removal from the lower level.

The SEP spectra were recorded using the active baseline subtraction mode of a gated integrator (SRS 250). The dump laser (10 Hz) was pulsed every other time the pump laser (20 Hz) fires. A negative signal indicates that the dump laser has depleted the fluorescence signal. Typical pulse energies for the pump and dump steps were 0.1-0.2 and 0.5-1.0 mJ, respectively. Focusing conditions were chosen to ensure that the dump laser beam was larger than the pump laser, with the pump and dump lasers focused with 50- and 70-cm focal length lenses, respectively.

In order to detect the SEP dump transition, the two lasers were delayed somewhere

in the range of 2-10 ns, determined by a compromise between maximizing the dip in the fluorescence signal and minimizing the interference from scattered light from the dump laser. The gated signal was delayed as far from the scattered light as possible while collecting sufficient fluorescence to detect the depletion in fluorescence signal created by the dump laser.

The triple-resonance methods presented here share the pump-dump-probe excitation scheme with the studies of Kable and Knight[133] and Burgi *et al.*[134,135] The unique aspect of the present work is the place of SEP excitation, sufficiently downstream so that SEP excitation could be cleanly carried out from the vibrational zero-point levels of the conformational isomers, but in a collisional regime where sufficient collisional cooling occurred subsequent to the SEP step to recollect the population into the zero-point levels of the various conformers prior to probing downstream. The lasers used for SEP excitation typically intersected the expansion at $x/D = 2 - 2.5$, while the probe laser was set to $x/D = 6$, producing a delay between pump/dump and probe of 1.8-2.0 μs for optimal signal, determined by the terminal velocity of a helium expansion (1.8×10^5 cm/s). We estimate a collision rate for tryptamine with helium at 4×10^9 s^{-1} at the SEP excitation point in the expansion under typical expansion conditions, falling off as (x/D).[114]

Two schemes, differing in terms of which lasers were tuned and which were fixed in wavelength, were employed for the infrared excitation.[123] In SEP-population transfer spectroscopy, the pump and probe lasers were fixed on the $S_1 \leftarrow S_0$ origin transitions of two conformational isomers (e.g., A and B, respectively), while the dump laser was tuned. As its name implies, population transfer (PT) spectroscopy monitors the amount of population transferred from A to B as a function of the internal energy placed in A by the dump laser:

$$A^*(E_{int}) \rightarrow B. \tag{5.2}$$

In order to selectively highlight the population transfer due to the dump laser, the pump and probe lasers operated at 20 Hz, while the dump laser operated at 10 Hz. The difference in signal between successive probe pulses was recorded using active baseline subtraction. By

recording the LIF signal size due to conformer B before and after the PT spectrum, the ordinate can be recorded as a fractional change in the population of the product B induced by the dump laser.

A second variation, SEP hole-filling spectroscopy (HFS), has both the pump and dump wavelengths fixed; thereby selectively exciting a particular conformational isomer to a ground-state vibrational level with well-defined internal energy. In HFS, the probe laser was scanned to determine where the population went, with gains in the probe signal occurring whenever transitions due to energetically open product channels were encountered.

Since PT and HF spectroscopies require careful spatial and temporal controls of three laser beams, two laser checks were developed to assist in setting up the experiment. The proper timing and spatial arrangement between pump and probe lasers could be set by pulling back the nozzle so that collisional refilling could not occur, and then maximizing the dip in the fluorescence signal from conformer A produced by the pump laser fixed on the same transition. Maximizing the SEP dip was used to maximize the spatial overlap between pump and dump. These two checks were typically sufficient to observe some signal in the three-laser experiment. Final optimization of the delay and spatial overlap between pump and dump was carried out on the three-laser signal under hole-filling conditions.

TRA deuterated at the NH_2 and indole NH sites [TRA(d_3)] was prepared in order to test for the effects of tunneling involving the NH_2 hydrogens on the measured energy thresholds for isomerization. Because TRA is relatively insoluble in pure D_2O, the sample was dissolved in excess tetrahydrofuran in the presence of D_2O. The exchange was allowed to occur for several hours before removal of the solvent with a rotary evaporator. The procedure was repeated three times to bring the sample to near-complete deuteration at the ND_2 site. The resulting purity and further experimental details concerning the deuterated sample will be presented in the Results section.

5.3.2 Calculations

The minimum-energy structures were optimized using the Becke3 LeeYangParr[104,8] (LYP) density-functional method with both the 6-31+G(d)[136] and augmented correlation consistent polarized valence double zeta[109,110,111] (aug-cc-pVDZ) basis sets. Transition state structures were then optimized at the Becke3LYP/6-31+G(d) level and employing the quadratic synchronous transit (QST3)[15] algorithm. These calculations were followed up with the resolution of the identity second-order Møeller-Plesset[10,9] (RIMP2)/aug-cc-pVDZ single-point calculations at the Becke3LYP/6-31+G(d) geometries. In addition, all local minima and a subset of the transition states were reoptimized at the RIMP2/aug-cc-pVDZ level. For selected minima and transition state structures, single-point RIMP2/augmented correlation consistent polarized valence triple zeta[109,110,111] (aug-cc-pVTZ) and second-order Møeller-Plesset (MP2)/aug-cc-pVDZ energies were calculated using RIMP2/aug-cc-pVDZ geometries, and in some cases, MP2/aug-cc-pVDZ geometry optimizations were performed as well. The results for these calculations are presented in their entirety in supplementary material and will be referred to throughout the text as necessary.[137]

The RIMP2 procedure uses a resolution of the identity operator approach to reduce the computational effort associated with MP2-level calculations. Several studies have shown that the errors introduced in relative energies due to the use of this approximation is generally 0.1 kcal/mol or less.[10] The main advantage of the MP2 and RIMP2 procedures over the computationally faster Becke3LYP method is the proper treatment of long-range dispersion interactions.[118] The Becke3LYP and MP2 calculations were carried out using the GAUSSIAN 03 program[138] and the RIMP2 calculations were carried out using the TURBOMOLE program.[139] All Becke3LYP calculations used the ultrafine grid and tight convergence criteria as implemented in GAUSSIAN 03.

As will be discussed below, there are significant differences in some of the relative energies obtained from the Becke3LYP and RIMP2 calculations. To gain insight into the origin of these differences we also carried out coupled cluster singles, doubles (triples) [CCSD(T)][140,141] coupled cluster single point calculations for the various minima using the 6-31+G(d) basis

set and the RIMP2 geometries.

5.4 CONFORMATIONAL ASSIGNMENTS AND CALCULATED STATIONARY POINTS ON THE POTENTIAL-ENERGY SURFACE OF TRYPTAMINE

The present work on conformational isomerization dynamics of TRA builds off previous studies that have assigned the observed $S_1 \leftarrow S_0$ vibronic transitions to particular conformational isomers.[115,129,11,130,13,131] The recent high-resolution study of the origin bands of the isomers by Nguyen *et al.*[131] have provided convincing evidence for the assignments given in Figure 5.2(a). The labels in the figure make use of a shorthand notation for the conformers which designates the position of the amino group relative to the indole ring: Anti, *gauche* on the phenyl (Gph), and *gauche* on the pyrrole (Gpy) side of indole.[115] The label in parentheses refers to the direction of the amino nitrogen lone pair relative to the indole ring.

5.4.1 Conformational minima

The flexible ethylamine side chain present in TRA has a total of four coordinates along which large-amplitude motion can occur [Figure 5.2(b)]. These include internal rotation about the $C17$-$N20$ (dihedral angle ψ), $C16$-$C17$ (dihedral angle β), and $C15$-$C16$ (dihedral angle α) bonds and inversion of the NH_2 group. Table 5.1 summarizes the computed Becke3LYP values of these torsional angles for all minima located on the potential-energy surface. The geometrical parameters obtained at the RIMP2 level are reported in Table A in the supplementary material.

The seven lowest-energy minima (as determined from the Becke3LYP calculations) share a common configuration about the $C15$-$C16$ bond that points the $C16$-$C17$ bond approximately perpendicular to the indole ring ($\alpha = \pm 90\circ$). The inversion of the NH_2 group has a barrier high enough that it is safe to conclude that the lowest-energy conformers differ

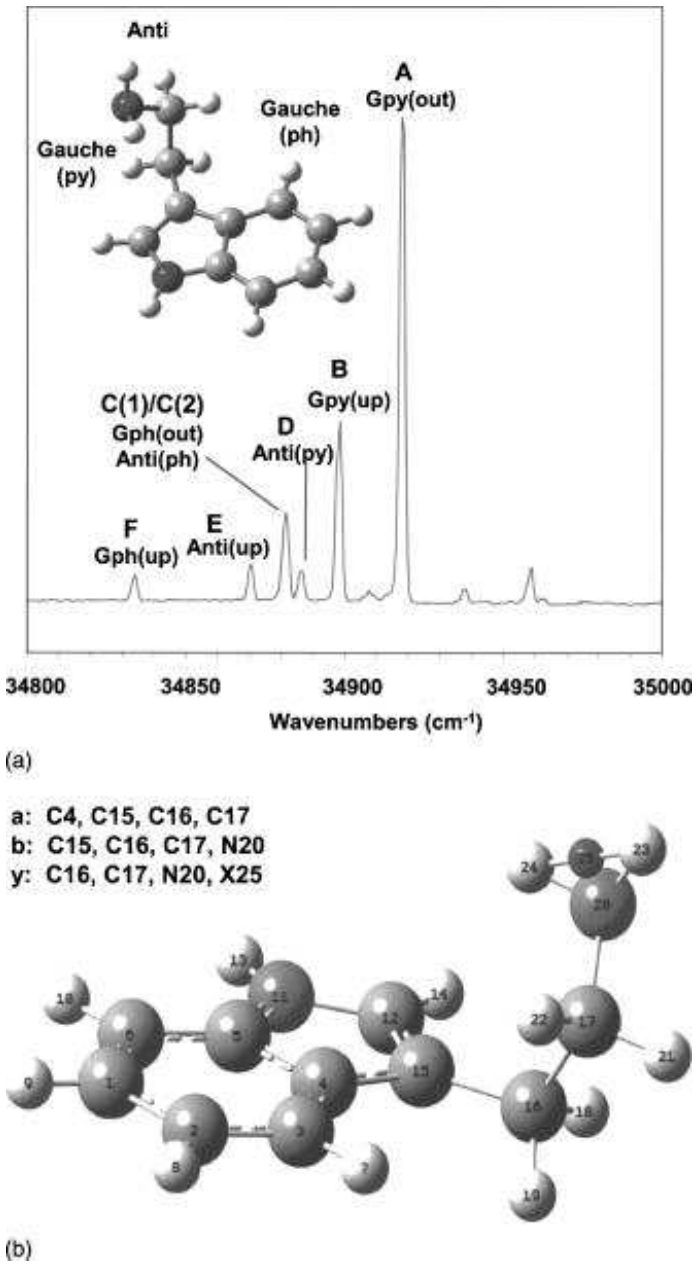

Figure 5.2: (a) LIF excitation spectrum of tryptamine in the region of the $S_1 \leftarrow S_0$ origins. Seven conformations are observed under supersonic conditions. The ethylamine side chain adopts several positions relative to the indole ring as shown and labeled in the inset. (b) Tryptamine dihedral angle definitions used in this work. Note that atom 25 is a "dummy" atom used to simplify the motions of the amino rotation.

Table 5.1: Dihedral angles (degrees) of local minima of tryptamine. For each conformer, with the exception of G, there is a second structure differing only by exchange of the two NH_2 H atoms. Results from Becke3LYP/6-31+G(d) calculations

	a-type enantiomers			b-type enantiomers		
Conformer	α	β	γ	α	β	γ
A	-76.13	-64.04	122.77	76.13	64.04	-122.77
B	-74.43	-62.80	-1.19	74.43	62.80	1.19
H	-149.79	-66.73	-121.53	149.79	66.73	121.53
C2	-85.08	65.68	-125.62	85.08	-65.68	125.62
J	-68.60	82.57	133.11	68.60	-82.57	-133.11
F	-91.15	61.40	2.10	91.15	-61.40	-2.10
C1	-76.06	-179.37	-126.15	76.06	179.37	126.15
E	-76.51	178.72	-0.75	76.51	-178.72	0.75
D	-75.60	176.27	125.88	75.60	-176.27	-125.88
G	-179.99	180.00	0.00	179.99	-180.00	0.00
I	-177.92	178.73	125.48	177.92	-178.73	-125.48

primarily in the angles of internal rotation about the $C16$-$C17$ and $C17$-$N20$ bonds (β and ψ). As a result, it is useful to consider the potential-energy surface as a function of β and ψ shown in Figure 5.3. The threefold character of the potential along each of these coordinates produces nine conformational minima, seven of which are observed experimentally. The structures associated with these minima are shown in Figure 5.3(a), and the computed energies of the minima and transition states (first-order saddle points) are given in Figure 5.3(b). The two unobserved conformers are those in which the nitrogen lone pair points in toward the indole π cloud [Gpy(in)/H and Gph(in)/J], which destabilizes these minima relative to the others. In conformer H, this leads to a substantial distortion of the structure in which the side chain rotates to about $-150.0°$ about the $C15$-$C16$ bond so that the nitrogen lone pair is stabilized by interaction with an aromatic CH group. One could argue that the distortion is so large that structure H does not actually belong on the two-dimensional (2D) potential-energy surface depicted in Figure 5.3.

Two other minima, labeled G and I in the tables, have the heavy atoms of the ethylamine side chain lying in or close to the plane of the aromatic ring [Figure 5.4(a)]. These minima are formed by internal rotation of each of the three "anti" structures E, C(1), and D about the $C15$-$C16$ bond. These structures highlight the possibility that pathways to isomerization could swing the ethylamine side chain from one side of the indole plane to the other. As Figure 5.4(b) shows, each of the conformational minima has a mirror image isomer. These enantiomers (labeled a and b) are spectroscopically indistinguishable, but could play a role in isomerization pathways that swing the ethylamine side chain from one side of the indole ring to the other.

Finally, a combination of inversion and internal rotation of the NH_2 group swaps the positions of the two hydrogens. These spectroscopically indistinguishable isomers [labeled with and without a prime (‘)] are relevant to isomerization pathways that involve these coordinates.

The relative energies of the minima computed at several levels of theory are given in Table 5.2. The relative energies at the Becke3LYP/6-31+G(d) and Becke3LYP/aug-cc-pVDZ

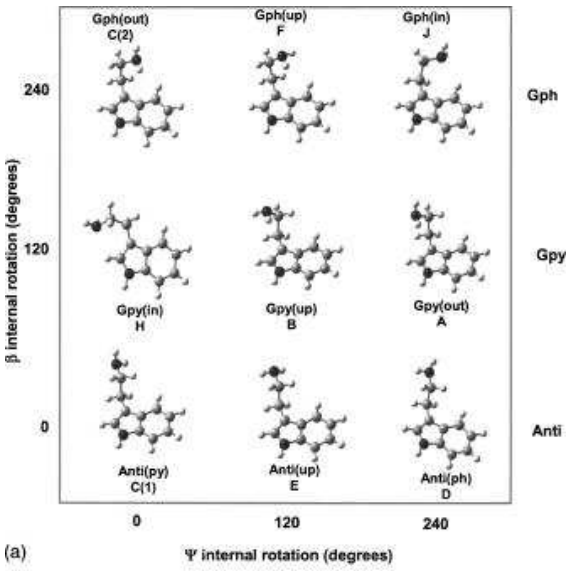

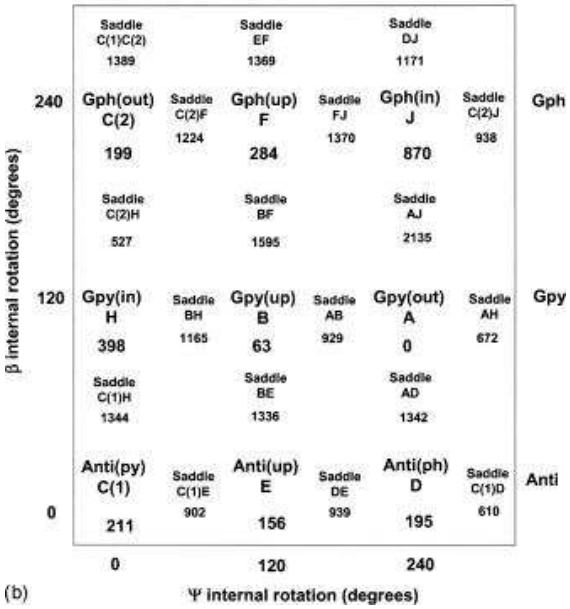

Figure 5.3: (a) Schematic PES of the nine calculated minima of tryptamine and their abbreviated structural designations plotted along two flexible coordinates Ψ and β corresponding to an amino internal rotation ($C17$-$N20$) and a $C16$-$C17$ rotation, respectively. (b) The calculated energies of the minima and all associated transition states interconnecting all minima about the two internal coordinates. All energies are in kcal/mol from B3LYP/6-31+G(d) optimizations employing the QST3 algorithm for the transition state structures.

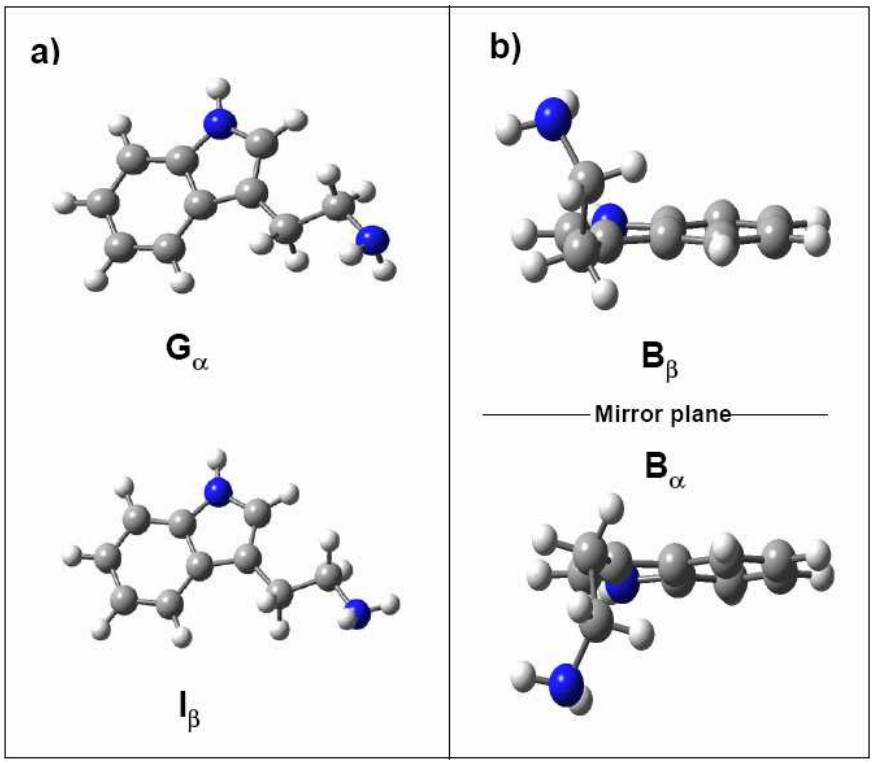

Figure 5.4: Two minima not shown on the schematic PES which have the ethylamine side chain in or near the plane of the aromatic ring. (b) Each of the minima has a mirror image isomer. Conformer B of tryptamine is highlighted as an example. These isomers and their mirror images could play a role in isomerization pathways.

levels of theory are in fairly good agreement. Stress is placed on the Becke3LYP/6-31+G(d) level since the transition state optimizations with the Becke3LYP method were carried out only with the same basis set. Inspection of these results reveals that A, B, C2,and F are preferentially stabilized by 0.6-1.8 kcal/mol relative to the other minima when going from the Becke3LYP to the RIMP2 method.

For all minima the relative energies from the RIMP2/aug-cc-pVDZ and MP2/6-31+G(d) are in fairly good agreement, which indicates that basis set superposition error[7] is not the origin of the discrepancies between the Becke3LYP and MP2 results. In order to determine the origin of the inconsistencies between the RIMP2 and Becke3LYP results, we also carried out CCSD(T)/6-31+G(d) calculations at several of the local minima using the Becke3LYP/6-31+G(d) and RIMP2/aug-cc-pVDZ geometries. In all cases the relative energies obtained from the CCSD(T) calculations are in good agreement with the RIMP2 results. This leads us to conclude that the stabilization of A, B, C2, and F relative to the other conformers is a consequence of a greater importance of dispersion interactions in the former set of minima. Further support for this conclusion is provided by the results of the Hartree-Fock calculations, namely, the energy lowering in going from the Hartree-Fock to the MP2 method is appreciable greater for A, B, C2, and F than for the other conformers.

Figure 5.5 summarizes the energies of the various conformers calculated at the different levels of theory, with conformer *I* being chosen as the zero of energy. This figure underscores the close agreement between the RIMP2 and CCSD(T) results and the fact that the Becke3LYP method is giving relative energies roughly intermediate between the Hartree-Fock and CCSD(T) results. Further it is seen that the dispersion in the relative energies predicted by the various methods grows as one proceeds from the structures with the chain "in the plane" (right-hand side) to the structures with one of the amino NH bonds pointed toward the ring system (left-hand side).

Table 5.2: Relative energies (kcal/mol) of the local minima with respect to A.

Theoretical method[a]	Conformer										
	A	B	C1	C2	D	E	F	G	H	I	J
HF/aug-cc-pVDZ//RIMP2/aug-cc-pVDZ	0.00	0.33	-0.14	0.74	-0.16	0.06	1.27	0.25	0.92	0.24	2.51
B3LYP/6-31+G(d)//B3LYP/6-31+G(d)	0.00	0.26	0.74	0.54	0.73	0.59	0.84	1.18	1.17	1.45	2.66
B3LYP/aug-cc-pVDZ//aug-cc-pVDZ	0.00	0.31	0.57	0.56	0.57	0.58	0.96	0.93	1.12	1.00	2.55
RIMP2/aug-cc-pVDZ//B3LYP/6-31+G(d)	0.00	0.62	1.59	0.26	1.59	1.68	1.02	2.41	1.93	2.51	3.28
RIMP2/aug-cc-pVDZ//RIMP2/aug-cc-pVDZ	0.00	0.65	1.83	0.21	1.84	1.91	0.95	2.75	2.24	2.86	3.35
RIMP2/aug-cc-pVTZ//RIMP2/aug-cc-pVDZ	0.00	0.56	1.68	0.39	1.68	1.74	1.01	2.54	2.26	2.64	3.34
MP2/6-31+G(d)//RIMP2/aug-cc-pVDZ	0.00	0.67	1.83	0.39	1.83	1.91	1.20	3.04	2.11	3.19	3.30
CCSD(T)/6-31+G(d)//RIMP2/aug-cc-pVDZ	0.00	0.54	1.48	0.36	1.48	1.54	1.09	2.60	1.67	2.76	3.11

[a]The theoretical method specified to the left of the double slash was used to calculate the energies and that to the right of the double slash was used to optimize the geometries.

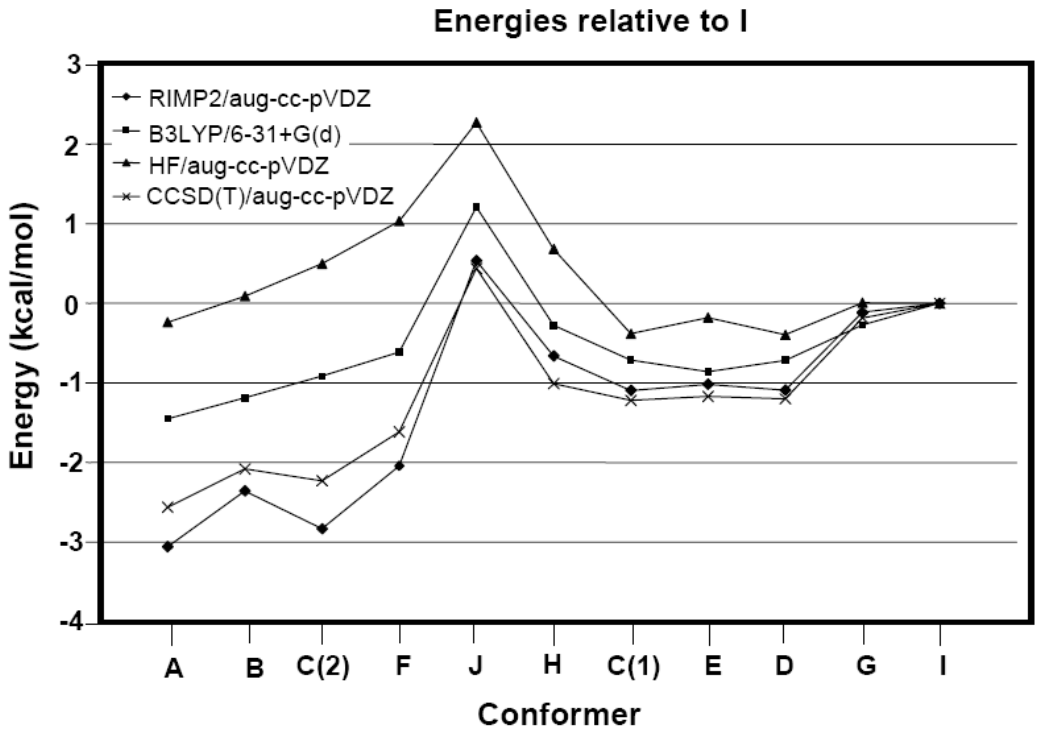

Figure 5.5: Energies of the various conformers calculated at the different levels of theory, with conformer I being chosen as the zero of energy. The results labeled CCSD(T)/aug-cc-pVDZ were estimated using: $E[CCSD(T)/aug-cc-pVDZ] \approx E[CCSD(T)/6-31+G(d)]E[MP2/6-31+G(d)] + E[MP2/aug-cc-pVDZ]$

5.4.2 Transition states

Searches for transition states connecting the minima were carried out at the Becke3LYP/6-31+G(d) level of theory. Structural parameters associated with the transition states are given in Table B of the supplementary material, while their energies relative to the lowest-energy minimum (conformer A) are collected in Table 5.3.

For the most part, the transition state energies obtained from the Becke3LYP and RIMP2 methods are in fairly good agreement, with the largest changes being in those cases for which one is proceeding from one of the minima A, B, C2, or F to one of the other minima. In these cases the energies calculated at the RIMP2 level tend to be about 1 kcal/mol higher than the corresponding values calculated at the Becke3LYP level. The predictions from theory serve as a point of comparison for the experimental results described in the next section.

5.5 EXPERIMENTAL RESULTS AND ANALYSIS

5.5.1 "Upstream" LIF spectra

The hole-filling experimental protocol (Sec. 1.3.1) calls for SEP excitation of a single conformer to take place out of the vibrational zero-point level of that conformer. In doing so, the initial internal energy available to the conformer for isomerization has a single, well-defined value determined by the difference in the wavelengths of the pump and dump lasers. Much of this selective excitation is achieved by the choice of pump wavelength, which is fixed on the S_0-S_1 origin transition of the conformer of interest. In addition, we seek to carry out excitation at a point in the expansion where the vast majority of the populations of the conformers have been collapsed into their vibrational zero-point levels. Figure 5.6 proves that this is the case. There, a LIF excitation spectrum of TRA recorded at the point where SEP excitation occurs ($x/D = 2$) is compared with a downstream spectrum at the probe position ($x/D = 6$). Apart from the broader rotational band contours at $x/D = 2$, hot

Table 5.3: Relative energies (kcal/mol) of the transition states of tryptamine.

Transition state	B3LYP/6-31+G(d)//B3LYP/6-31+G(d)			RIMP2/aug-cc-pvDZ//B3LYP/6-31+G(d)		
	From lowest energy minima	From higher energy minima	Relative to A	From lower energy minima	From higher energy minima	Relative to A
AaBa	3.02	2.76	3.02	3.03	2.40	3.03
AaDa	4.11	3.38	4.11	5.05	3.47	5.05
AaJa	6.34	3.68	6.34	6.16	2.88	6.16
AC2b'	6.00	5.46	6.00	5.94	5.69	5.94
BaEa	3.94	3.61	4.20	4.72	3.66	5.34
BaFa	4.43	3.85	4.69	4.19	3.80	4.82
C1aC2a	3.73	3.53	4.27	4.85	3.52	5.10
C1aIb	1.01	0.29	1.75	1.28	0.35	2.86
C2aFa	3.33	3.03	3.87	3.49	2.73	3.74
C2aJa	2.64	0.51	3.18	3.44	0.41	3.70
C1aDa	1.53	1.53	2.27	1.68	1.68	3.27
DaEa	2.54	2.40	3.13	2.39	2.29	3.97
DaIa	4.02	3.30	4.75	3.59	2.67	5.18
DaJa	2.78	0.86	3.52	2.64	0.94	4.22
Ea'Eb	4.12	4.12	4.71	3.66	3.66	5.33
EaFa	3.62	3.37	4.21	4.32	3.66	5.34
FaJa	4.38	2.56	5.22	4.87	2.60	5.88
EaG	0.95	0.36	1.54	1.18	0.44	2.86
GIb	2.57	2.30	3.75	2.35	2.25	4.76
HaJb'	4.90	3.42	6.08	3.96	2.61	5.89
BbFa'	5.59	5.01	5.85	5.33	4.93	5.95
AaHa	2.42	1.25	2.42	3.01	1.08	3.01
BaHa	3.58	2.67	3.84	3.29	1.99	3.92
C2aHa	6.10	5.46	6.63	6.39	4.72	6.65
C1aHa	3.33	2.89	4.07	3.56	3.22	5.15
C1aEa	2.46	2.31	3.05	2.32	2.23	3.91

bands are very weak. The band at 34911 cm^{-1}, marked with an asterisk, is a $v" = 1 - v' = 0$ hot band of conformer A. By comparing the intensity of this hot band with the corresponding $v" = 0 \rightarrow v' = 1$ vibronic band of TRA(A), we estimate that greater than 95% of the population at $x/D = 2$ is in the ground-state zero-point level.

5.5.2 Single conformation SEP spectra

SEP scans of TRA(A), (B), and (C) are shown in Figures 5.7(a) to 5.7(c), respectively, acquired with the pump laser fixed on the selected $S_1 \leftarrow S_0$ origin in Figure 5.2(a) while the dump laser was tuned over the range from 440 to 1580 cm^{-1} above the zero-point level in the ground state. SEP scans over this energy region produced vibrationally excited TRA conformers with energies ranging from below to well above the thresholds to isomerization. The SEP scan shows a dense vibronic structure throughout this energy range, allowing narrow bounds to be placed on the isomerization barriers. The striking similarities between the spectra are due to the Franck-Condon activity isolated primarily in indole ring vibrations, which are effected only slightly by the conformation of the ethylamine side chain. The spectrum of band C [Figure 5.7(c)] is not, in fact, a single conformation spectrum, but rather a composite of the two unresolved transitions C(1) and C(2) in the origin region [Figure 5.2(a)].

5.5.3 SEP-PT spectra

SEP-induced population transfer spectrum obtained by carrying out SEP excitation on TRA(A) while monitoring transitions B, D, E, and F with the probe laser are shown in Figures 5.8(b) (c) (d) and (e), respectively. The abscissa in these scans is the difference in the wave number between the pump and dump lasers as the dump laser is scanned, which is equivalent to the initial internal energy of conformer A. Positive-going signals indicate an increase in the population of the indicated conformer downstream in the expansion. A comparison of the population transfer spectra with the SEP spectrum in Figure 5.8(a) shows

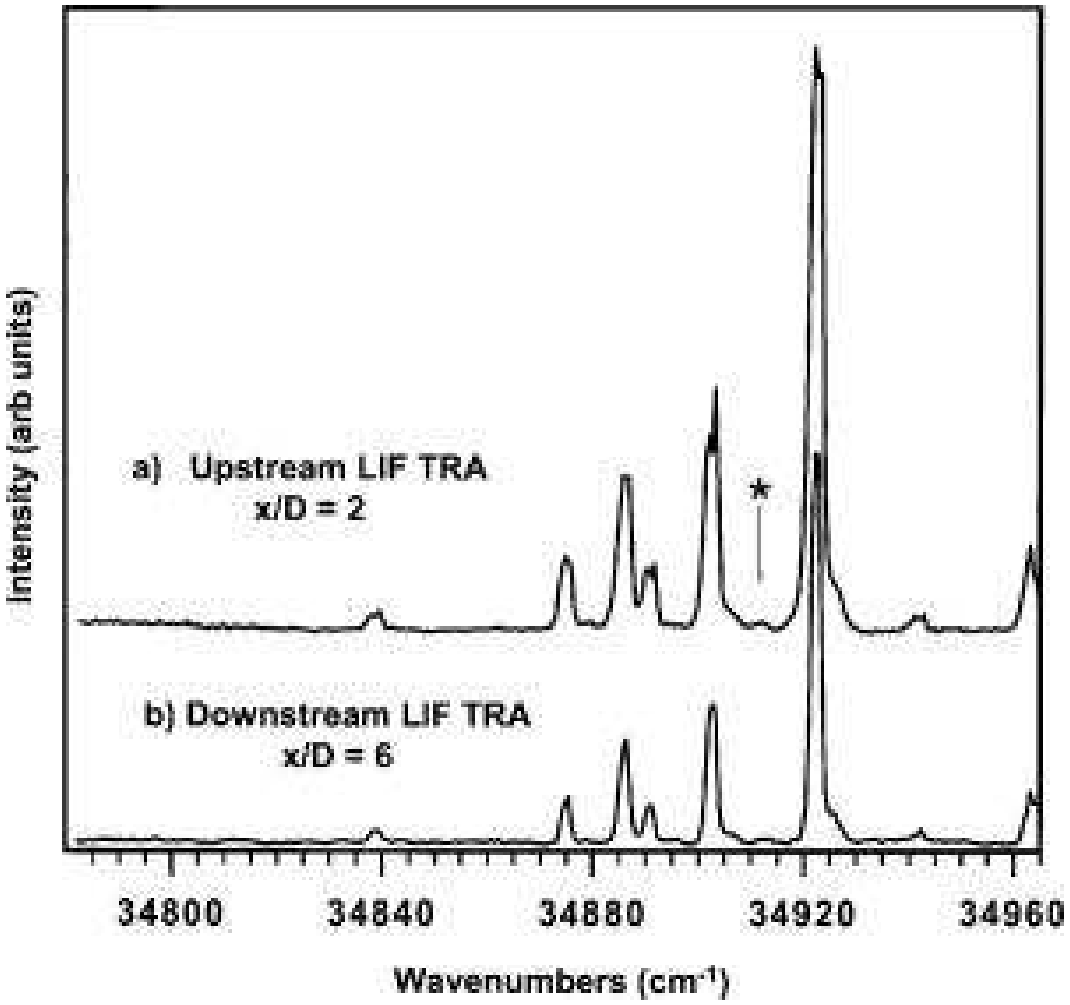

Figure 5.6: (a) LIF excitation spectra taken "upstream" at $x/D = 2$. (b) LIF excitation spectrum taken "downstream" at $x/D = 6$. The asterisk (*) marks a hot band of conformer A at 34911 cm^{-1} due to incomplete cooling.

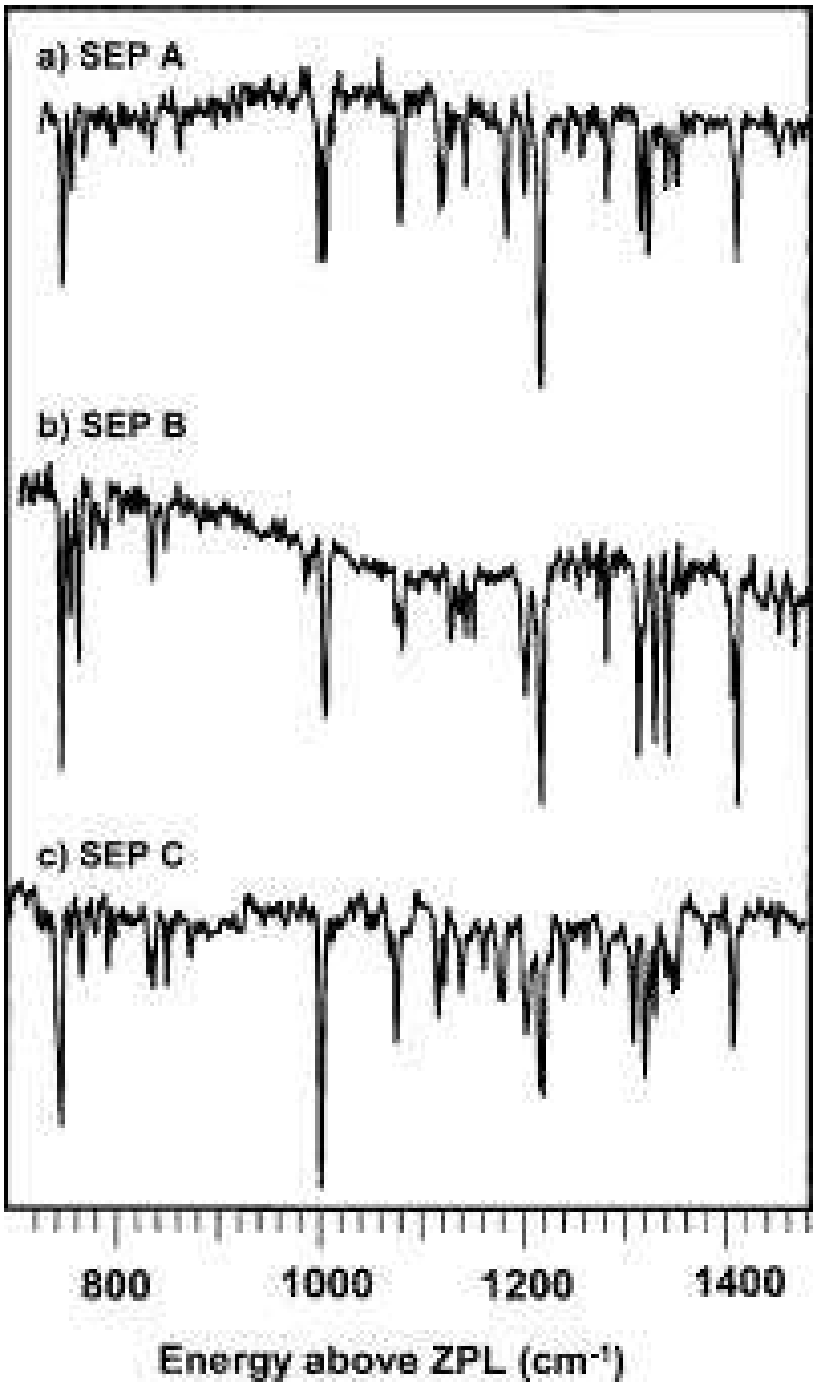

Figure 5.7: SEP spectra of conformers (a) A, (b) B, and (c) C. The striking similarities among the three spectra are due to the Franck-Condon (FC) factors being localized on the aromatic ring.

a sudden turn on of each spectrum at a particular threshold energy that is unique to each conformer.

The analogous scan monitoring transition C in the LIF spectrum with the probe laser [Figure 5.9(c)] contains contributions from both the $A \rightarrow C(1)$ and $A \rightarrow C(2)$ conformer pairs. This spectrum has a threshold at 1000 cm^{-1}, but it is impossible to know from this spectrum which conformer is responsible for the lowest-energy threshold, nor where the second threshold is to be found. Despite their overlapping origin transitions, conformers C(1) and C(2) have slightly different vibronic transitions 413 and 422 cm^{-1} above the C origin [Figure 5.9(a)], which can be used to separate out the thresholds to isomerization for the two conformers.[115] The population transfer spectra taken while monitoring these nonoverlapped transitions determine the threshold for C(1) at 1316 cm^{-1} [Figure 5.9(d)], while that for C(2) occurs at 1000 cm^{-1} [Figure 5.9(e)].

These spectra illustrate several important features of the experimental method. First, the obvious primary results to be derived from the data in Figures 5.8 and 5.9 are the clear energy thresholds for isomerizing conformer A [Gpy(out)] to all six product wells. These thresholds for isomerization are located at 750 ($A \rightarrow B$), 1316 [$A \rightarrow C(1)$], 1000 [$A \rightarrow C(2)$], 1280 ($A \rightarrow D$), 1316 ($A \rightarrow$), and 750 cm^{-1} ($A \rightarrow F$). Second, above threshold, the transitions in the PT spectra have relative intensities commensurate with the corresponding transitions in the SEP spectra of A. This argues against any mode-specific effects in the isomerization process. Third, a lower bound on each threshold for $A \rightarrow X$ isomerization can be determined by identifying the last transition in the SEP spectrum of A that should have been seen in the $A \rightarrow X$ PT spectrum. It is likely that the upper and lower bounds on the energy threshold are bounds on the classical barrier height separating the particular $A \rightarrow X$ reactant-product pair. However, we need to take into account the possible effects on these bounds of tunneling (producing too low an upper bound to the barrier) or a kinetic shift (producing too high a lower bound). These effects will be considered in the Discussion section. Finally, these data raise the prospect of measuring similar thresholds for all 42 $X \rightarrow Y$ product pairs in TRA, leading to a complete characterization of all the stationary points of consequence on

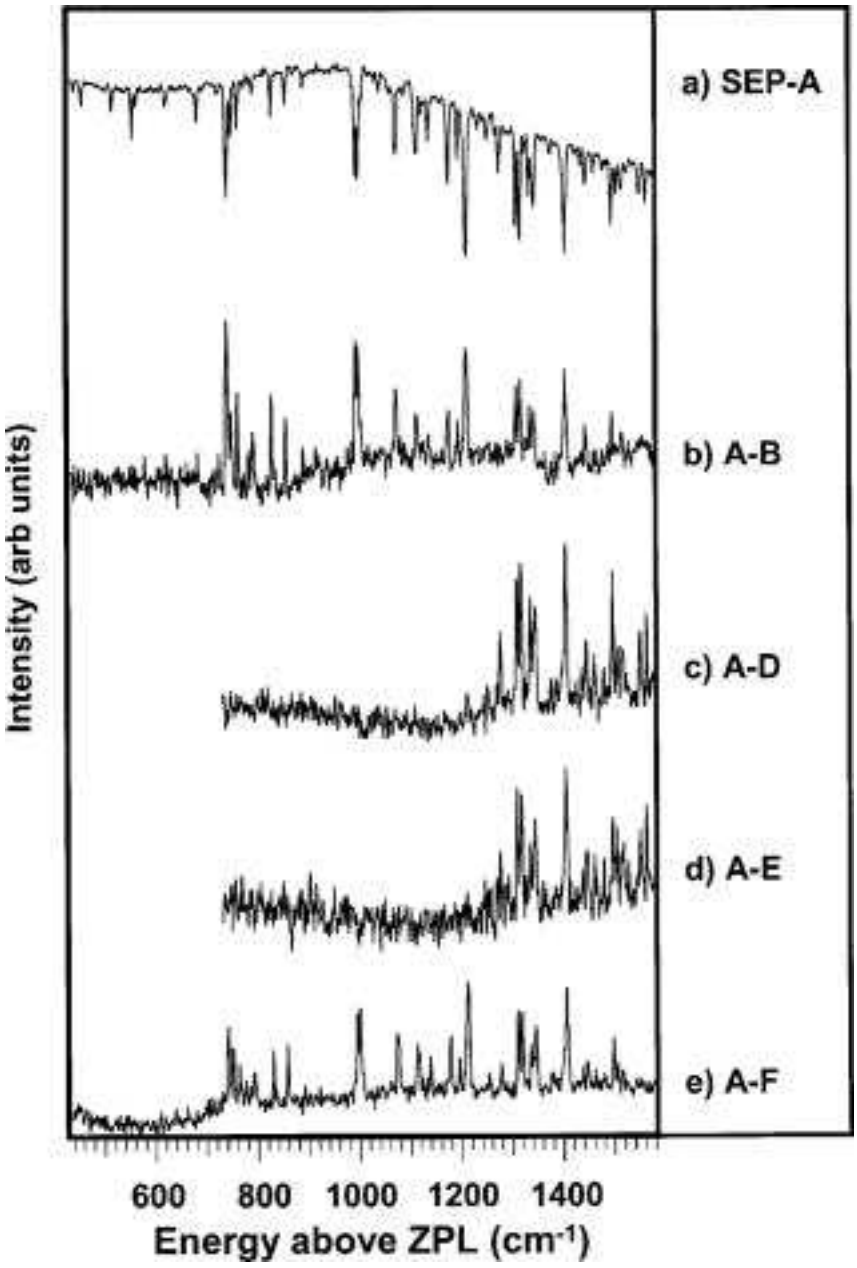

Figure 5.8: (a) SEP spectra of A. (be) SEP-PT spectra recorded by monitoring the $S_1 \leftarrow S_0$ origin transition of the corresponding conformer.

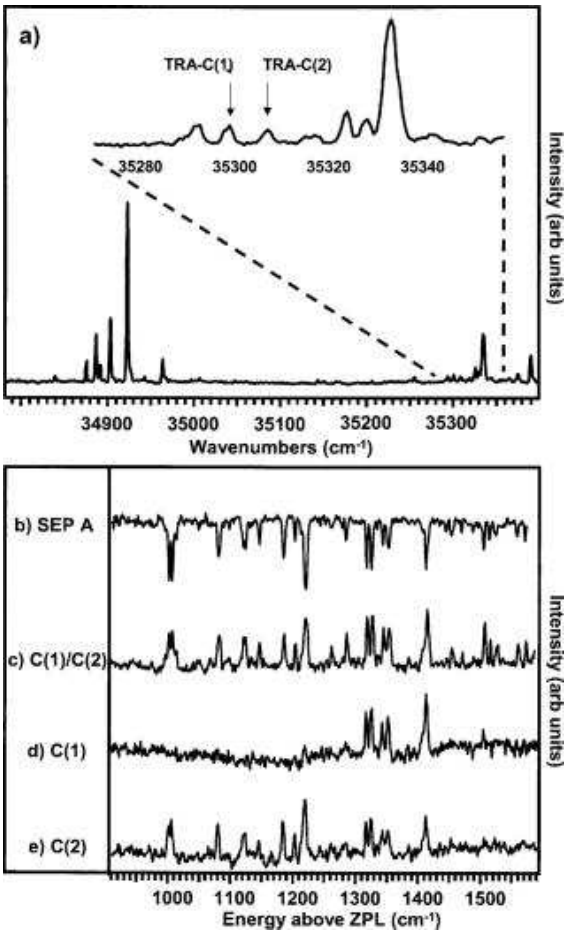

Figure 5.9: (a) An overview LIF spectrum of tryptamine with the expanded region corresponding to vibronic transitions of C(1) and C(2). C(1) and C(2) have vibronic bands at 413 and 422 cm^{-1}, respectively, which were used to probe the energy thresholds free of interference from one another. The (b) SEP spectra of A is compared to the SEP-PT spectra of (c) $A \rightarrow C(1)/C(2)$, (d) $A \rightarrow C(1)$, and (e) $A \rightarrow C(2)$.

the potential-energy surface for TRA. Not surprisingly, such a complete characterization is not possible. The spectra in Figures 5.8 and 5.9 involve observing the population transfer from a large population conformer (A) to small population conformers ($B - F$). The reverse process, namely, pumping a small population conformer into a large population well, becomes increasingly hard to observe as the population in the initial conformer well decreases in size.

Despite this difficulty, the thresholds for several other $X \rightarrow Y$ product pairs were measured. SEP-induced population transfer spectra pumping TRA(B) monitoring transitions A,F, and C with the probe laser are shown in Figures 5.10(b) (c), respectively. Both TRA C(1) and C(2) are being probed when monitoring transition C in the LIF spectrum of Figure 5.2(a). However, based on the lower threshold for $A \rightarrow C(2)$ than $A \rightarrow C(1)$, we tentatively assign this threshold to the $B \rightarrow C(2)$ process. Similarly, the threshold for pumping conformers C(1)/C(2) [whether C(1) or C(2) is not known] back to B was also measured at 750 cm^{-1}, with the likely $X \rightarrow Y$ pair being $C(2) \rightarrow B$. Due to signal-to-noise constraints, only in the $B \rightarrow F$ case was it possible to establish a clear lower bound for the threshold.

The combined experimental data on the thresholds for isomerization are summarized on a 2D potential-energy surface in Figure 5.11. The comparison with theory (Figure 5.3) will be taken up in the Discussion section.

5.5.4 SEP-hole-filling spectra

An interesting consequence of these three sharp thresholds is that they can be used to exert some control over which isomerization products are formed by the SEP step. This is best observed in a hole-filling spectrum, in which the SEP laser wavelengths are fixed to selectively excite a particular conformer to a well-defined vibrational energy while the probe laser is scanned. As Figure 5.12(a) shows, when the dump laser is fixed at a wavelength corresponding to an energy of 750 cm^{-1} above the zero-point level of A, only conformers B and F are formed as products. At 1219 cm^{-1} [Fig. 12(b)], conformer C(2) appears in the product spectrum, while at 1411 cm^{-1} [Figure 5.12(c)], C(1), D, and E are added as well. In Figure 5.12, the population gain in the hot band of A results from incomplete cooling of

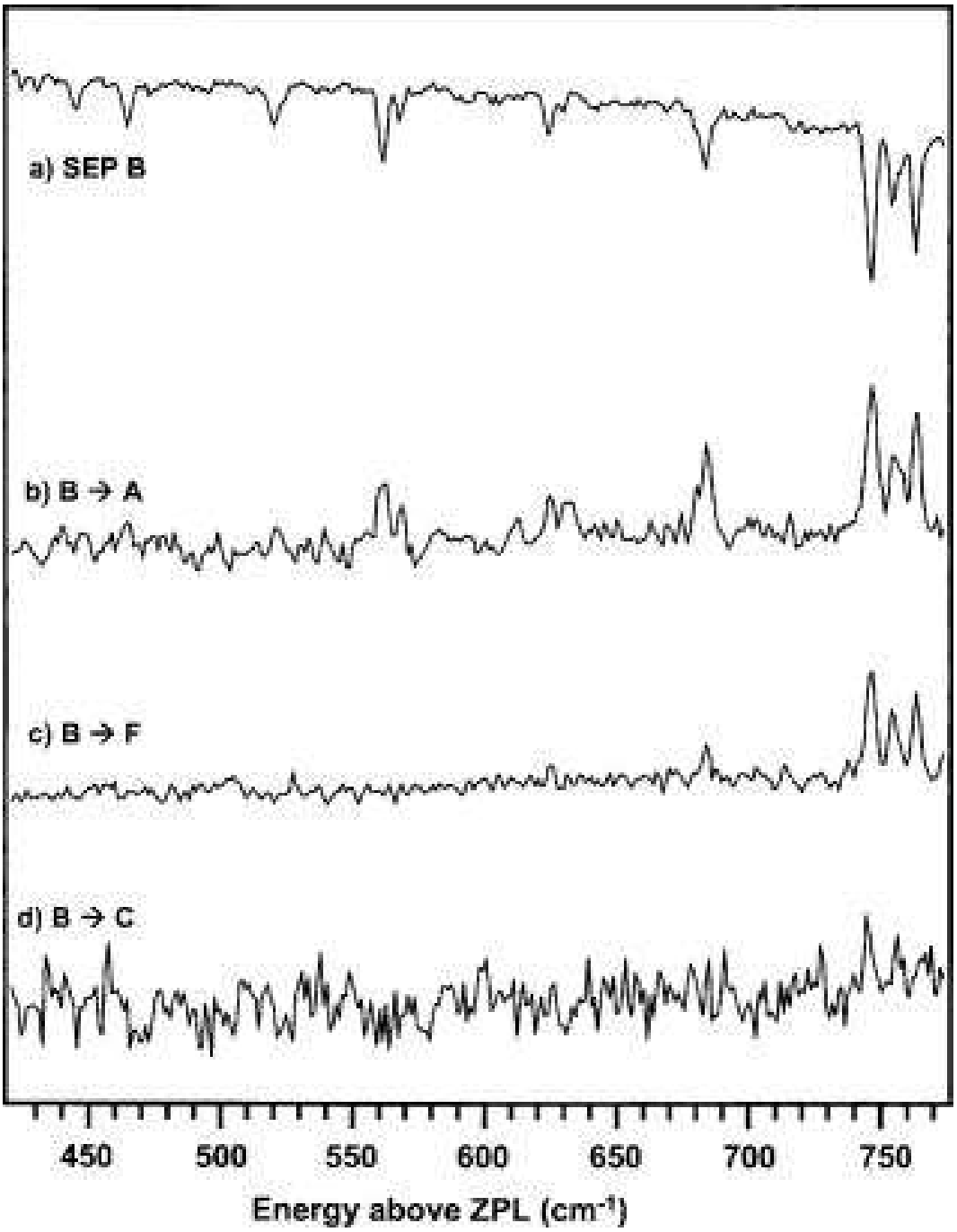

Figure 5.10: The (a) SEP spectrum of B compared to the SEP-PT spectra of (b) $B \rightarrow A$, (c) $B \rightarrow F$, and (d) $B \rightarrow C$.

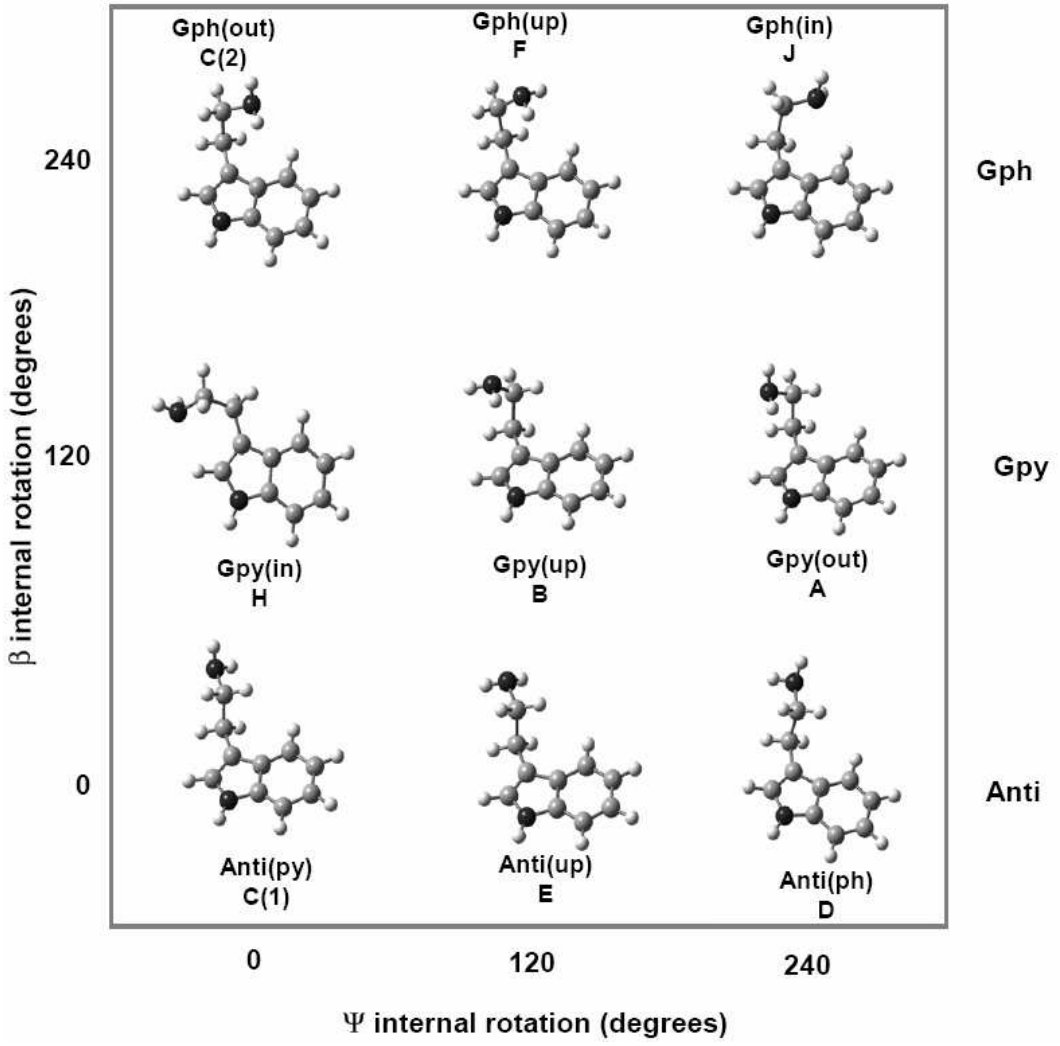

Figure 5.11: Schematic PES for TRA along two flexible internal coordinates. The arrows signify all of the conformational isomerization reactant-product pairs probed experimentally. The numbers associated with the arrows denote the lower and upper bounds to the energy threshold.

a small fraction of the population of A during the recooling step.

Because the scans in Figure 5.12 are taken with a 20/10/20-Hz configuration, the SEP hole-filling signal in transition A reflects the population difference between population reaching the ground state via fluorescence versus SEP. The fluorescing molecules produce a ground-state population dictated by the FranckCondon factors from the fluorescing level, while SEP produces a population only in a single level. When SEP is to a low-energy state, SEP will be more efficient than fluorescence at recooling into the reactant well, producing a gain on transition A, as is observed in Figure 5.12(a). When the dump laser reaches to levels with higher internal energy [Figures 5.12(b) (c)], SEP will be more efficient at isomerization than fluorescence, leading to a depletion on transition A.

5.5.5 Studies of deuterated TRA

Two of the four flexible coordinates in TRA involve internal rotation and inversion of the NH_2 group. These motions are implicated in the high-resolution studies of TRA by Nguyen *et al.*,[131] which have revealed small tunneling splittings (95 MHz) in the origin bands of C(1) and D. In the present studies of isomerization dynamics, tunneling through the barrier could produce an energy threshold below the classical barrier height. One way to test for the effects of tunneling on the isomerization is to compare the isomerization thresholds for the NH_2 and ND_2 isotopomers of TRA.

TRA has three exchangeable hydrogens: the two amino hydrogens and the indole NH, with the former more easily exchanged than the latter. Despite repeated exchange cycles, complete deuteration at all three sites was never achieved, probably due to exchange back in the sample compartment. The degree of isotopic substitution was assessed using resonant two-photon ionization spectroscopy (R2PI). Figure 5.13 shows the R2PI spectra taken while monitoring the four mass channels of the protonated, singly, doubly, and triply deuterated TRA. Based on the intensities of the origin transitions, more than 90% of the sample is either doubly or triply deuterated, with near-complete deuteration at the ND_2 site anticipated. Furthermore, by judicious choice of the SEP pump wavelength on the blue edge of the triply

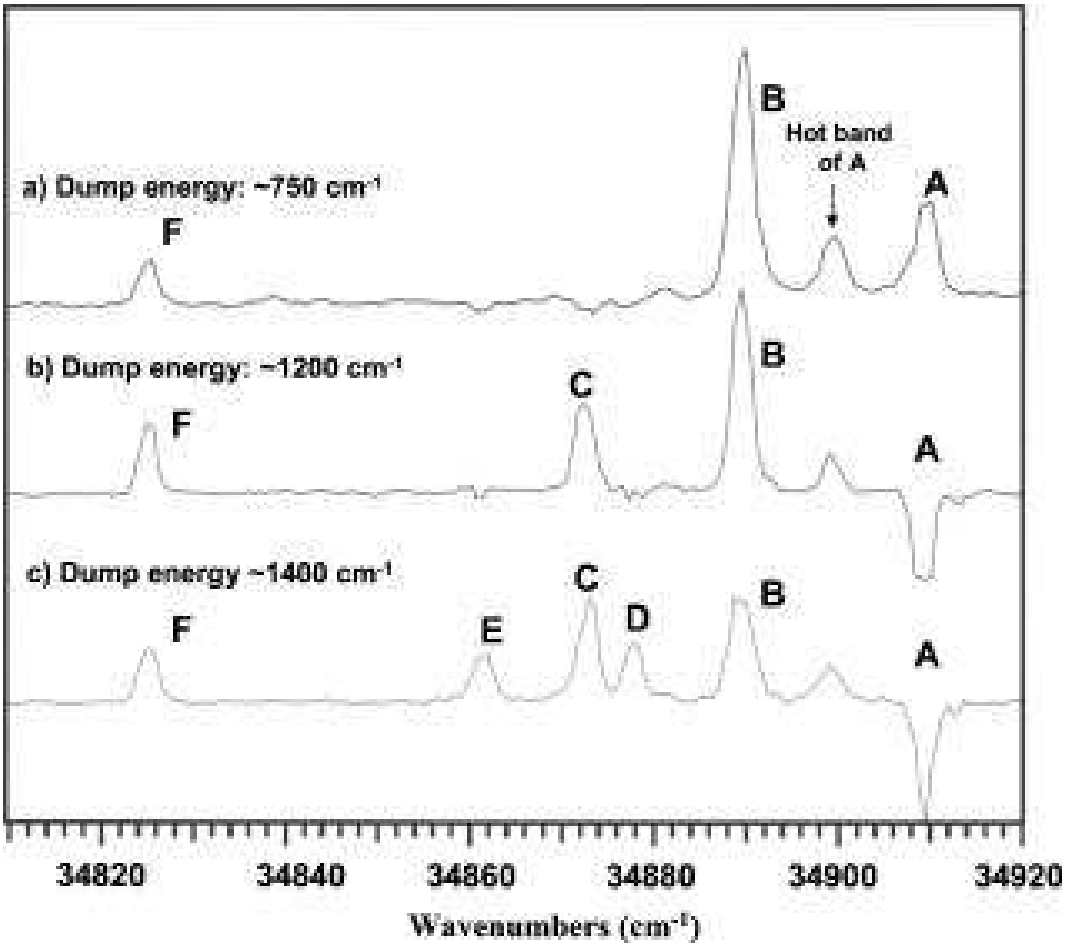

Figure 5.12: SEP-HF spectra after selective excitation of conformer A to vibrational levels with energies of (a) 748, (b) 1219, and (c) 1411 cm^{-1}

deuterated origin (34,927 cm^{-1}, marked in the figure), selective excitation of TRA(d_3) was further enhanced.

Figure 5.14(a) shows the SEP spectrum of conformer A of TRA(d_3) with a pump wavelength set at 34,927 cm^{-1}. Not surprisingly, the spectrum bears a close resemblance to the spectrum of TRA(A,h_3) [Figures 5.14(a) (d)], with small shifts in the frequencies of most bands. These similarities make it possible to determine the threshold to isomerization with comparable accuracies on the upper and lower bounds. SEP-PT spectra were recorded for three reactant-product pairs: $A \rightarrow B$, $A \rightarrow F$, and $B \rightarrow F$. The $A \rightarrow B$ pair was chosen because conformers A and B differ primarily in the orientation of the NH_2 group, suggesting that tunneling might play a role in the isomerization pathway connecting them. The other two pairs have F as their product, and therefore represent pathways where the barriers computed on the 2D potential energy surface (PES) (˜0.1-1300 cm^{-1}, Figure 5.3) are significantly higher than the experiment (<750 cm^{-1}, Figure 5.11).

The SEP-PT spectrum of TRA(A,d_3)→ TRA(B,d_3) exhibits a threshold to isomerization [742 cm^{-1}, Figure 5.14(b)] that is identical to the measured threshold in the nondeuterated system [750 cm^{-1}, Figure 5.8(b)]. Therefore, under the conditions of this experiment, tunneling does not shift the threshold for isomerization of TRA $A \rightarrow B$.

The corresponding PT scan for $A \rightarrow F$ is shown in Figure 5.14(c). A comparison of this scan with the undeuterated analog [Figure 5.14(d)] indicates that the threshold for the d_3 isotope is at 832 cm^{-1}, 90 cm^{-1} above the threshold for the h_3 isotope. The triad of bands near 750 cm^{-1} is clearly missing despite its large intensity in the SEP spectrum. This result is surprising because conformers A [Gpy(out)] and F [Gph(up)] differ in both the orientation and position of the NH_2 group relative to the indole ring. Nevertheless, there is a clear shift in the threshold towards higher values upon deuteration, consistent with tunneling as the source of the shift.

The corresponding results for $B \rightarrow F$ [Figure 5.15] show a similar shift, but are less clear due to a somewhat poorer signal-to-noise ratio in this case. The threshold for TRA(d_3) is at 737 cm^{-1}, with no evidence for the transition at 672 cm^{-1} [Fig. 15(d)]. The corresponding

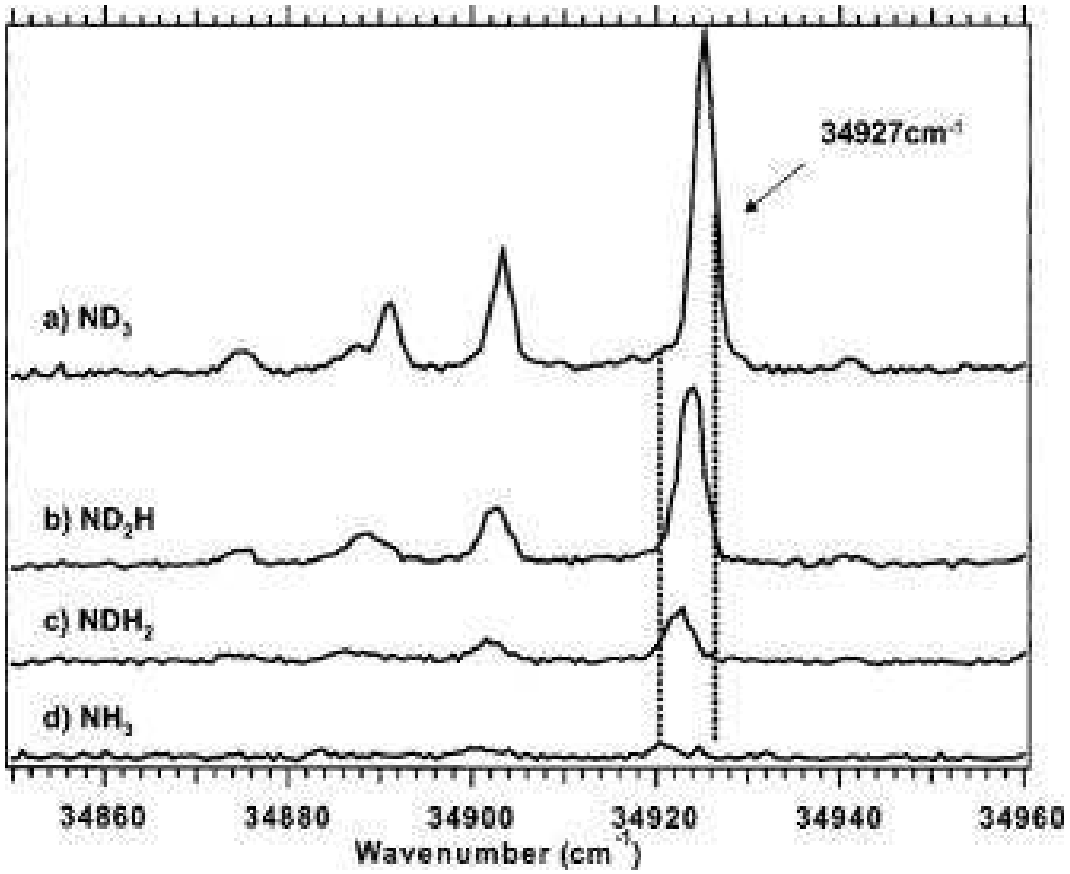

Figure 5.13: The mass-selected R2PI excitation spectra of deuterated tryptamine in the (a) triply deuterated mass channel, (b) doubly deuterated mass channel, (c) singly deuterated mass channel, and (d) the undeuterated tryptamine. The $S_1/leftarrow S_0$ origin transition of tryptamine A is 34,920 cm^{-1} and the excitation wavelength for the deuterated tryptamine A is marked at 34,927 to ensure no interference from the other species in the LIF excitation scheme.

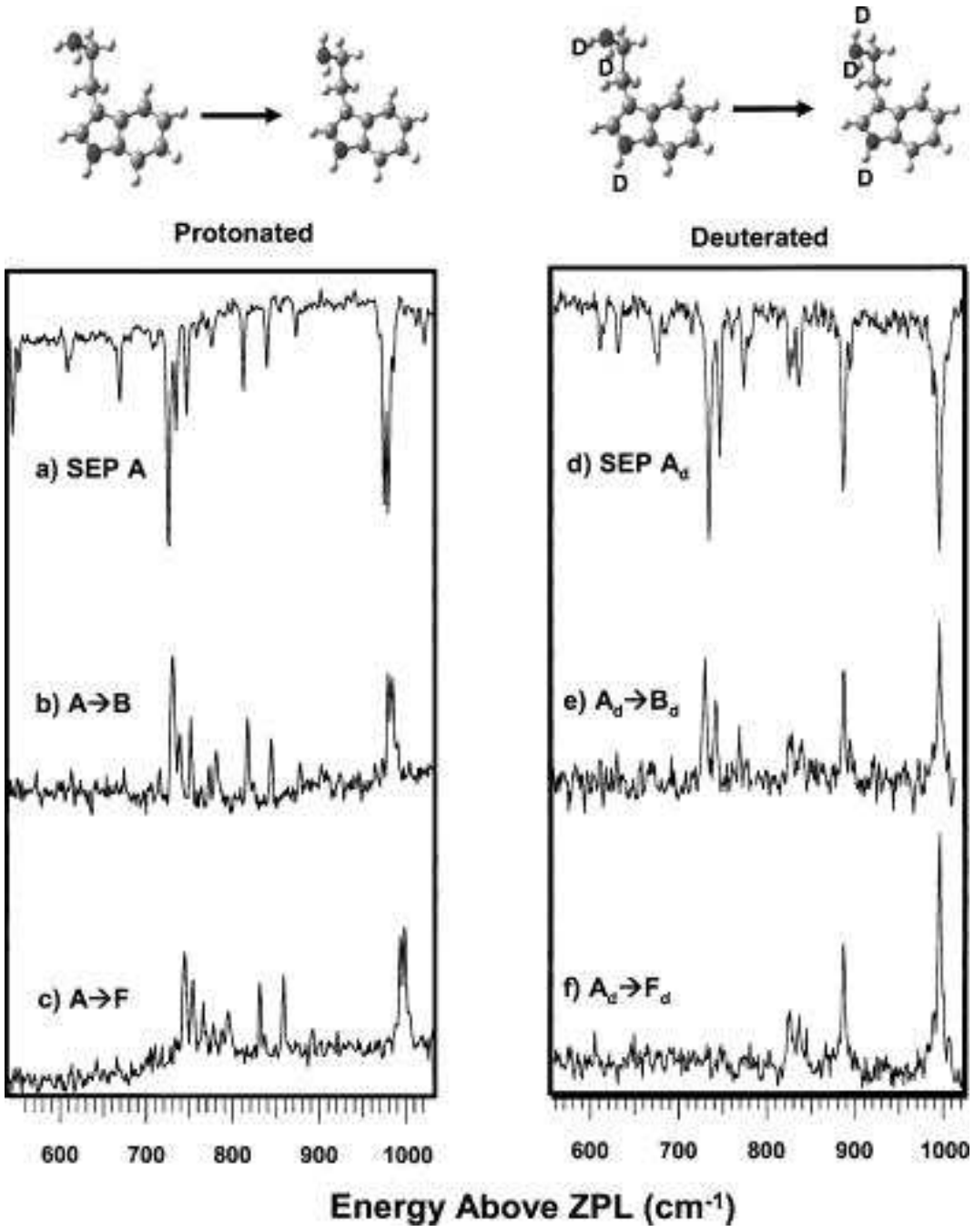

Figure 5.14: The structures indicate the conformational isomerization and deuterated sites. The SEP spectrum of (a) tryptamine is compared to (d) tryptamine-(d_3). The SEP-PT spectra of (b) $A \rightarrow B$ and (c) $A \rightarrow F$ are shown for comparison to (e) $A_d \rightarrow B_d$ and (f) $A_d \rightarrow F_d$, respectively. Only the threshold to isomerization of $A_d \rightarrow F_d$ has any indication of tunneling effects ($\tilde{}100\ cm^{-1}$).

band at 685 cm^{-1} in the spectrum of TRA(h_3,$B \rightarrow F$) is observed, but its intensity is sufficiently small that its absence in the TRA(d_3) scan may be simply because it is hidden in the noise [Figure 5.15(b)].

5.6 DISCUSSION

5.6.1 SEP as a vibrational excitation scheme

The experimental protocol employed in this work uses stimulated emission pumping to initiate conformational isomerization in a single conformational isomer with a well-defined internal energy. SEP excitation is an important extension of an earlier work that used infrared excitation in the hydride stretch region of the infrared.[123,124,125] As noted earlier, the principle drawback of XH stretch infrared excitation is that many of the lowest-energy barriers to isomerization are well below the typical XH stretch $v = 1$ level ($\tilde{}3500cm^{-1} = 10$ kcal/mol). As such, near-IR excitation never directly probes the barriers to isomerization in the threshold region. By comparison, the principle advantage of SEP excitation is that it offers a wide tuning range that stretches from well below the lowest barriers to isomerization up to energies well in excess of these thresholds.

As a result, by observing the onset of a particular $X \rightarrow Y$ population transfer, SEP population transfer spectra provide direct experimental measurements of the energy thresholds for isomerization in individual $X \rightarrow Y$ reactant-product pairs. Furthermore, in cases where the thresholds for both $X \rightarrow Y$ and $Y \rightarrow X$ pairs can be measured, their difference constitutes a measure of the relative energies of minima X and Y. Thus, in principle, step-by-step characterization of all $X \rightarrow Y$ thresholds constitutes a complete characterization of the rate-limiting stationary points on the potential-energy surface for isomerization.

SEP excitation also offers exceptional selectivity in the excitation step. Any vibronic transition that is not overlapped in the ultraviolet spectrum can be used to selectively excite a particular conformation. With supersonic expansion cooling, vibronic bands typically have

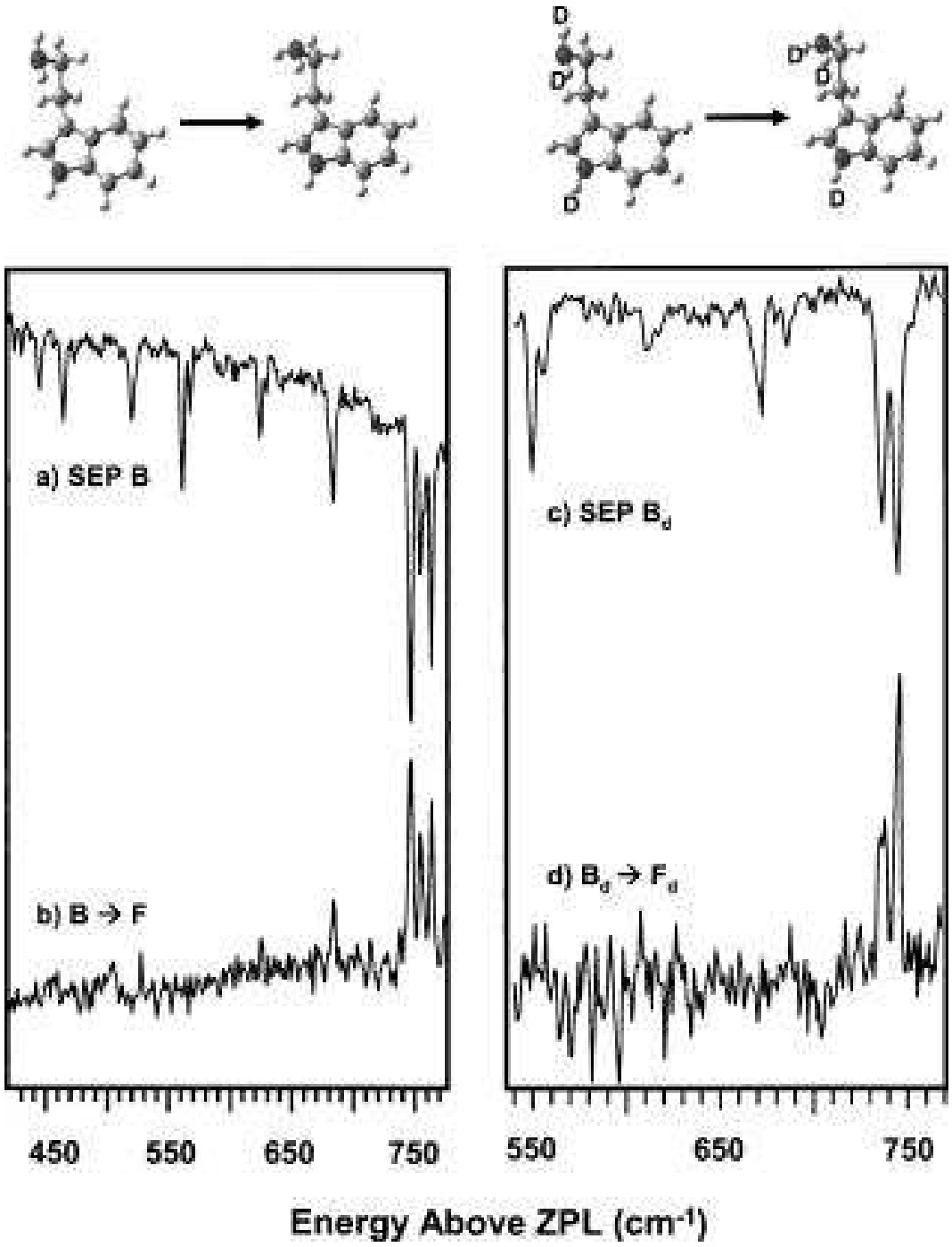

Figure 5.15: (a) SEP spectrum of B compared to (c) the SEP spectrum of B_d. The SEP-PT spectra of (b) $B \rightarrow F$ exhibits a measured threshold almost identical to the (d) SEP-PT of $B_d \rightarrow F_d$. No tunneling effects are observed in the isomerization of conformers B into F.

rotational band contours with widths of 12 cm^{-1}, so different conformers need only shift the electronic origin by this amount in order to enable selective excitation, a very small fraction of the excitation energy (˜30,000 cm^{-1}).

Finally, SEP offers the versatility of carrying out SEP using vibronic bands above the origin in the pump step. In principle, selection of different $S_1(v)$ levels offers a powerful means of changing the FranckCondon intensities to the ground state in the dump step. These changed FranckCondon factors could be used to narrow the bounds on the threshold for isomerization. This potential advantage is more one in theory than practice and, in fact, was not utilized in the present experiment. If intramolecular vibrational redistribution (IVR) is fast compared to the time delay between pump and dump, then the oscillator strength in the dump transition is spread over many transitions that reduce the SEP intensity in any one band considerably. In TRA, we were not able to carry out SEP effectively on bands more than 200 cm^{-1} above the S_1 origin.

The principle disadvantage of SEP in the context of this experimental protocol is that it turns a two-laser IR pump/UV probe experiment into a three-laser experiment (SEP pump-dump, UV probe). Furthermore, in order to use this scheme, the molecule of interest must have an ultraviolet chromophore capable of efficient SEP, with a sufficiently long lifetime to stimulate a significant fraction of the excited-state population back down to the ground state. With the nanosecond lasers employed here, this requires excited-state lifetimes of several nanoseconds. The tryptamine conformers have excited-state lifetimes of 15 ns.[129,131] In addition, the method is not easily adapted to the quantitative measurement of product quantum yields[123,125] because the SEP pump step removes population that is not entirely brought back to the ground state by the dump step.

5.6.2 The comparison between experiment and calculations

In this section, we compare the experimentally determined energy thresholds for isomerization (Figure 5.10) with computed barrier heights, corrected for zero-point energy effects (Figure 5.3). This comparison is justified provided that the experimental upper and lower

bounds bracket the computed classical barrier height. In order for the upper bound on the threshold to be an upper bound on the classical barrier height, tunneling must not play a significant role. The experimental lower bound is a firm lower bound only if the isomerization rate at threshold is fast compared to the vibrational cooling rate, producing a negligible kinetic shift in the threshold.

The measurements on TRA show no evidence for a significant kinetic shift. If vibrational cooling were competing effectively with isomerization, then the bands near threshold in the PT spectra should show a reduced intensity (compared to the SEP spectrum) that depends on the cooling conditions. In TRA, the intensities of transitions above threshold in the PT spectra faithfully reflect those in the SEP spectra, consistent with isomerization occurring on a time scale fast compared to cooling. This is consistent with RiceRamspergerKasselMarcus (RRKM) estimates for the rate constants for isomerization ($> 1 \times 10^9\ s^{-1}$ at threshold) which are fast compared to the anticipated cooling rate by helium (23cm^1 per collision at a collision rate of $4 \times 10^9\ s^{-1}$). A more detailed discussion of the competition between isomerization and collisional cooling will be taken up in the adjoining paper on 3-indole propionic acid (IPA). For our purposes here, we will use the lower bounds from the SEP measurements as the lower bounds on the energy barriers, assuming that the kinetic shifts are negligible.

The data on TRA(d_3) (Sec. 1.5.5 E) indicate that tunneling does play a role in isomerization in certain regions of the potential-energy surface; notably, in pathways leading into well F. Recall that the threshold for $A \rightarrow B$ isomerization was unchanged by deuteration at the amino group, while the thresholds for the $A \rightarrow F$ and $B \rightarrow F$ channels were raised by small but measurable amounts ($\tilde{}100\ cm^{-1}$). Because this shift is small, it could arise from some other effect than tunneling; perhaps due to zero-point energy (ZPE) shifts in the threshold or an increased kinetic shift to the measurement. However, the computed shift in the barrier height due to ZPE differences between TRA(h_3) and TRA(d_3) is less than 10 cm^{-1}. Furthermore, the computed RRKM rate constants at threshold for isomerization of TRA(d_3) are only reduced by about 20% by deuteration, and are still large compared to the rate for cooling. Therefore, tunneling is the most likely explanation for the observed shift

in the $A \rightarrow F$ and $B \rightarrow F$ isomerization thresholds in TRA(d_3). The relationship between the observed thresholds for $A \rightarrow F$ and $B \rightarrow F$ and the classical barrier height depends on the tunneling pathway, an issue to which we shall return shortly. In other measured $X \rightarrow Y$ thresholds, we assume that tunneling plays an insignificant role, and treat the observed energy threshold as an upper bound to the classical barrier height.

5.6.2.1 Relative energies of the minima A first test of the calculated potential-energy surface is to compare the relative energies of the minima with the observed relative populations of the conformers in the expansion in the absence of SEP excitation. One must be careful not to put too much weight on these populations reflecting energy differences alone, because it is possible that the cooling in the expansion can remove population out of the higher-energy minima into the lower ones if the barriers are not too great. In the case of TRA, we do not observe significant changes in these relative populations as a function of distance downstream in the expansion (Figure 5.6), and therefore see some merit in correlating the relative intensities of the observed S_0-S_1 origins with their relative energies. The high-resolution spectra of Nguyen *et al.*[131] show that the intensity of the C(2) origin is about twice that of the C(1) origin. Sorting these intensities from large to small yields, $I(A) > I(B) > I[C(2)] > [I[C(1)], I(D), I(E), and I(F)]$, where the bands in brackets have similar intensities. This suggests that the experimental energy ordering is $E(A) < E(B) < E[C(2)] < \{E[C(1)], E(D), E(E), and E(F)$

This energy ordering matches reasonably well with the DFT energies, while the RIMP2 results would predict greater populations in C(2) and F than observed experimentally. It is possible that the low experimental barriers separating these minima from B (Figure 5.11) provide a pathway for removing population from these minima into B early in the expansion ($x/D < 2$).

5.6.2.2 Barrier heights For most of the measured $A \rightarrow X$ thresholds, the calculated barrier heights, including ZPE corrections, are within a couple of hundred wave numbers

of experiment. For instance, the experimental barriers separating A [Gpy(out)] from any of the three anticonformers [C(1), D and E] are $E_{thresh} \sim 1300\ cm^{-1} = 3.7$ kcal/mol, consistent with the computed barrier heights for AD and BE ($\sim 1300\ cm^{-1}$ for DFT and 16001700 cm^{-1} for RIMP2). The $A \rightarrow B$ threshold is somewhat lower experimentally ($688 < E_{thresh} < 748\ cm^{-1}$) than predicted by theory ($E_{barrier} = 930\ cm^{-1}$ by both methods), but still within this 200 cm^{-1} spread.

The glaring exceptions to this general correspondence between experiment and theory are the $A \rightarrow F$ and $A \rightarrow F$ thresholds. As Figure 5.3 shows, the computed barriers into well F are all up in the 13001500 cm^{-1} range, almost a factor of 2 higher than the experiment. These are the same pathways that show some evidence for tunneling, and it is possible that tunneling accounts for the entire discrepancy between experiment and theory. However, the small shift in threshold induced by deuteration seems to argue against such a simple resolution. Furthermore, since A and F differ along at least two of the flexible coordinates, one would like to pin down the isomerization pathway, whether tunneling or classical in nature.

5.6.2.3 Isomerization pathways The experimental thresholds (Figure 5.15) that connect $A \rightarrow B$, $A \rightarrow F$, and $B \rightarrow F$ are particularly low, suggesting that there is an efficient isomerization pathway connecting these minima. As just noted, this pathway may involve tunneling, but if so, the tunneling penetrates some of the highest computed barriers on the surface, those that surround minimum F. As noted in the initial communication, the observed thresholds are consistent with a pathway from $A \rightarrow F(688 < E_{thresh} < 748\ cm^{-1})$ that passes from $A \rightarrow B(688 < E_{thresh} < 748\ cm^{-1})$ and then from $B \rightarrow F(566 < E_{thresh} < 688\ cm^{-1})$.

The computed potential-energy surface possesses a low-energy trough that connects wells A, H, and C(2) via the AH and HC(2) barriers. A possible way to resolve these differences would be to simply swap the assignments of conformers C(2) and F. These two conformers are both Gph conformers, differing only in the orientation of the NH_2 group. As a result, they have rotational constants which are very close to one another. If this swap in assignments

were made, the calculations would predict an $A \rightarrow F$ barrier of 672 cm^{-1} based on a pathway that goes from Gpy(out) to Gpy(in) ($E_{barrier} = 672cm^{-1}$) and then on to Gph(out) ($E_{barrier} = 527cm^{-1}$). While such a swap is tempting, the arguments that Nguyen used to arrive at the assignments for C(2) and F are quite persuasive, and are consistent with previous assignments based on infrared and vibronic level data.[131]

With or without such a swap in assignments, it is surprising that tunneling would lead to a shift in the $A \rightarrow F$, and $B \rightarrow F$ thresholds, but produce no shift in $A \rightarrow B$, since the pathways from A or B into F necessarily involve motion of the entire NH_2 group from the Gpy to the Gph position (with an effective tunneling mass of $\sim$ 16 amu), while $A \rightarrow B$ isomerization [$Gpy(out) \rightarrow Gpy(up)$] can be accomplished merely by an internal rotation and/or inversion of the NH_2 group ($\sim$2-amu tunneling mass). Of course, this difference in mass of the tunneling group could be compensated for by a narrower width to the barrier. Since the likely isomerization pathway for either $A \rightarrow F$ or $B \rightarrow F$ involves motion of the NH_2 group over the top of the phenyl ring, one wonders whether the interaction of the NH_2 group with the indole π cloud could provide a low-energy tunneling pathway that inverts the NH_2 group as it sweeps across the π cloud. A final resolution of these issues will require theoretical methods that can directly model the tunneling contribution to the isomerization dynamics.

Finally, even in a molecule the size of tryptamine, we are quickly losing our ability to use chemical intuition to identify the important isomerization pathways on the potential-energy surface. The transition states identified in this work are likely only a subset of those needed to fully describe the isomerization dynamics. In particular, isomerization pathways that involve swinging the ethylamine side chain from one side of the indole ring to the other may play a significant role in the isomerization dynamics. The anti configuration supports minima G and I in which the ethylamine side chain is nearly in plane. The barriers into and out of these minima are quite low ($\sim$100 cm^{-1}). Analogous pathways involving motion of the ethylamine group from the Gpy or Gph positions around the edges of the pyrrole or phenyl rings deserve further exploration.

5.7 CONCLUSIONS

Despite its modest size, tryptamine possesses a potential-energy surface for conformational isomerization that is a challenge to characterize via experiment and theory. The population of TRA molecules is spread over seven conformational minima, even with supersonic expansion cooling. A complete characterization of the isomerization process would then require measurement of 42 independent $X \rightarrow Y$ conformer pairs, illustrating the need for new experimental tools capable of studying the process in a conformation specific way. The present paper describes measurements of the energy thresholds for isomerization using conformation-specific SEP excitation, followed by collisional cooling of the products prior to conformation-specific detection via laser-induced fluorescence. The method of SEP-induced population transfer spectroscopy provides a means for measuring the energy thresholds for isomerization of individual $X \rightarrow Y$ conformer pairs free from interference from others present in the expansion.

The application of this method to TRA has demonstrated the power of the method, but it has also raised many unanswered questions, providing a stimulus for future work. First, since the method uses collisions as an integral part of the experimental scheme, isomerization is always viewed in competition with collisional cooling. Ideally, this competition can be used as a means to quantify the energy-dependent rate of isomerization for individual $X(E*) \rightarrow Y$ pairs. It is hoped that such studies can provide critical new tests of RRKM theory, which is undergoing close scrutiny by theory, which suggests that in many circumstances, IVR into the torsional modes may limit the rate of isomerization near threshold. Second, as just discussed in the preceding section, theoretical methods that can explore the isomerization pathways more completely, and include the effects of tunneling, are needed. Third, it is important to compare the results of the present study with analogous studies of isomerization in the absence of collisions, using methods such as those employed by Pate and co-workers. Finally, hole-filling methods can be applied to the study of isomerization in a much wider range of contexts. In the adjoining paper, we will probe the effect of a bound solvent water molecule

on the barrier to intramolecular isomerization in 3-indole propionic acid.[132]

5.8 ACKNOWLEDGEMENTS

We gratefully acknowledge support for the work from the National Science Foundation (Grant No. CHE-0242818). One of the authors (J.R.C.) acknowledges partial support from the Purdue Research Foundation for a Graduate Student Assistantship.

APPENDIX

TRYPTAMINE TRANSITION STATE STRUCTURES

Figure A1: Transition-state structures of tryptamine.

BIBLIOGRAPHY

[1] Mao, W.; Mao, H.; Goncharov, A.; Struzhkin, V. V.; Guo, Q.; Hu, J.; Shu, J.; Hemley, R.; Somayazulu, M.; Zhaoi, Y. *Science* **2002**, *297*, 2247.

[2] Ripmeester, J. A.; Ratcliffe, C.; Klug, D. D.; Tse, J. S. *Ann. N. Y. Acad. Sci.* **1994**, *715*, 161.

[3] Kuhs, W. F.; Chazallon, B.; Radaelli, P. G.; Pauer, F. *J. Incl. Phenom.* **1997**, *29*, 65.

[4] Hill, T. L. *J. Chem. Phys.* **1948**, *16*, 399.

[5] Yu, H.; van Gunsteren W. F., *J. Chem. Phys.* **2004**, *121; 19*, 9549.

[6] Forester, T. R.; Smith, W. *The DLPOLY-2.0 Reference Manual, CCLRC, Daresbury Laboratory, Warrington, England version 2.0 edition 1995.*

[7] Boys, S. F.; Bernardi, F. *Mol. Phys.* **1970**, 553.

[8] Lee, C.; Yany, W.; Parr, R. G. *Phys. Rev. B: Condens. Matter Mater. Phys.* **1988**, 785.

[9] Bernholdt, D. E.; Harrison, R. J. *Chem. Phys. Lett.* **1996**, 470.

[10] Feyereisen, M.; Fitzgerald, G.; Komornicki, A. *Chem. Phys. Lett.* **1993**, 359.

[11] Park, Y. D.; Rizzo, T. R.; Peteanu, L. A.; Levy, D. H. *Journal of Chemical Physics* **1986**, *84*, 6539–49.

[12] Philips, L. A.; Levy, D. H. *Journal of Chemical Physics* **1988**, *89*, 85–90.

[13] Wu, Y. R.; Levy, D. H. *Journal of Chemical Physics* **1989**, *91*, 5278–5284.

[14] Dian, B. C.; Clarkson, J. R.; Zwier, T. S. *Science* **2004**, *303*, 1169–1173.

[15] Peng, C.; Schegel, H. B. *Israel J. Chem* **1993**, *33*, 449.

[16] Sloan, E. D. *Clathrate Hydrates of Natural Gases*; Marcel Dekker, New York, 1990.

[17] Atwood, J.; Davies, J. E. D.; Macnicol, D. D. *Inclusion Compounds*; Oxford University Press, Oxford, 1991.

[18] Davidson, D. W. *Water: A Comprehensive Treastise; Frank, F., Ed.; Plenum Press New York, 1973 2*, year.

[19] Jeffery, G. A.; Macnicol, D. D.; Bishop, R. *Comprehensive Supramolecular Chemistry Vol. 6*; 1996.

[20] Ripmeester, J. A.; Tse, J. S.and Ratcliffe, C.; Powell, B. M. *Nature* **1987**, *119*, 173.

[21] Udachin, K. A.; Ratcliffe, C.I.and Enright, G. D.; Ripmeester, J. A. *Supramol. Chem.* **1997**, *8*, 173.

[22] Sloan, E. D. *Nature* **2003**, *426*, 353.

[23] Udachin, K. A.; English, N. J.; Ratcliffe, C.I.and Ripmeester, J. A. *J. Am. Chem. Soc.* **197**, *119*, 11481.

[24] Udachin, K. A. Ratcliffe, C. R. J. A. *Angew. Chem. Int. Ed.* **2001**, *40*, 1303.

[25] Mcmullan, R. K.; Jeffery, G. A.; Jordan, T. H. *J. Chem. Phys.* **1967**, *47*, 1229.

[26] Davy, H. *Philos. Trans. R. Soc. London* **1811**, *101*, 1.

[27] Faraday, M. *Philos. Trans. R. Soc. London* **1823**, *113*, 60.

[28] Clausen, W. F. *J. Chem. Phys.* **1951**, *19*, 259.

[29] von Stackelberg, M.; Muller, H. R. *J. Chem. Phys.* **1951**, *29*, 2425.

[30] Clausen, W. F. *J. Chem. Phys.* **1951**, *19*, 1425.

[31] Muller, H. R. von Stackelberg, M. *Naturwissenschaften* **1952**, *39*, 20.

[32] Pauling, L.; Marsh, R. E. *Pro. Natl. Acad. Sci. U.S.A.* **1952**, *38*, 112.

[33] Hammerschmidt, E. G. *Ind. Eng. Chem.* **1934**, *26*, 851.

[34] Suess, E.; Bohrmann, G. an dGreinert, J.; Laush, E. *Sci. Am.* **1999**, *281*, 52.

[35] Kvenolden, K. *Proct. Int. Japan Natl. Oil Comp, Chiba City, Japan* **1998**.

[36] Nesbit, E. *Nature* **1990**, *23*, 347.

[37] Dresselhaus, M. S.; Thomas, I. L. *Nature* **2001**, *414*, 332.

[38] Schlapbach, L.; Zuttel, A. *Nature* **2001**, *414*, 353.

[39] Dyadin, Y. A.; Larionov, E. G.; Manakov, A. Y.; Zhurko, F. V.; Aladki, E. Y.; V, M. T.; Komarov, V. Y. *Mendeleev. Commun.* **1991**, 171.

[40] Mao, W. L.; Mao, H. K. *Proc. Natl. Acad. Sci.* **2004**, *101*, 708.

[41] Vos, W. L.; Finger, L. W.; Hemley, R. J.; Mao, H. K. *Phys. Rev. Lett.* **1994**, *71*, 3150.

[42] Powell, H. M. *J. Chem. Soc.* **1948**, 61.

[43] Deaton, W. M.; Frost, E. M., J. *U.S. Bur Mines Monogr.* **1946**, 8.

[44] Waals, J. H. v. d.; Platteeuw, J. C. *Adv. Chem. Phys.* **1959**, *2*, 1.

[45] Somayazulu, M. S.; Finger, L. W.; Hemley, R. J.; Mao, H. K. *Science* **1996**, *271*, 1400.

[46] Loubeyre, P.; Letoullec, R.; Pinceaux, J. P. *Phys. Rev. Lett.* **1994**, *72*, 1360.

[47] www.eere.energy.gov,.

[48] Lokshin, K. A.; Zhao, Y.and He, D.; Mao, W. L.; Mao, H. K.; Hemley, R. J.and Lobanov, M. V.; Greenblatt, M. *Phys. Rev. Lett.* **2004**, *93*, 125503.

[49] Mao, W.; Mao, H. K. *U.S.A. Patent 6735960* **2002**.

[50] von Stackelberg, M. *Naturwissenschaften* **1949**, *36*, 11–12.

[51] Mao, W. L.; Mao, H. K.; Goncharov, A. F.; Struzhkin, V. V.; Guo, Q.; Hu, J.; Hemley, R.; Somayazulu, M.; Y., Z. *Science* **2002**, *297*, 2247.

[52] Patchkovskii, S.; Tse, J. *Proc. Natl. Acad. Sci. U. S. A.* **2003**, *100*, 14645.

[53] Sluiter, M. F.; Adachi, H.; Belosludov, R. V.; Belosludov, V.; Kawazoe, Y. *Materials Transactions* **2004**, *45; 5*, 1452.

[54] Alavi, S.; Ripmeester, J. A.; Klug, D. D. *J. Chem. Phys.* **2005**, *123*, 024507.

[55] Inerbaev, T. M.; Belosludov, V. R.; Belosludov, R. V.; Sluiter, M.; Kawazoe, Y. *Computational Materials Science* **2006**, *36*, 229.

[56] Patchkovskii, S.; N., Y. S. *Phys. Chem. Chem. Phys.* **2004**, *6*, 4152.

[57] Ponder, J. W.; Case, D. A. *Adv. Protein Chem.* **2003**, *66*, 27.

[58] Stillinger, F. H. *Science* **1980**, *209*, 451.

[59] Halgren, T. A.; Damm, W. *Curr. Opin. Struct. Biol.* **2001**, *11*, 236.

[60] Rick, S. W.; Stuart, S. J. *Reviews in Computational Chemistry* **2002**, *89-154*, year.

[61] Verlet, L. *Physical Review* **1967**, *159*, 98.

[62] English, N. J.; Macelroy, J. M. D. *J. Comput. Chem.* **2003**, *24*, 1569.

[63] English, N. J.; Johnson, K. J.; Taylor, C. E. *J. Chem. Phys.* **2005**, *123*, 244503.

[64] Rick, S. W.; Stuart, S. J.; Berne, B. J. *J. Chem. Phys.* **1994**, *101*, 6141–6156.

[65] Jiang, H.; Jordan, K. D.; Taylor, C. E. *J. Phys. Chem. B* **2007**, *111*, 6486.

[66] Ren, P.; Ponder, J. W. *J. Phys. Chem. B* **2003**, *107*, 5933.

[67] Ren, P.; Ponder, J. J. *J. Phys. Chem. B* **2003**, *107*, 5933.

[68] Ren, P.; Ponder, J. W. *J. Chem. Phys. B* **2004**, *108*, 13427.

[69] Smith, W.; Forester, T. R. *J. Mol. Graphics* **1996**, *14*, 136.

[70] Eisenberg, D.; Kauzmann, W. *The Structure and Properties of Water (Clarendon Press, Oxford, 1969).*

[71] Wallqvist, A.; Mountain, R. D. *Reviews in Computational Chemistry* **1999**, 183–247.

[72] Finney, J. L. *J. Mol. Liq.* **2001**, *90*, 303.

[73] Guillot, B. *J. Mol. Liq.* **2002**, *101*, 219.

[74] Ponder, J. W.; Case, D. A. *Adv. Protein Chem.* **2003**, *66*, 27.

[75] Cornell, W. D. Cieplak, P. a. C. I. *J. Am. Chem. Soc.* **1995**, *117*, 5179.

[76] MacKerrell, A. D.; Bashford, D.; Bellot, M. *J. Phys. Chem. B* **1998**, *102*, 3586.

[77] van Gunsteren W. F.,; Billeter, S. R.; Eising, A. A.; Hunenberger, P. H.; Mark, A. E.; Scott, W. R. P.; Tironi, I. G. *Biomolecular Simulation: The GROMOS manual and User Guide (vdf Hochschulverlag, ETH Zurich, Switzerland)* **1996**.

[78] Schuler, L. D.; Daura, X.; van Gunsteren W. F., *J. Comput. Chem.* **2001**, *22*, 1205.

[79] Jorgensen, W. L.; Maxwell, D. S.; Tirado-Rivers, J. *J. Am. Chem. Soc.* **1996**, *118*, 11225.

[80] Bernal, D.; Fowler, R. H. *J. Chem. Phys.* **1933**, *1*, 515.

[81] Stillinger, F. H.; Rahman, A. *J. Chem. Phys.* **1974**, *60*, 7943.

[82] Berendsen, H. J. C.; Postma, J. P. M.; Von Gunsteren, W. F.; Hermans, J. **1988**, 331.

[83] Jorgensen, W. L.; Chandrasekhar, J.; Madura, J. D.; Impey, R. W.; Klein, M. L. *J. Chem. Phys.* **1983**, *79*, 926.

[84] Rick, S. W. *J. Chem. Phys.* **2001**, *114*, 2276.

[85] Yu, H. B.; van Gunsteren W. F.and, *J. Chem. Phys.* **2003**, *118*, 221.

[86] Peterson, K. A.; Woon, D. B.; Dunning Jr, T. H. *J. Chem. Phys.* **1994**, *100*, 7410.

[87] edited by D. R. Lide, *CRC Handbook of Chemisry and Physics, 83rd edition* **2002**.

[88] Buckingham, A. D. *Quaterly Reviews of the Chemical Society* **1959**, *13*, 183.

[89] Tang, K. T.; Toennis, J. P. *J. Chem. Phys.* **1977**, *66*, 1496.

[90] Berendsen, H. J. C.; Grigera, J. R.; Straatsma, T. P. *J. Phys. Chem.* **1987**, *91*, 6269.

[91] Nose, S. *J. Chem. Phys.* **1984**, *81*, 511.

[92] Hoover, W. G. *J. Chem. Phys.* **1985**, *81*, 511.

[93] Allen, M. P.; Tildesley, D. J. *Computer Simulation of Liquids*; Clarendon Press: Oxford University Press, Oxford, 1987.

[94] Ewald, P. *Ann. Phys.* **1921**, *64*, 253.

[95] Mak, T. C.; McMullan, R. K. *J. Chem. Phys.* **1964**, *42*, 2732.

[96] van Kleveren, E. P.; Michels, J. P. J.; Schouten, J. A.; Klug, D. D.; Tse, J. S. *J. Chem. Phys.* **2002**, *117*, 6636.

[97] van Kleveren, E. P.; Michels, J. P. J.; Schouten, J. A.; Klug, D. D.; Tse, J. S. *J. Chem. Phys.* **2001**, *114*, 5745.

[98] van Kleveren, E. P.; Michels, J. P. J.; Schouten, J. A.; Klug, D. D.; Tse, J. S. *J. Chem. Phys.* **2001**, *115*, 10500.

[99] McQuarrie, D. A. *Statistical Mechanics*; University Science Books, 2000.

[100] Florusse, L. J.; Peters, C. J.; Schoonman, J.; Hester, K. C.; Koh, C. A.; Dec, S. F.; Marsh, K. N.; Sloan, E. D. *Science* **2004**, 469.

[101] Florusse, L. J.; Peters, C. J.; Schoonman, J. an dHester, K. C.; Koh, C. A.; Dec, S. F.; Marsh, K. N.; Sloan, E. *Science* **2004**, *306*, 469.

[102] Lee, H.; Lee, J.-W.; Kin, D. Y.; Park, J.; Seo, Y.-T.; Zeng, H.; Maoudrakovski, I. L.; Ratcliffe, C.I.and Ripmeester, J. A. *Nature* **2005**, *434*, 743.

[103] Sloan, E. *Soc. Plastic Engineer., Richardson, TX* **2000**, *21*, year.

[104] Becke, A. D. *Phys. Rev. A* **1988**, 3098.

[105] Fanourgakis, G. S.; Apra, E.; Xantheas, S. S. *J. Chem. Phys.* **2004**, *121*, 2655.

[106] Cui, J.; Liu, H.; Jordan, K. D. *J. Phys. Chem. B* **2006**.

[107] Hartke, B. *Phys. Chem. Chem. Phys.* **2003**, *5*, 275.

[108] Burnham, C. J.; Xantheas, S. S. *The Journal of Physical Chemistry* **2002**, *116*, 5115.

[109] Kendall, R. A.; Dunning, T. H.; Harrison, R. J. *J. Chem. Phys.* **1992**, 1481.

[110] Dunning, T. H. *J. Chem. Phys.* **2002**, 6796.

[111] Woon, D. E.; Dunning, T. H.; Harrison, R. J. *J. Chem. Phys.* **1993**, *96*, 1481.

[112] Shin, J.-W.; Hammer, N. I.; Diken, E. G.; Johnson, M. A.; Walters, R. S.; Jaeger, T. D.; Duncan, M. A.; Christie, R. A.; Jordan, K. D. *Science* **2004**, *304*, 1137–1141.

[113] Robertson, E.; Simons, J. *Physical Chemistry Chemical Physics* **2001**, *3*, 1–18.

[114] Zwier, T. *Journal of Physical Chemistry A* **2001**, *105*, 8827–8839.

[115] Carney, J. R.; Zwier, T. S. *Journal of Physical Chemistry A* **2000**, *104*, 8677–8688.

[116] Carney, J. R.; Zwier, T. S. *Chemical Physics Letters* **2001**, *341*, 77.

[117] Dian, B. C.; Longarte, A.; Mercier, S.; Evans, D. A.; Wales, D. J.; Zwier, T. S. *J. Chem. Phys.* **2002**, *117*, 10688.

[118] Florio, G. M.; Christie, R. A.; Jordan, K. D.; Zwier, T. S. *J. Am. Chem. Soc.* **2002**, *124*, 10236.

[119] Chin, W.; Mons, M.; Dognon, J.; Piuzzi, F.; Tardivel, B.; Dimicoli, I. *Physical Chemistry Chemical Physics* **2004**, *6*, 2700–2709.

[120] Fricke, H.; Gerlach, A.; Unterberg, C.; Rzepecki, P.; Schrader, T.; Gerhards, M. *Physical Chemistry Chemical Physics* **2004**, *6*, 4636–4641.

[121] Gerhards, M.; Unterberg, C.; Gerlach, A.; Jansen, A. *Physical Chemistry Chemical Physics* **2004**, *6*, 2682–2690.

[122] Nir, E.; Hunig, I.; Kleinermanns, K.; Vries, M. d. *ChemPhysChem* **2004**, *5*, 131–137.

[123] Dian, B. C.; Longarte, A.; Winter, P. R.; Zwier, T. S. *J. Chem. Phys.* **2004**, *120*, 133–147.

[124] Evans, D. A.; Wales, D. J.; Dian, B. C.; Zwier, T. S. *J. Chem. Phys.* **2004**, *120*, 148.

[125] Dian, B. C.; Florio, G. M.; Clarkson, J.; Longarte, A.; Zwier, T. S. *Journal of Chemical Physics* **2004**, *120*, 9033–9046.

[126] Nesbitt, D. J.; Field, R. W. *Journal of Physical Chemistry* **1996**, *100*, 12735–12756.

[127] Flynn, G. W.; Parmenter, C. S.; Wodtke, A. M. *Journal of Physical Chemistry* **1996**, *100*, 12817–12838.

[128] Silva, M.; Jongsma, R.; Field, R.; Wodtke, A. *Ann. Rev. Phys. Chem.* **2001**, *52*, 811–852.

[129] Connell, L.; Corcoran, T.; Joireman, P.; Felker, P. *Journal of Physical Chemistry* **1990**, *94*, 1229–1232.

[130] Philips, L. A.; P., W. S.; Martinez III, S. J.; R., F. G.; Levy, D. H. *J. Am. Chem. Soc.* **1988**, *110*, 1352.

[131] Nguyen, T. V.; Korter, T. M.; Pratt, D. W. *Journal of Molecular Spectroscopy* **2005**, *(in press)*, year.

[132] Clarkson, J. R.; Baquero, E.; Zwier, T. S. *J. Chem. Phys.* **2005**, *122*, 214312.

[133] Kable, S.; Knight, A. *Journal of Chemical Physics* **1990**, *93*, 3151–3150.

[134] Burgi, T.; Droz, T.; Leutwyler, S. *Chemical Physics Letters* **1995**, *246*, 291–99.

[135] Burgi, T.; Droz, T.; Leutwyler, S. *Journal of Chemical Physics* **1995**, *103*, 7228.

[136] Frisch, M. J.; Pople, J. A.; Binkley, J. S. *J. Chem. Phys.* **1984**, 3265.

[137] EPAPS, *See EPAPS Document No. E-JCPSA6-122-016523 for the complete results from the calculations including optimized geometric parameters and selected associated harmonic frequencies. This document can be reached via a direct link in the online article's HTML reference section or via the EPAPS homepage (http://www.aip.org/pubservs/epaps.html).*

[138] Frisch, M. J. et al. **1995-2004**.

[139] Ahlrichs, R.; an d M. Hser, M. B.; Horn, H.; Klmel, C. *Chem. Phys. Lett* **1989**, *162*, 165–169.

[140] Noga, J.; Bartlett, R. J. *J. Chem. Phys.* **1987**, *86*, 7041.

[141] Raghavachari, K.; Trucks, G. W.; Pople, J. A.; Head-Gordon, M. *Chem. Phys. Lett.* **1989**, 479.